

NAVAL POSTGRADUATE SCHOOL

Monterey, California



THESIS

INCREASING PROMPT RESPONSE FROM IMPULSE RADIATING ANTENNA BY APERTURE SHAPING

by

Michael J. Baretela

March 2002

Thesis Advisor:
Second Reader:

J. Scott Tyo
Michael Morgan

Approved for public release; distribution is unlimited

Report Documentation Page

Report Date 29 Mar 2002	Report Type N/A	Dates Covered (from... to) -
Title and Subtitle Increasing Prompt Response from Impulse Radiating Antenna by Aperture Shaping		Contract Number
		Grant Number
		Program Element Number
Author(s) Baretela, Michael		Project Number
		Task Number
		Work Unit Number
Performing Organization Name(s) and Address(es) Naval Postgraduate School Monterey, California		Performing Organization Report Number
Sponsoring/Monitoring Agency Name(s) and Address(es)		Sponsor/Monitor's Acronym(s)
		Sponsor/Monitor's Report Number(s)
Distribution/Availability Statement Approved for public release, distribution unlimited		
Supplementary Notes		
Abstract		
Subject Terms		
Report Classification unclassified		Classification of this page unclassified
Classification of Abstract unclassified		Limitation of Abstract UU
Number of Pages 120		

REPORT DOCUMENTATION PAGE			<i>Form Approved OMB No. 0704-0188</i>	
Public reporting burden for this collection of information is estimated to average 1 hour per response, including the time for reviewing instruction, searching existing data sources, gathering and maintaining the data needed, and completing and reviewing the collection of information. Send comments regarding this burden estimate or any other aspect of this collection of information, including suggestions for reducing this burden, to Washington headquarters Services, Directorate for Information Operations and Reports, 1215 Jefferson Davis Highway, Suite 1204, Arlington, VA 22202-4302, and to the Office of Management and Budget, Paperwork Reduction Project (0704-0188) Washington DC 20503.				
1. AGENCY USE ONLY (Leave blank)		2. REPORT DATE March 2002	3. REPORT TYPE AND DATES COVERED Master's Thesis	
4. TITLE AND SUBTITLE: Increasing Prompt Response From Impulse Radiating Antenna by Aperture Shaping			5. FUNDING NUMBERS	
6. AUTHOR(S) Michael J. Baretela				
7. PERFORMING ORGANIZATION NAME(S) AND ADDRESS(ES) Naval Postgraduate School Monterey, CA 93943-5000			8. PERFORMING ORGANIZATION REPORT NUMBER	
9. SPONSORING / MONITORING AGENCY NAME(S) AND ADDRESS(ES) N/A			10. SPONSORING / MONITORING AGENCY REPORT NUMBER	
11. SUPPLEMENTARY NOTES The views expressed in this thesis are those of the author and do not reflect the official policy or position of the Department of Defense or the U.S. Government.				
12a. DISTRIBUTION / AVAILABILITY STATEMENT Approved for public release; distribution unlimited			12b. DISTRIBUTION CODE	
13. ABSTRACT (maximum 200 words) <p>In order to improve the prompt response from an impulse radiating antenna (IRA) a number of studies have suggested controlling the spatial distribution of the aperture fields by changing the feed arm angle. Other work has suggested that proper shaping of the aperture can further enhance the radiated signal for a given feed structure. This paper shows how the radiated prompt response can be maximized for a given feed arm configuration by shaping the aperture to eliminate fields orientated in the wrong direction.</p> <p>The percent increase in the prompt radiated electric field for a 200 Ω IRA with a ideally shaped aperture compared to a standard circular aperture ranged from 0.42% to 39.94% depending on the input electrode angle. For the most common electrode angles of 45° and 60° the increases are 6.00% and 16.63% respectively.</p>				
14. SUBJECT TERMS Ultra Wideband Electromagnetics, Time Domain Electromagnetics, Impulse Radiating Antennas, Wideband Antennas.			15. NUMBER OF PAGES 120	
			16. PRICE CODE	
17. SECURITY CLASSIFICATION OF REPORT Unclassified	18. SECURITY CLASSIFICATION OF THIS PAGE Unclassified	19. SECURITY CLASSIFICATION OF ABSTRACT Unclassified	20. LIMITATION OF ABSTRACT UL	

THIS PAGE INTENTIONALLY LEFT BLANK

Approved for public release; distribution unlimited

**INCREASING PROMPT RESPONSE FROM IMPULSE RADIATING ANTENNA
BY APERTURE SHAPING**

Michael J. Baretela
Lieutenant Commander, United States Navy
B.S., State University of New York at Buffalo, 1991

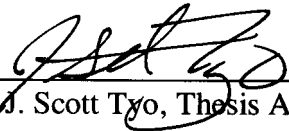
Submitted in partial fulfillment of the
requirements for the degree of

MASTER OF SCIENCE IN ELECTRICAL ENGINEERING

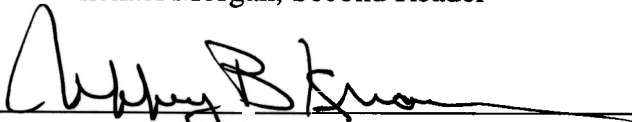
from the

**NAVAL POSTGRADUATE SCHOOL
MARCH 2002**

Author: 
Michael J. Baretela

Approved by: 
J. Scott Tyo, Thesis Advisor


Michael Morgan, Second Reader


Jeffrey B. Knorr, Chairman
Department of Electrical and
Computer Engineering

THIS PAGE INTENTIONALLY LEFT BLANK

ABSTRACT

In order to improve the prompt response from an impulse radiating antenna (IRA) a number of studies have suggested controlling the spatial distribution of the aperture fields by changing the feed arm angle. Other work has suggested that proper shaping of the aperture can further enhance the radiated signal for a given feed structure. This paper shows how the radiated prompt response can be maximized for a given feed arm configuration by shaping the aperture to eliminate fields orientated in the wrong direction.

The percent increase in the prompt radiated electric field for a $200\ \Omega$ IRA with a ideally shaped aperture compared to a standard circular aperture ranged from 0.42% to 39.94% depending on the input electrode angle. For the most common electrode angles of 45° and 60° the increases are 6.00% and 16.63% respectively.

THIS PAGE INTENTIONALLY LEFT BLANK

TABLE OF CONTENTS

I.	INTRODUCTION.....	1
A.	BACKGROUND	1
B.	OBJECTIVE	3
C.	RELATED WORK	3
1.	Effect of Different Focused Aperture Geometries	3
2.	Optimizing Feed Arm Geometry	6
D.	OUTLINE	7
II.	THEORY	9
A.	OPERATION OF A REFLECTOR IRA.....	9
B.	RADIATED FIELD OF AN IRA	9
1.	Field Equivalence Principle	10
2.	Radiated Field From a Focused Aperture	12
3.	Radiated Field in Terms of Aperture Height	15
C.	FINDING THE ELECTRIC FIELD ON THE APERTURE SURFACE.....	15
D.	FINDING THE APERTURE HEIGHT	17
1.	Stereographic Projection.....	18
2.	Electric Field as the Gradient of a Complex Potential	20
3.	Writing the Surface Integral as a Contour Integral.....	21
III.	FINDING THE IDEAL APERTURE SHAPE.....	25
A.	OVERVIEW	25
B.	PROBLEM GEOMETRY.....	25
1.	Self-reciprocal Symmetry.....	27
2.	Symmetry and Boundary Conditions	30
C.	COMPUTING ELECTRIC POTENTIAL DISTRIBUTION	32
1.	Aperture Voltage Distribution Using FEM	32
2.	Contents of Data Files.....	35
3.	Two-dimensional Aperture Voltage Distribution Using Gauss's law.....	37
3.	Comparing FEM Distribution to Gauss's Law	41
D.	FINDING THE IDEAL CONTOUR.....	42
IV.	DETERMINEING THE OPTIMUM CIRCULAR APERTURE	45
A.	OVERVIEW	45
B.	CALCULATE THE APERTURE HEIGHT.....	45
1.	Numerically Computing the Aperture Height h_a	46
2.	Comparing Numerical Value of h_a to an Analytic Form Solution	50
C.	CALCULATED RESULTS	51
1.	Aperture Height h_a	52
2.	Normalized Values for Aperture Height.....	53

3.	Trends	55
a.	<i>Electrode Size</i>	56
b.	<i>Maximum Normalized h_a</i>	56
c.	<i>Optimum Electrode Angle</i>	57
d.	<i>Increase in h_a Due to Following Ideal Contour</i>	57
D.	APERTURE TRIMMING IN ANTENNA DESIGN EXAMPLE	59
V.	EXPERIMENT	63
A.	OVERVIEW	63
B.	EXPERIMENT SETUP	63
1.	The IRA	64
2.	The range	65
3.	Data collection	67
C.	MEASUREMENTS	68
1.	Measuring Input Impedance	68
2.	Measuring the Aperture Height	70
D.	RESULTS	72
1.	Plotting the Results.	72
2.	Comparing Calculated and Measured Results	72
a.	<i>Comparing Aperture Height h_a to Measured Δv</i>	74
b.	<i>Match Between Experiment and Numerical Results</i>	74
3.	Possible Sources for Experimental Error	75
VI.	CONCLUSION AND RECOMMENDATIONS	79
A.	CONCLUSION	79
B.	RECOMMENDATIONS	80
APPENDIX A	81
A.	FIRST TEM FEED ELECTRODE CONFIGURATION	81
B.	SECOND TEM FEED ELECTRODE CONFIGURATION	83
C.	THIRD TEM FEED ELECTRODE CONFIGURATION	85
D.	FOURTH TEM FEED ELECTRODE CONFIGURATION	87
E.	FIFTH TEM FEED ELECTRODE CONFIGURATION	89
F.	SIXTH TEM FEED ELECTRODE CONFIGURATION	91
G.	SEVENTH TEM FEED ELECTRODE CONFIGURATION	93
H.	EIGHTH TEM FEED ELECTRODE CONFIGURATION	95
LIST OF REFERENCES	97
INITIAL DISTRIBUTION LIST	99

LIST OF FIGURES

Figure 1.1. Example of an impulse radiating antenna. [From: Farr 2001]	1
Figure 1.2. Six different apertures tested. A. Horizontal block B. Aperture blocked C. Blocking strip D. Natural aperture E. “Infinite aperture F. Strip aperture. [After: Tyo and Buchenauer, 2001]	4
Figure 1.3. Prompt receive step and impulse responses of the lens IRA with the six aperture configurations depicted in Figure 1.2. The aperture height h_a is proportional to the magnitude of the initial rise of the step responses or the magnitude of the impulse responses. The step radiated response is equivalent to the impulse receive response. The risetime of all six measured signals was between 50 and 55 ps. The impulse responses were obtained by numerical differentiation of the step responses. A Gaussian low-pass filter ($\sigma = 8$ ps) was used to eliminate numerical nose. The impulse responses are offset on the time axis for clarity. [From: Tyo and Buchenauer, 2001]	5
Figure 1.4. Optimum feed impedance as a function of [electrode angle]. Note that the optimum angle for impedances of 100Ω , 150Ω , 200Ω , and 250Ω are approximately 30° , 45° , 60° , and 75° respectively. [After: Tyo, 1999]	7
Figure 2.1. Far-field waveform from an impulse radiating antenna.	9
Figure 2.2. (a) Actual sources. (b) Equivalent source. (c) Love’s equivalent. (d) Electric conductor equivalent.	12
Figure 2.3. Arbitrary source plane used to find radiated electromagnetic fields.	13
Figure 2.4. Two-dimensional view of an IRA.	18
Figure 2.5. A 3-dimensionsl view of the stereographic projection. [From: Yang, 1977]	19
Figure 2.6. Stereographic projection of conical TEM feed electrodes. [After: Farr and Baum, 1992a]	20
Figure 3.1. (a) Side view of the IRA being studied. (b) Front view of the IRA after stereographic projection.	26
Figure 3.2. Some examples of two-dimensional structures and their reciprocals.	28
Figure 3.3. Some examples of self-reciprocal apertures. The structure on the right is the same as the IRA being studied in this paper.	29
Figure 3.4. Taking symmetry into consideration reduces the amount of finite element triangles needed for reasonably accurate results from 68,240 to 8,530.	30
Figure 3.5. Illustration of why the electric field normal to the circle of symmetry is zero. .	31
Figure 3.6. Finite Element mesh used to find the voltage distribution.	32
Figure 3.7. Finite element mesh after rotation.	33
Figure 3.8. Finite element mesh outside the circle of symmetry created using self-reciprocation relationships	34
Figure 3.9. Contours of constant electric potential due to TEM feed electrode. The contours inside the circle of symmetry were calculated using finite element methods. The contours outside the circle of symmetry were found by self-reciprocation.	35

Figure 3.10.	Infinite length line charge surrounded by surface S .	38
Figure 3.11.	Gauss' Law is being used to find the electric potential at point R due to the four electrodes. Each electrode is treated as an infinite plate coming out and going into the page that is broken up into an infinite amount of line charges. The vector \mathbf{r}' points to one of the infinite length line charges.	39
Figure 3.12.	Close up view of the finite element mesh along on of the electrodes. Each segment of the electrode is being approximated by an infinite line charge coming out of the page, located at the center of the electrode.	41
Figure 3.13.	Plot of the percent difference between the electric potential distribution calculated by the finite element method and the by Gauss' Law. The white areas at the bottom are caused by divide by zero errors. The electric potential along the x-axis is zero, so the electric potential in the triangles bordering the x-axis is also zero.	42
Figure 3.14.	IRA showing electric field lines in blue and the ideal contour in black and the circle of symmetry in red.	43
Figure 3.15.	Some examples of Ideal Contours for different electrode size and angle combinations. The entire area below the ideal contour contains aperture electric field that will contribute constructively to the radiated electric field.	44
Figure 4.1.	There are four possible relationships between the circle of symmetry C and the maximum radius R : a) R inside C and inside the inner edge of the electrode, b) R inside C and intersecting the electrode, c) R outside C and intersecting the electrode, d) R outside the electrode. [From: Baretela and Tyo, 2001]	46
Figure 4.2.	Circular shaped aperture that follows the ideal contour with and outer radius larger than the circle of symmetry.	47
Figure 4.3.	This is an enlarged view of the portions of the ideal contour calculated by the MATLAB <i>pdecont</i> command. The ideal contour is divided into m segments identified by starting and ending x-y coordinates. The contribution to h_a is found by summing the average electric potential of each piece multiplied by the length of each piece in the x-direction.	49
Figure 4.4.	This is an enlarged view of the portions of the ideal contour where the geometry is easily identified. The ideal contour is divided into 100 equally sized pieces. The contribution to h_a is found by summing the average electric potential of each piece multiplied by the length of each piece in the x-direction.	50
Figure 4.5.	Comparison of analytic solution for h_a to the numerically computed one. The Analytic solution is for the $\theta_0 = 45^\circ$ case. The aperture height is normalized by the radius of the circle of symmetry.	51
Figure 4.6.	Plot of aperture height vs. the radius of the reflector boundary. Five different electrode angles with electrode sizes corresponding to a TEM input impedance of $200\ \Omega$. The dashed lines represent a circular aperture that does not follow the ideal contour.	52
Figure 4.7.	Aperture height normalized by the size of the focusing aperture. The dashed lines represent a standard circular aperture. This figure can be used in	

IRA design. Suppose a 200Ω antenna with 60° electrodes is being made, looking at the graph, the peak value for h_a occurs at a radius of 1.14 times the circle of symmetry boundary. So if the aperture radius is 1 meter then the circle of symmetry radius will be 1/1.14 or 0.877 meters.....	54
Figure 4.8. Normalized aperture height curves for different input impedances.	57
Figure 4.9. Maximum normalized h_a increases as the electrode angle increases and reaches a maximum at 23°. As the electrode angle continues to increase, the value for h_a begins to decrease.....	58
Figure 4.10. For large electrode angles, a larger portion of the aperture has the electric field orientated in the wrong direction. When this area is removed, there is a greater effect on the radiated electrode field than at small electrode angles.	59
Figure 4.11. Side view of the parachute IRA after being deployed. The canopy of the parachute will be metalized to serve as the reflector of the IRA.	60
Figure 4.12. Two-dimensional view of the parachute IRA along its bore sight. The conical feed electrodes are shown at an angle of 30° after stereographic projection. The shaded portions identify the portions of the aperture that has the input electric field orientated in the wrong direction, thus these areas would not be metalized in order to maximize the radiated prompt electric field.	60
Figure 5.1. AFRL ultra-wideband antenna range.	63
Figure 5.2. Schematic diagram of the experimental setup.....	64
Figure 5.3. Aperture integrated over is the same for both a lens and reflector.....	65
Figure 5.4. (a) IRA used for measurements (b) Lens (c) Various sized electrodes.....	66
Figure 5.5. A 4ns clear time means that a wave traveling along A will reach the end of the range 4ns before the shortest reflected wave B	66
Figure 5.6. Picosecond Pulse Labs 4050B step generator and the 4 ns monocone antenna ..	67
Figure 5.7. (a) Tektronix Digital Sampling Oscilloscope (b) Top view of the focal point of IRA showing the TEM electrodes connected to the co-axial cable protruding through the ground plane.	67
Figure 5.8. (a) Template that was used to cut the metal foil used to block the areas of the aperture above the ideal contour. (b) Metal foil template attached to the flat surface of the lens.	68
Figure 5.9. One-inch metal foil strips were used to simulate different sized apertures by blocking the prompt response of the IRA.	69
Figure 5.10. Plot of TDR response used to find impedance	70
Figure 5.11. Received step response for a 200Ω, 40° electrode IRA.....	71
Figure 5.12. An 8ps Gaussian filter was used to remove high frequency noise from the step response	73
Figure 5.13. Received step response and corresponding transmit impulse response for a 200Ω, 30° electrode. Notice that the late time response becomes apparent around 320 picoseconds.....	74
Figure 5.14. Experimental values for h_a denoted by the x's compared to calculated data for 200Ω IRAs	76

Figure 5.15. Experimental values for Normalized h_a denoted by the x's compared to calculated data for 200 Ω IRAs.....	77
Figure 5.16. Experimental values for h_a and Normalized h_a denoted by the x's compared to calculated data for 200 Ω IRAs	78
Figure A.1. Step and impulse response.....	82
Figure A.2. Step and impulse response.....	84
Figure A.3. Step and impulse response.....	86
Figure A.4. Step and impulse response.....	88
Figure A.5. Step and impulse response.....	90
Figure A.6. Step and impulse response.....	92
Figure A.7. Step and impulse response.....	94
Figure A.8. Step and impulse response.....	96

LIST OF TABLES

Table 3.1. Parameter values for different IRA configurations.....	37
Table 4.1. Increase in aperture height due to an ideal contour shaped aperture.	56
Table 4.2. Increase in radiated field for the parachute IRA due to an ideal shaped aperture boundary.	61

THIS PAGE INTENTIONALLY LEFT BLANK

EXECUTIVE SUMMARY

The IRA is a class of antenna that has been developed in order to radiate ultra-wideband pulses of electromagnetic radiation [Baum et al, 1999]. These antennas use a non-dispersive transverse electromagnetic (TEM) transmission line to feed a focusing optic, usually a lens or a reflector. The focused aperture radiates (in the far-field) the approximate derivative of the signal applied to the feed, so when the IRA is fed by a fast-rising step, a short-duration, high-amplitude, impulse-like waveform is produced.

It is well known that the radiated electric field (E_{rad}) of an IRA is proportional to the surface integral of the transverse electric field (E_y) over the focused aperture [Baum et al, 1999]

$$E_{rad} \propto h_a \propto \iint_{S_a} E_y(x, y) ds, \quad (1)$$

where h_a is termed the aperture height and S_a is the area of the focused aperture. This integral is often computed by writing E_y as the gradient of a potential function in the complex plane and applying Green's theorem

$$E_{rad} \propto h_a = \frac{1}{v} \oint_{C_a} u dx, \quad (2)$$

where u is the electric potential, v is the magnetic potential and C_a is the closed contour enclosing S_a [Baum et al, 1999].

CHOOSING THE IDEAL SHAPE OF THE APERTURE

Equation 1 shows that the far field is determined by the y-component of the electric field everywhere in the aperture. If one could eliminate the areas of the aperture where E_y is oriented in the wrong direction, the prompt radiated response from the IRA would be improved. In order to find these areas of negative contribution we must first calculate the electric field in the aperture. Solving the Laplace equation for the TEM feed structure and taking the gradient of the resulting electric potential accomplish this.

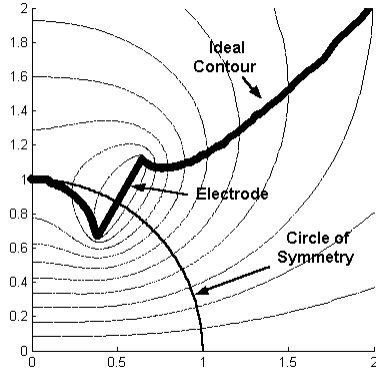


Figure 1. Ideal contour.

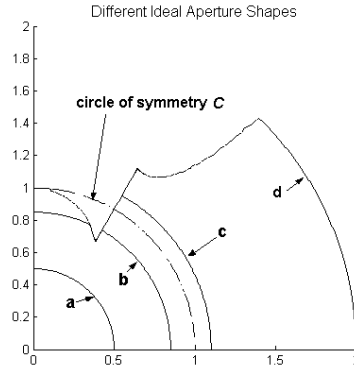


Figure 2. The dashed line denotes the circle of symmetry. There are four possible relationships between the circle of symmetry C and the maximum radius R : a) R inside C and inside the inner edge of the electrode, b) R inside C and intersecting the electrode, c) R outside C and intersecting the electrode, d) R outside the electrode.

Figure 1 shows the equipotential lines for one electrode configuration $\Phi_0 = 30^\circ$, $Z_0 = 200\Omega$. The electric potential is calculated inside the self-reciprocity circle of symmetry using MATLAB's PDE Toolbox to solve the Laplace equation by the finite element method [Baum, 1998]. The electric potential outside the circle of symmetry can be found using the self-reciprocal symmetry considerations presented in [Farr and Baum, 1995], and the electric field can be found by taking the gradient of the electric potential distribution.

Once the electric field is known, it is a trivial matter to find out the areas where E_y is less than zero. The bold line in Figure 1 is where $E_y = 0$ and is referred to as the ideal contour, as E_y is orientated in the correct direction below the ideal contour. Each electrode size and angle combination will produce a slightly different ideal contour similar in shape to the one in Figure 1.

For most IRA applications the aperture size is fixed, and the optic is normally a paraboloidal reflector or a lens that has the same outer dimensions as the circle of symmetry. The maximum possible radiated field from a given aperture and electrode configuration will result by projecting the ideal contour onto the aperture and eliminating the parts of the aperture outside. For a reflector aperture, the paraboloidal surface should

be made of some non-reflecting material, and metalization applied only to the region inside the ideal contour. A second question is whether, for a given aperture size, the response can be improved by optimizing the position of the circle of symmetry relative to the maximum aperture size while forcing the aperture boundary to follow the ideal contour. Figure 2 shows a number of different ideal aperture shapes relative to the circle of symmetry.

The aperture height h_a in Equation 2 is a useful tool to find the optimum position of the circle of symmetry relative to the aperture boundary. A high value for h_a is desired since h_a is proportional to the prompt radiated electric field. Figure 3 is a plot of the normalized aperture height vs. the relative radius of the ideal shaped aperture for a number of feed arm size and angle combinations corresponding to a 200Ω input impedance. The circle of symmetry is at $R=1$. The angles are measured clockwise from the y-axis.

The maximum h_a in Figure 3 is near an electrode angle of 30° at a radius of $R=1.125$ relative to the circle of symmetry. It is important to note that the h_a increase in Figure 3 is not caused by increasing the actual size of the aperture. Two factors cause this increase. First, the edge of the aperture is following the ideal contour instead of the circle of symmetry. Second, by changing the size of the electrodes, the circle of symmetry is being made larger or smaller relative to the edge of the aperture. Thus for a given size, the aperture encompasses the portions of the input electric field that have the greatest positive effect on the prompt radiated electric far field. Table 1 shows the improvement in h_a due to using the ideal contour/optimum circle of symmetry position over a circular shaped aperture with its boundary on the circle of symmetry.

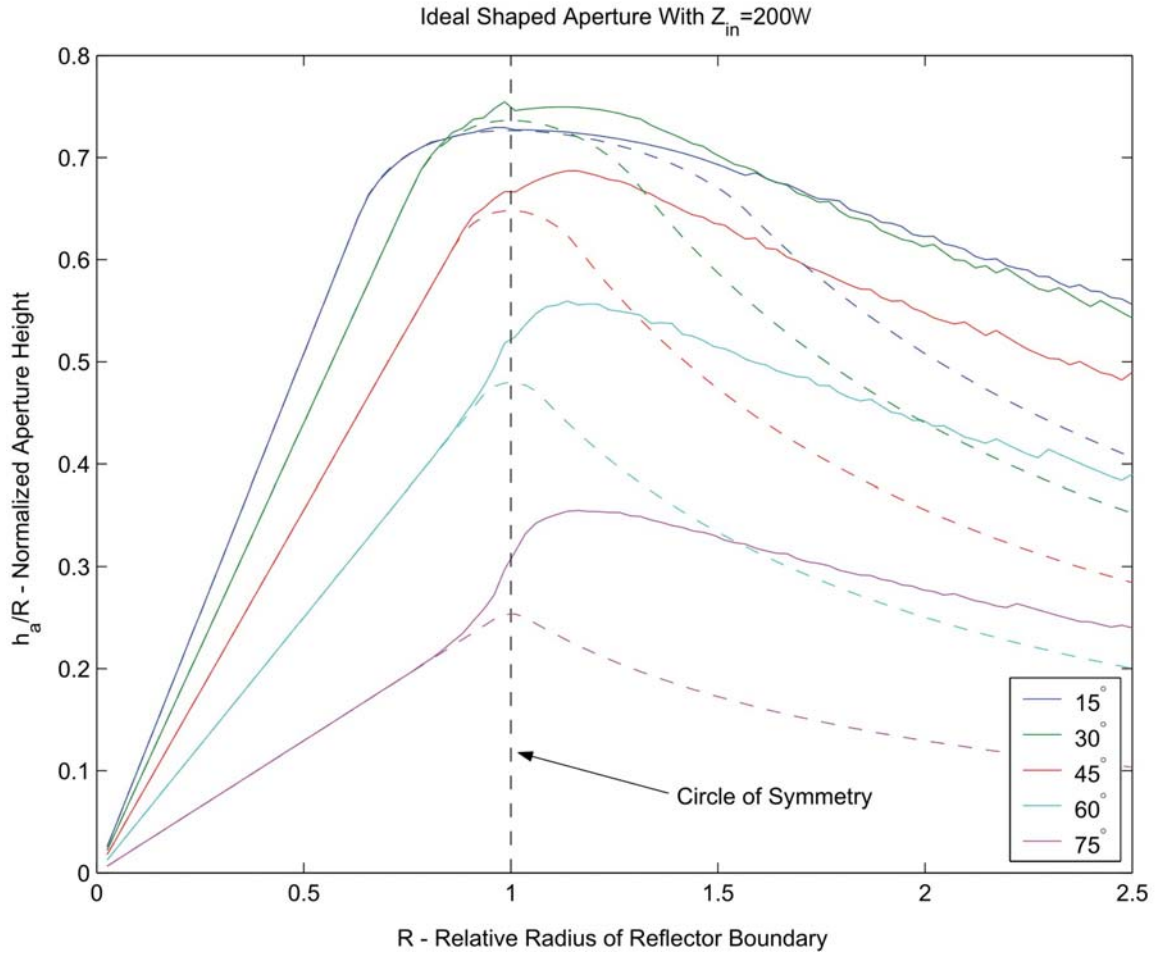


Figure 3. Aperture height normalized by the size of the focusing aperture. The dashed lines represent a standard circular aperture.

Feed Angle	h_a R=1	h_a Ideal	h_a Increase	Relative Aperture Size
75°	0.2537	0.3562	40%	1.15
60°	0.4797	0.5563	16%	1.15
45°	0.6482	0.6870	5.9%	1.15
30°	0.7363	0.7494	1.8%	1.125
15°	0.7265	0.7304	0.5%	0.95

Table 1. Increase in h_a Due to Aperture Boundary Following Ideal Contour and Optimum Circle of Sym. Position

EXPERIMENTAL RESULTS

An experiment was conducted to validate the computational methods used in determining the ideal contours and the values of h_a . An antenna was configured as a half-lens IRA over a ground plane and measured on receive. The transmitted electric field from an antenna is the derivative of the received field under the same excitation due to reciprocity [Baum et al, 1999]. The transmitting antenna was a 4-ns monocone over the same ground plane, radiating a 50-ps risetime, 10V step. Covering portions of the lens with metal foil simulated the different aperture contours.

Figure 4 compares calculated values for 200Ω TEM electrode configurations with the experimental results denoted by the blue x's. The results follow the same trend as the calculations. Notice for the 30° case that the radius of symmetry is at 8 inches and the maximum value for h_a is at a radius of 9. This corresponds to a normalized aperture radius of 1.125, which is the same as the value in Table 1. Also, for the most part, the increase in h_a appears to be on the same order of magnitude as reported in Table 1.

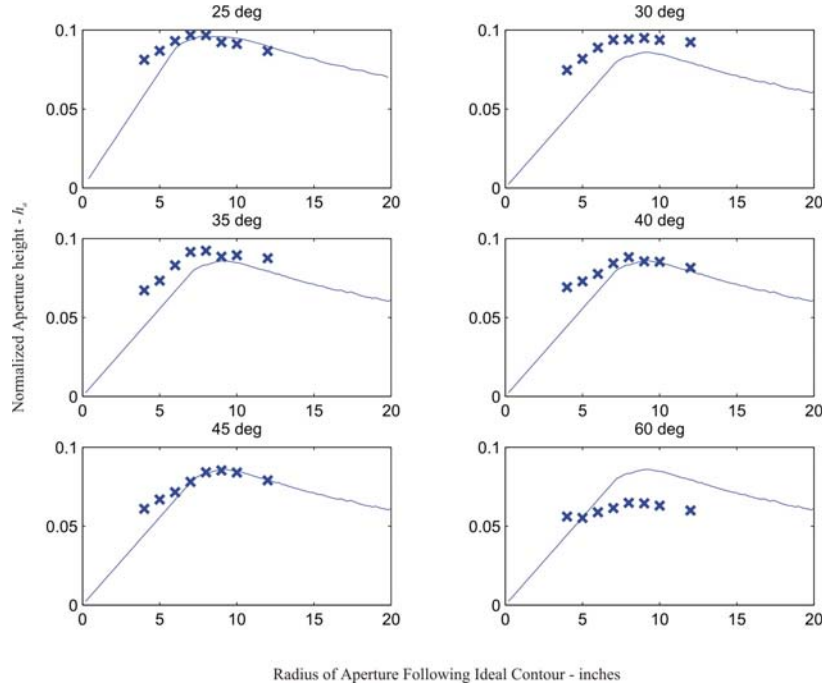


Figure 4. Comparison between experimental and calculated results.

CONCLUSION

The radiated far field of an IRA can be improved by changing the shape of the aperture to eliminate the portions of the aperture that contribute negatively to the far field. There is a more dramatic increase at larger TEM feed electrode angles. Experiment closely follows the calculated results. These results can be used to optimize the prompt radiated field from a fixed aperture shape and size by scaling the circle of symmetry relative to the maximum aperture size and by eliminating the portions of the aperture outside the ideal contour.

I. INTRODUCTION

A. BACKGROUND

Impulse-radiating antennas (IRA) are a class of antenna designed to radiate ultra-wideband pulses of electromagnetic radiation. IRAs are well suited for high power impulse electronic warfare applications whose objective is generate large amounts of electromagnetic energy. These antennas use a non-dispersive transverse electromagnetic (TEM) transmission line to feed a lens or reflector focusing optic. The early time field radiated by the focusing optic is approximately the derivative of the signal applied to the feed. Thus when the IRA is fed by a fast rising step, a short duration, high amplitude impulse like waveform is produced.

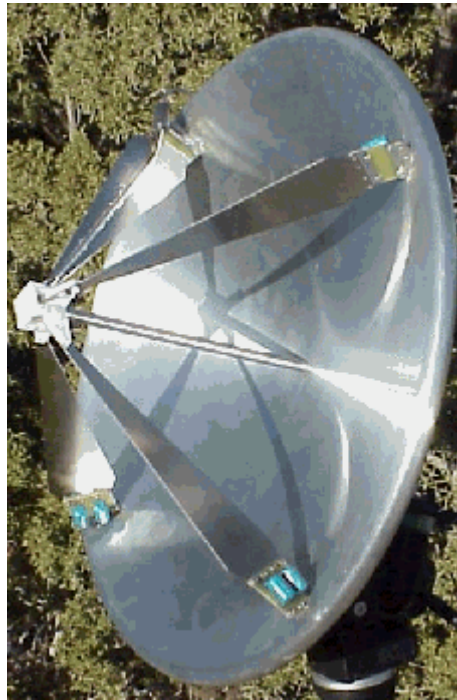


Figure 1.1. Example of an impulse radiating antenna. [From: Farr 2001]

Other applications for IRAs include: antennas that operate simultaneously on multiple frequencies [Baum et al, 1999], ground-penetrating radar [Rhebergen, 1998], and radar that is used in highly cluttered environments [Baum and Farr, 1993].

Most reflector IRAs have been built with two pairs of crossed, coplanar feed arms oriented at 90° angles with a feed impedance of 200Ω , similar to the IRA pictured in Figure 1.1. Recently, it has been suggested that different feed arm angles might produce increased radiated fields [Baum, 1998; Tyo, 1999]. New experimental results using 30° (clockwise from vertical) feed arms for an IRA have produced significant improvements in prompt radiated fields; with the additional benefit of reducing cross-polarized response of the antenna [Farr and Bowen, 2000].

In practice there are three ways to increase the radiated field of an IRA with given input impedance. First is to increase the input voltage on the feed arms of the antenna. However, this voltage cannot be increased indefinitely without reaching the dielectric breakdown of air or some other medium. A second approach is to shorten the rise time of the input waveform. Since the transmitted response of an IRA is the derivative of the input excitation, a faster input rise time will increase the magnitude of the response.

A third approach involves designing the antenna aperture to increase the radiated response of the antenna. Three ways in which this can be accomplished are, changing the *angle* of the input TEM feed arms, changing the *shape* of the aperture, and changing the *size* of the aperture relative to the size of the TEM feed arms. As mentioned earlier, impulse radiating antennas are now being built with TEM feed arms orientated 120° apart vice 90° . Optimizing the shape and relative size of an IRA aperture has not yet been undertaken and is the subject of this thesis.

As discussed in Chapter II the radiated field of an IRA is proportional to the integral of the electric field everywhere on the surface of the aperture. Not all of this electric field on the aperture surface is orientated in the correct direction and thus contributes destructively to the radiated field. So, by trimming off portions of the aperture with the electric field orientated in the wrong direction, the radiated electric field should be increased. In conjunction with trimming the aperture, the size of the aperture relative to the size of the input TEM electrodes plays a part in the magnitude of the radiated field. Should the size of the aperture be made larger or smaller relative to the size of the input electrodes?

B. OBJECTIVE

The objective of this work is to show that proper shaping and sizing of the aperture can increase the radiated field in the far field for an IRA. To accomplish this, the ideal aperture shape is calculated for a number of different TEM feed configurations. All of the electric field on an ideal aperture will be orientated in the correct direction to contribute constructively to the radiated field.

This ideal aperture shape is applied to different “aperture windows” in order to maximize the radiated field. Often the size and shape of an antenna aperture is decided by factors other than antenna optimization. For example, the available space for an IRA aperture might be a 1-meter diameter circle.

An experiment is also conducted to verify the methods used to compute the effects on radiated field due to aperture trimming.

C. RELATED WORK

IRAs were originally an outgrowth of Air Force research in nuclear-electromagnetic-pulse (EMP) simulators used to test electronic systems. Many applications today require fast rising, narrow electromagnetic pulses, though at much smaller power levels than that of an EMP [Baum et al, 1999]. The theory and operation of IRAs has been extensively researched and documented mainly by the Air Force Research Lab (AFRL) and its associates. Two recently conducted studies by the AFRL directly lead into this work. One is on the effect of different focused aperture geometries on the radiated electric field [Tyo and Buchenauer, 2001] and another on optimizing the input feed impedance by changing the geometry of the TEM feed electrodes [Tyo, 1999].

1. Effect of Different Focused Aperture Geometries

An experiment was conducted at AFRL to see if the prompt response from an IRA can be accurately predicted when the shape of the focusing aperture is changed. A lens IRA operating in the receive mode was placed on a 40 ft ground plane opposite a 40 nanosecond monocone antenna that was transmitting 10 Volt 10 nanosecond duration voltage steps. The derivative of the received step response of an IRA is equal to the transmitted step response by a property called reciprocity. [Baum et al, 1999] This allows data that is collected on an IRA operating in the receive mode to be applied to the

same antenna operating in the transmit mode. In order to change the shape of the focusing aperture, portions of the lens were blocked with metal foil. This effectively prevents the electric field on the blocked portions of the lens from contributing to the prompt response of the antenna. [Tyo and Buchenauer, 2001]

Figure 1.2 shows the six different apertures that were tested in this experiment. The small triangle represents the TEM horn and the rectangles represent the metal foil used to block the prompt response of the antenna. The received step responses and corresponding transmitted responses are shown in Figure 1.3.

Notice in the unblocked case, case E of Figures 1.2 and 1.3, that the received step response is a fast rising step with a gradual linear decay and its corresponding transmitted step response is a narrow impulse like waveform. Next take a look at case A where the aperture is blocked everywhere below the TEM input electrodes. This received and transmitted step responses both become negative suggesting that the covered areas of the lens block electric field that would have contributed constructively to the step response. Finally in case F, the aperture is blocked everywhere above the TEM feed electrodes. The received and transmitted responses both have a greater magnitude than the unblocked case E. [Tyo and Buchenauer, 2001]

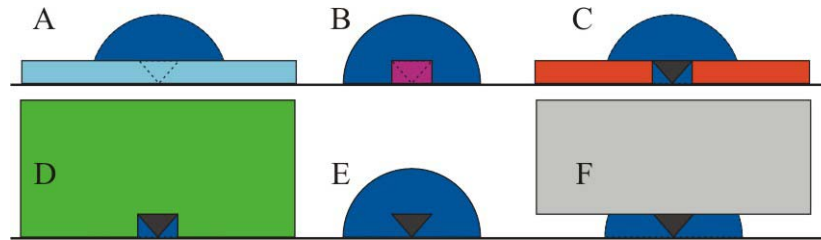


Figure 1.2. Six different apertures tested. A. Horizontal block B. Aperture blocked C. Blocking strip D. Natural aperture E. “Infinite aperture F. Strip aperture. [After: Tyo and Buchenauer, 2001]

This shows that altering the shape of the focusing aperture can increase or decrease the magnitude of the prompt response. Another outcome of this experiment showed that the calculated response was within 10% of the measured response with the

difference mainly contributed to experimental error. The next task is to determine the optimum aperture shape, which is accomplished in this thesis.

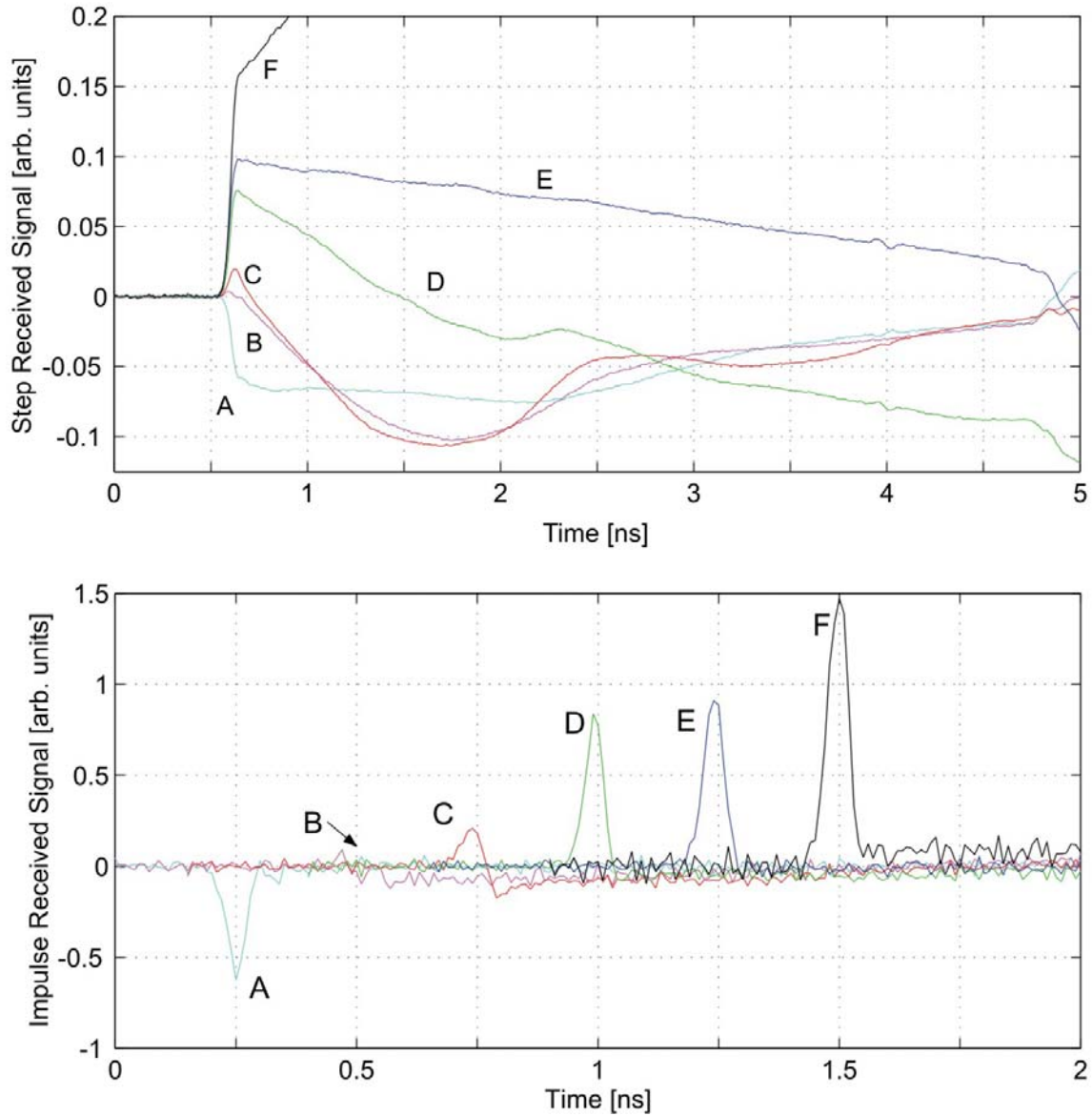


Figure 1.3. Prompt receive step and impulse responses of the lens IRA with the six aperture configurations depicted in Figure 1.2. The aperture height h_a is proportional to the magnitude of the initial rise of the step responses or the magnitude of the impulse responses. The step radiated response is equivalent to the impulse receive response. The risetime of all six measured signals was between 50 and 55 ps. The impulse responses were obtained by numerical differentiation of the step responses. A Gaussian low-pass filter ($\sigma = 8$ ps) was used to eliminate numerical noise. The impulse responses are offset on the time axis for clarity. [From: Tyo and Buchenauer, 2001]

2. Optimizing Feed Arm Geometry

Changing the angle of the input TEM feed electrodes was one of the ways mentioned above to increase the prompt response of an IRA. A study was conducted to compute the effect of TEM feed electrode angle on the radiated field of an IRA. The aperture height (h_a) parameter is common to a number of different performance metrics discussed in this paper and is proportional to the surface integral of the electric field on the focusing aperture. Which in turn is proportional to the radiated electric field. This implies that for a given input impedance, maximizing h_a will also maximize the prompt response of the IRA. Therefore, h_a was the parameter that was maximized to determine the optimum input feed electrode angle. [Tyo, 1999]

The electric potential distribution for numerous circular shaped 4-arm IRAs was computed. The angle of the input feed electrodes ranged from 3° to 87° measured counterclockwise from horizontal*. It was found that for a given input impedance, there was a corresponding optimum feed arm angle, and vice versa. In fact as shown in Figure 1.4 the relationship between the optimum feed angle and impedance is essentially linear. This paper includes much discussion on the effects of changing the angle of the feed arms and it provides a method on designing an antenna that maximizes the prompt response by choosing the optimum feed arm angle.

Two important aspects of this paper are used directly in this thesis. First, the computed electric potential distributions for the different feed arm electrode size and angle combinations were stored in a database. The data contained in this database was used as a starting point in this thesis. Second, the fact that the aperture height parameter h_a is proportional to the magnitude of the prompt response is also used in this thesis to determine the optimum aperture shape.

* Since Tyo wrote this paper, the convention for measuring the angle of the electrodes has been changed. Now the electrode angle is measured clockwise from the vertical axis of the IRA. This new convention is used in this thesis.

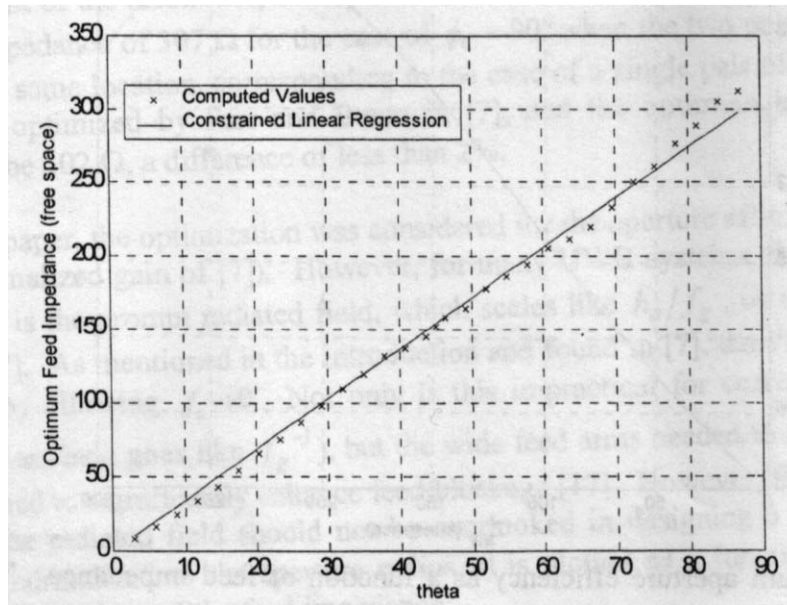


Figure 1.4. Optimum feed impedance as a function of [electrode angle]. Note that the optimum angle for impedances of 100Ω , 150Ω , 200Ω , and 250Ω are approximately 30° , 45° , 60° , and 75° respectively. [After: Tyo, 1999]

D. OUTLINE

The theory of how an IRA works and how the prompt radiated electric field can be computed is contained in Chapter II. Chapter III shows how the ideal aperture shape is found. In Chapter IV, the ideal aperture shape is applied to circular aperture windows and the optimum aperture shape is found. The experiment conducted at the AFRL ultra-wideband antenna range to verify the calculated results is contained in Chapter V. Finally some conclusions and recommendations are made in Chapter VI.

THIS PAGE INTENTIONALLY LEFT BLANK

II. THEORY

A. OPERATION OF A REFLECTOR IRA

The makeup of an IRA usually consists of a conical TEM wave launcher connected to a parabolic reflector. The TEM electrodes are excited with a step voltage source and a spherical TEM wave is sent into the parabolic reflector. The reflector converts the spherical wave into a plane wave in the near field, and in the far field the radiated wave behaves as the derivative of the input field. Figure 2.1 is an example time waveform of the far field magnitude. The pre-pulse is associated with the field given off the voltage source that reaches the far-field before the reflected response does. The impulse response is the focused prompt response from the IRA that is seen along the bore-sight of the antenna. [Baum, 1989] For electronic warfare applications it is desired to maximize the magnitude of this impulse response. The late time response is caused by the decay of the input step excitation, feed blockage, unfocused reflections from the reflector among other factors. [Giri and Baum, 1994] This portion of the wave-form is not as important in this application.

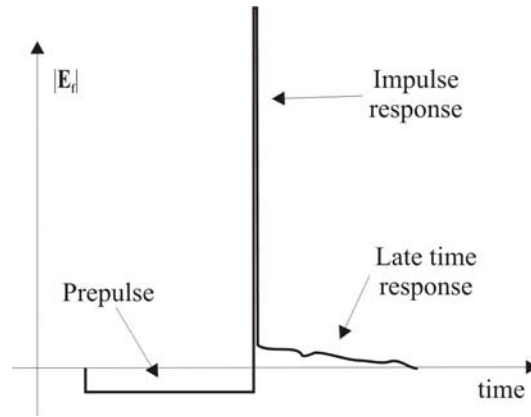


Figure 2.1. Far-field waveform from an impulse radiating antenna.

B. RADIATED FIELD OF AN IRA

The main objective of this work is to maximize the radiated electric field of an IRA by proper shaping of the antenna aperture without increasing the overall size of the aperture. In order to accomplish this a relationship between the radiated electric field and

the antenna aperture needs to be found. Normally, for an antenna the radiation characteristics can be found if the current distribution on the surface of the antenna is known everywhere and at anytime. For simple geometries, such as a wire antenna, the current distribution is relatively easy to find. However, the current distribution on the electrodes and reflector of an IRA is not easy to find so alternate methods are typically used to find the radiation characteristics. The IRA belongs to a class of antenna called aperture antennas and for this class of antennas the radiated fields can be determined using the Field Equivalence Principle.

1. Field Equivalence Principle

By Huygens' Principle and the Uniqueness Theorem, the fields in a source-free region can be determined if the tangential electrical and magnetic fields over a closed surface inside that region are known [Balanis, 1982]. The Field Equivalence Principle takes this one step further, by enclosing an electromagnetic source with an imaginary closed surface:

...the fields outside an imaginary closed surface are obtained by placing over the closed surface suitable electric- and magnetic-current densities which satisfy the boundary conditions. The current densities are selected so that the fields inside the closed surface are zero and outside they are equal to the radiation produced by the actual sources. [Balanis, 1982]

Figure 2.2a shows a source denoted by the electric and magnetic current densities \mathbf{J}_1 and \mathbf{M}_1 that produces electric and magnetic fields \mathbf{E}_1 and \mathbf{H}_1 in the region V_1 . Using the Equivalence Principle, the sources are replaced in Figure 2.2b by surface S and equivalent sources satisfying the following boundary conditions [Balanis, 1982]:

$$\begin{aligned}\mathbf{J}_s &= \hat{\mathbf{n}} \times [\mathbf{H}_1 - \mathbf{H}_2], \\ \mathbf{M}_s &= -\hat{\mathbf{n}} \times [\mathbf{E}_1 - \mathbf{E}_2].\end{aligned}\tag{2.1}$$

The surface densities in Equation 2.1 produce the same fields in region V_1 as those of Figure 2.2a. However, inside the surface there are new fields \mathbf{E}_2 and \mathbf{H}_2 . Since the fields inside surface S can be anything, as long as the boundary conditions are met, they are typically assumed to be zero. This case, shown in Figure 2.2c is known as

Love's Equivalence Principle and has the following simpler boundary conditions [Balanis, 1982]:

$$\begin{aligned}\mathbf{J}_s &= \hat{\mathbf{n}} \times \mathbf{H}_1, \\ \mathbf{M}_s &= -\hat{\mathbf{n}} \times \mathbf{E}_1.\end{aligned}\tag{2.2}$$

A further simplification can be made if the medium inside V_2 is replaced with a perfect electrical conductor (PEC). Unlike Love's Equivalence Principle where the current was free to radiate in an unbounded medium, the current now radiates in the presence of an electrical conductor. Using Image theory on a planar PEC boundary, \mathbf{J}_s cancels out and \mathbf{M}_s doubles therefore the boundary conditions become [Balanis, 1982]:

$$\begin{aligned}\mathbf{J}_s &\cong 0, \\ \mathbf{M}_s &\cong 2(-\hat{\mathbf{n}} \times \mathbf{E}_1).\end{aligned}\tag{2.3}$$

Equation 2.3 is a good approximation in the far field, but if the radiation characteristics are needed in the near field, it is better to use Love's Equivalence Principle from Equation 2.2. Equation 2.3 will be used in this case since the far field radiation characteristics of an IRA are of interest for electronic warfare applications.

Equations that describe the far-field radiation characteristics due to surface electric and magnetic current densities near a PEC have been developed. [Balanis, 1982] These equations contain the following surface integral whose significance will become apparent shortly:

$$\iint_S \mathbf{M}_s \frac{e^{-jkR}}{R} d\mathbf{S}'\tag{2.4}$$

At this point, it seems that the only benefit of using the Field Equivalence Principle is that the original complicated source current densities have been replaced by different current densities on a different surface. Even with all of the simplifications made, the magnetic surface current density is still needed to find the far field radiation characteristics. The key is in Equation 2.3; for the IRA being studied the electric field at the surface, which is also a plane, is a known quantity! The field is produced by the antenna input TEM feed electrodes. Since the electric field at the surface is known, the

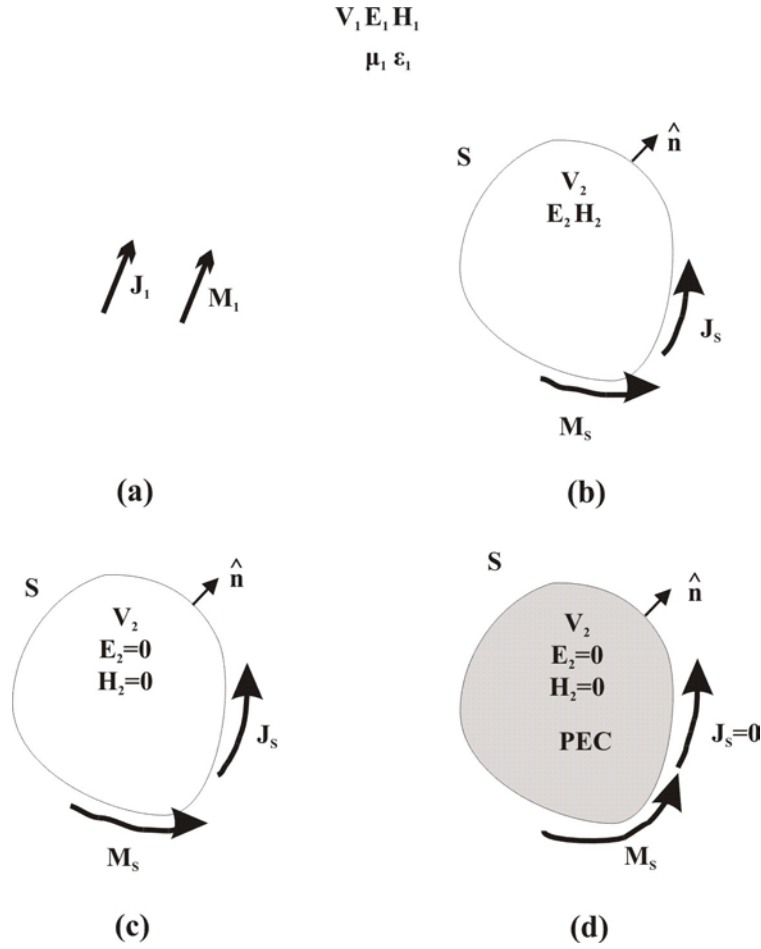


Figure 2.2. (a) Actual sources. (b) Equivalent source. (c) Love's equivalent. (d) Electric conductor equivalent.

magnetic current can be found by Equation 2.3 and consequentially the far-field radiation characteristics are found using the equations derived by Balanis.

2. Radiated Field From a Focused Aperture

Consider the arbitrary planar aperture S' shown in Figure 2.3. The x and y -axis are in the same plane as the aperture and the z -axis is perpendicular to the aperture. The convention of using primed variable for sources will be used. The position vector for a point on the aperture is:

$$\mathbf{r}' = (x', y', z'), \quad (2.5)$$

with $z' = 0$ in this case. For a point not on the aperture the position vector is:

$$\mathbf{r} = (x, y, z). \quad (2.6)$$

The tangential electric field in the time domain on the surface of the aperture is written as:

$$\mathbf{E}_T(x', y'; t), \quad (2.7)$$

with t referring to time and the z' component being left out since it is equal to zero.

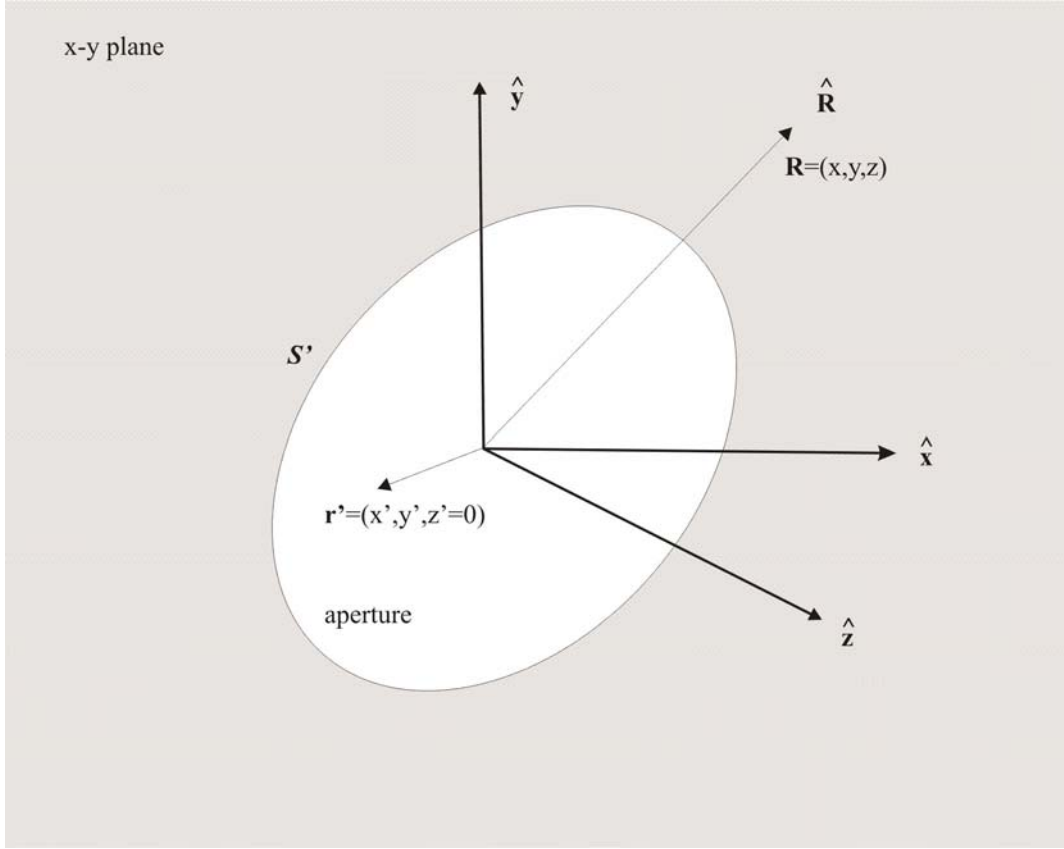


Figure 2.3. Arbitrary source plane used to find radiated electromagnetic fields.

Applying the Field Equivalence Principle, the radiated electric field in the frequency domain at some position r is [Baum, 1987]:

$$\mathbf{E}_{rad}(\mathbf{r}, s) = \frac{1}{2\pi} \iint_{S'} \frac{\gamma R + 1}{R^2} \left[\left(\hat{\mathbf{z}} \times \mathbf{E}_T(x', y'; s) \right) \times \hat{\mathbf{R}} \right] e^{-\gamma R} dS', \quad (2.8)$$

with the following terms defined as:

$$s \equiv \text{complex frequency}, \quad (2.9)$$

$$\gamma \equiv \frac{s}{c} \equiv \text{free-space propagation constant}, \quad (2.10)$$

$$c \equiv \frac{1}{\sqrt{\mu_0 \epsilon_0}} \equiv \text{speed of light}, \quad (2.11)$$

$$R \equiv |\mathbf{r} - \mathbf{r}'| = \sqrt{(x - x')^2 + (y - y')^2 + z^2} \text{ and}, \quad (2.12)$$

$$\hat{\mathbf{R}} \equiv \text{unit vector in the direction of } R. \quad (2.13)$$

Take a close look at the surface integral in Equation 2.8, notice that it is remarkably similar to Equation 2.4 in the frequency domain. The term $(\hat{\mathbf{z}} \times \mathbf{E}_T(x', y'; s))$ is proportional to the surface magnetic current density \mathbf{M}_s .

Equation 2.8 is the general equation for the radiated electric field at a given point in space from an aperture antenna at $z' = 0$. Using an aperture that focuses the radiated electric field along the bore sight of the IRA ($\hat{\mathbf{R}} = \hat{\mathbf{z}}$) at a distance of $R \rightarrow \infty$, Equation 2.8 simplifies to [Baum, 1989]:

$$\mathbf{E}_{rad}(\mathbf{r}, s) = \frac{se^{-\gamma R}}{2\pi c R} \iint_{S'} \mathbf{E}_T(x', y'; s) d\mathbf{S}' \quad (2.14)$$

Taking the inverse Laplace transformation Equation 2.14 becomes:

$$\mathbf{E}_{rad}(\mathbf{r}, t) = \frac{1}{2\pi R} \frac{d}{dt} \iint_{S'} \mathbf{E}_T(x', y'; t - R/c) d\mathbf{S}'. \quad (2.15)$$

Since a focusing aperture is being used, the time characteristics of the transverse field on the aperture \mathbf{E}_T can be written as [Baum, 1989]:

$$\mathbf{E}_T(x', y'; t) = \mathbf{E}_{rad}(x', y') f(t). \quad (2.16)$$

Equation 2.15 becomes:

$$\mathbf{E}_{rad}(\mathbf{r}, t) = \frac{1}{2\pi R} \frac{d}{dt} f(t) \iint_{S'} \mathbf{E}_T(x', y') d\mathbf{S}', \quad (2.17)$$

where $f(t)$ describes the time characteristics of the input electric field on the aperture \mathbf{E}_T .

In order to create the impulse like waveforms associated with IRAs, the antennas are typically excited with a fast rising step voltage source. Thus the electric field on the

aperture \mathbf{E}_T is also a fast rising step function in the time sense. This causes Equation 2.17 to result in a short high magnitude pulse, which is exactly the desired characteristic of an IRA being used in electronic warfare applications.

3. Radiated Field in Terms of Aperture Height

Equation 2.17 relates the radiated field along the bore sight of an IRA to the input electric field on the aperture of the antenna. For an IRA with a given optic and feed geometry and input impedance the radiated field along the bore Equation 2.17 becomes:

$$\mathbf{E}_{rad}(R, t) = -\frac{1}{2\pi R c f_g} \mathbf{h}_a \frac{dV}{dt}, \quad (2.18)$$

where V_0 is the voltage applied to the feed, f_g is a geometric impedance factor defined as:

$$\begin{aligned} f_g &= Z_{line} / Z_{medium}, \\ Z_{medium} &= \sqrt{\mu / \epsilon}, \end{aligned} \quad (2.19)$$

and finally the aperture height [Baum et al, 1999]:

$$\mathbf{h}_a = -\frac{f_g}{V_0} \iint_S \mathbf{E}_T(x, y) ds. \quad (2.20)$$

The aperture height \mathbf{h}_a is a useful parameter to measure the performance of an IRA. Notice in Equation 2.18 that for a given antenna, the radiated electric field is directly proportional to the magnitude of \mathbf{h}_a . Therefore if the magnitude of \mathbf{h}_a is increased, so will the magnitude of the radiated field. From Equation 2.20 \mathbf{h}_a can be increased with out changing the size of the aperture since it is directly proportional to the integral of the transverse electric field on the surface of the focusing aperture.

C. FINDING THE ELECTRIC FIELD ON THE APERTURE SURFACE

The previous section defined the relationship between the radiated electric field and the input electric field on the focusing aperture. This electric field is created by the input TEM feed electrodes. A good starting point to find this electric field are the source free Maxwell's equations for time-harmonic waves in a linear, isotropic and homogeneous medium [Cheng, 1989]:

$$\nabla \times \mathbf{E} = -j\omega\mu\mathbf{H} \quad (2.21)$$

$$\nabla \times \mathbf{H} = j\omega\epsilon\mathbf{E} \quad (2.22)$$

$$\nabla \cdot \mathbf{E} = 0 \quad (2.23)$$

$$\nabla \cdot \mathbf{H} = 0. \quad (2.24)$$

Since the input waves are assumed to be TEM, the electric and magnetic fields can be written as the following in spherical coordinates:

$$\mathbf{E} = \frac{\mathbf{E}_T(\theta, \phi) e^{-jkR}}{R}, \quad (2.25)$$

$$\mathbf{H} = \frac{\mathbf{H}_T(\theta, \phi) e^{jkR}}{R}. \quad (2.26)$$

Note that \mathbf{E}_T and \mathbf{H}_T have units of Volts and Amps. Since \mathbf{E} has units of Volts per meter and \mathbf{H} has units of Amps per meter, we use \mathbf{E}_T and \mathbf{H}_T to capture the vector nature of \mathbf{E} and \mathbf{H} .

Substituting the TEM Equations 2.25 and 2.26 into Equation 2.21 and computing the curl in spherical coordinates Equation 2.21 becomes:

$$\begin{aligned} & \hat{\mathbf{R}} \frac{1}{R \sin \theta} \left[\frac{\partial}{\partial \theta} \left(\frac{E_\phi e^{-jkR}}{R} \sin \theta \right) - \frac{\partial}{\partial \phi} \left(\frac{E_\theta e^{-jkR}}{R} \right) \right] \\ & + \hat{\boldsymbol{\theta}} \frac{1}{R} \left[-\frac{\partial}{\partial R} \left(R E_\phi \frac{e^{-jkR}}{R} \right) \right] + \hat{\boldsymbol{\phi}} \frac{1}{R} \left[\frac{\partial}{\partial R} \left(R E_\theta \frac{e^{-jkR}}{R} \right) \right] \\ & = \left[\hat{\boldsymbol{\theta}} H_\theta + \hat{\boldsymbol{\phi}} H_\phi \right] j\omega\mu \frac{e^{jkR}}{R}. \end{aligned} \quad (2.27)$$

Which reduces to:

$$\begin{aligned} & \hat{\mathbf{R}} \frac{1}{\sin \theta} \left[\frac{\partial}{\partial \theta} \left(\frac{E_\phi e^{-jkR}}{R} \sin \theta \right) - \frac{\partial}{\partial \phi} \left(\frac{E_\theta e^{-jkR}}{R} \right) \right] + \hat{\boldsymbol{\theta}} jk E_\phi e^{-jkR} - \hat{\boldsymbol{\phi}} jk E_\theta e^{-jkR} \\ & = \hat{\mathbf{R}} \left(\nabla \times \frac{\mathbf{E}_T}{R} \right)_R e^{-jkR} + \hat{\boldsymbol{\theta}} jk E_\phi e^{-jkR} - \hat{\boldsymbol{\phi}} jk E_\theta e^{-jkR} = \left[\hat{\boldsymbol{\theta}} H_\theta + \hat{\boldsymbol{\phi}} H_\phi \right] j\omega\mu e^{jkR}. \end{aligned} \quad (2.28)$$

From Equation 2.28 it can be seen that the curl of the electric field in the $\hat{\mathbf{R}}$ direction is equal to zero, and therefore:

$$\left(\nabla \times \frac{\mathbf{E}_T}{R} \right)_R = 0. \quad (2.29)$$

This is similar to the mathematical vector identity,

$$\nabla \times (\nabla \Phi) = 0, \quad (2.30)$$

which states that the curl of a gradient is equal to zero. In other words, if a vector field is curl free then it can be expressed as a gradient of a scalar field. As in electrostatics, the transverse electric field can be written as the gradient of the electric potential:

$$\frac{\mathbf{E}_T}{R} = -\nabla V. \quad (2.31)$$

Equation 2.31 is useful because the electric field on the surface of the aperture can now be found if the electric potential on the surface of the aperture is known. The electric potential can be found by solving Poisson's equation:

$$\nabla^2 V = -\frac{\rho}{\epsilon}, \quad (2.32)$$

which reduces to Laplace's equation,

$$\nabla^2 V = 0, \quad (2.33)$$

because there are no free charges on the aperture [Cheng, 1996]. Equation 2.33 can be solved using a number of different methods one being the Finite Element Method discussed in Chapter III.

D. FINDING THE APERTURE HEIGHT

Earlier the aperture height \mathbf{h}_a was defined in Equation 2.20 as:

$$\mathbf{h}_a = -\frac{f_g}{V_0} \iint_S \mathbf{E}_T(x, y, t) ds.$$

This surface integral can be rather difficult to solve depending on the geometry of the aperture. In order to compute a solution to this equation, the electric field is written as the gradient of a complex potential and cast into Green's theorem, which results in a rather simple contour integral.

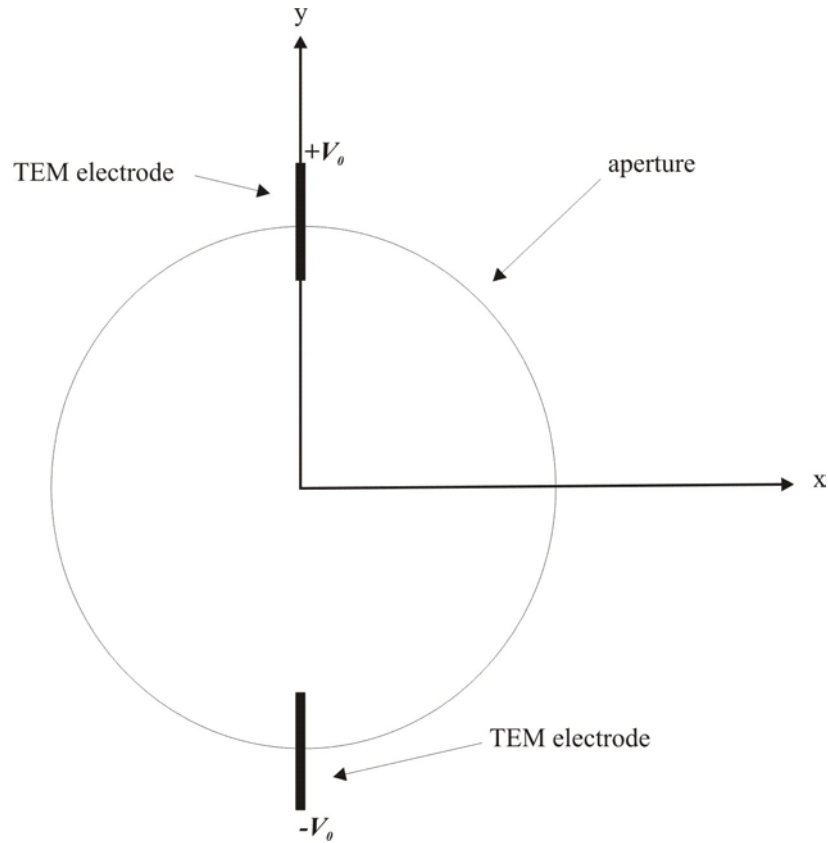


Figure 2.4. Two-dimensional view of an IRA.

Assume the feed electrodes of the IRA in Figure 2.4 are perfect electric conductors and have an electric potential V_0 between them. Also assume that there is no net charge on the two conductors. Essentially this is a two dimensional view of a transmission line and the voltage distribution on the plane of the aperture can be found by solving Laplace's Equation 2.33.

1. Stereographic Projection

The electric field on the surface of the aperture in Figure 2.4 is assumed to be created by a parallel feed electrode TEM transmission line. However, actual IRAs are usually excited by conical TEM transmission lines not parallel plate electrodes. So the resulting electric field has to be modified by a stereographic projection in order to produce accurate results. [Yang, 1977]

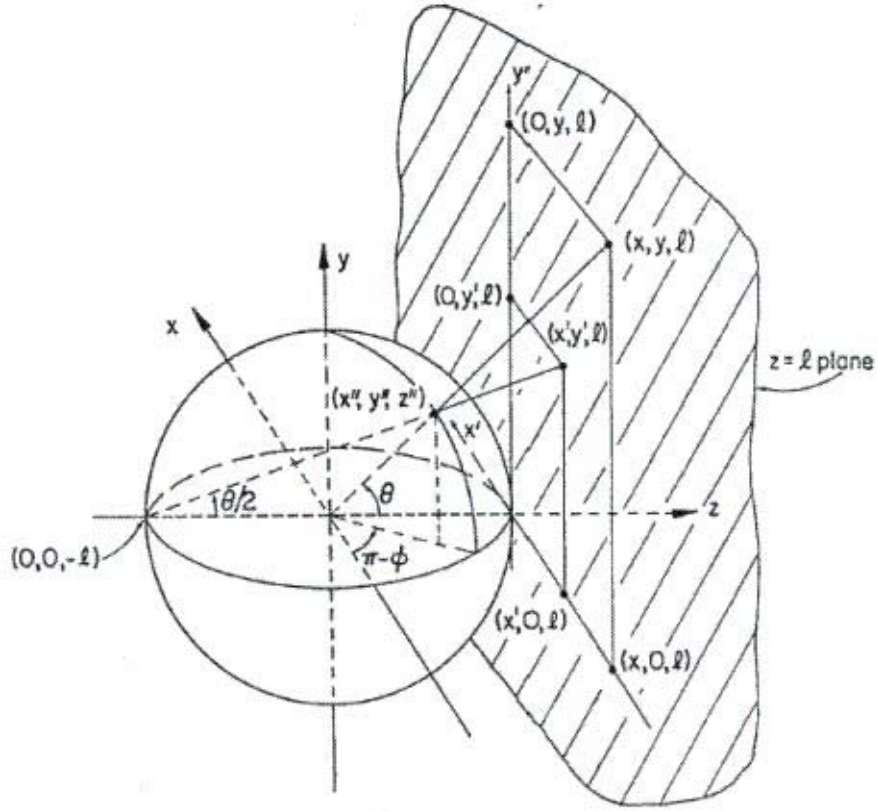


Figure 2.5. A 3-dimensional view of the stereographic projection. [From: Yang, 1977]

The stereographic projection, shown in Figure 2.5 will map points on the sphere to a corresponding point on the surface of the plane. A point described by (θ, ϕ) or (x'', y'', z'') on the surface of the sphere will be mapped to point (x', y') on the plane. Figure 2.6 shows the stereographic projection of a flat plate set of conical TEM feed electrodes.

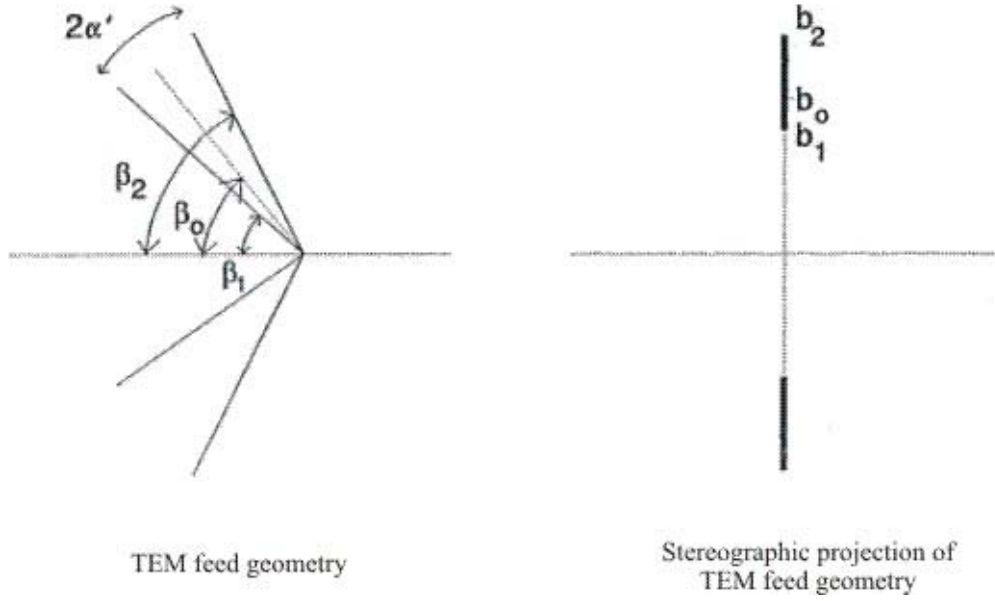


Figure 2.6. Stereographic projection of conical TEM feed electrodes. [After: Farr and Baum, 1992a]

Once the stereographic projection is carried out, the electric field on the surface of the aperture can be determined using the assumption of infinite length parallel plate electrodes.

2. Electric Field as the Gradient of a Complex Potential

The electric field on the surface of the aperture can be written as:

$$\mathbf{E}(x, y) = -\nabla V = -\frac{\partial V}{\partial x} \hat{\mathbf{x}} - \frac{\partial V}{\partial y} \hat{\mathbf{y}} = \mathbf{E}_x \hat{\mathbf{x}} + \mathbf{E}_y \hat{\mathbf{y}}. \quad (2.34)$$

Introducing the complex coordinate ζ ,

$$\zeta = x + jy, \quad (2.35)$$

and writing Equation 2.34 in terms of ζ the electric field is [Farr and Baum, 1995]:

$$\mathbf{E}(x, y) = E_c(\zeta) = E_x(\zeta) - jE_y(\zeta). \quad (2.36)$$

For a TEM mode wave propagating in the z -direction the analytic complex potential w is defined as:

$$w(\zeta) = u(\zeta) + jv(\zeta), \quad (2.37)$$

where $u(\zeta)$ is proportional the electric potential, $v(\zeta)$ is proportional to the magnetic potential and both are real analytic functions. Since $u(\zeta)$ is proportional to the electric potential it can be written as:

$$V(x, y) = \frac{V_0}{\Delta u} u(\zeta), \quad (2.38)$$

where Δu is the change in the electric potential parameter u between the two conductors in Figure 2.4. The electric field can now be written as:

$$E_c(\zeta) = E_x(\zeta) - jE_y(\zeta) = -\frac{V_0}{\Delta u} \left[\frac{\partial u}{\partial x} - j \frac{\partial u}{\partial y} \right]. \quad (2.39)$$

Applying the Cauchy-Riemann relationships [Brown and Churchill, 1996],

$$\frac{\partial u}{\partial x} = \frac{\partial v}{\partial y}, \quad \frac{\partial u}{\partial y} = -\frac{\partial v}{\partial x}, \quad (2.40)$$

Equation 2.39 can be written as:

$$E_c(\zeta) = -\frac{V_0}{\Delta u} \left[\frac{\partial u}{\partial x} + j \frac{\partial v}{\partial x} \right] = -\frac{V_0}{\Delta u} \frac{\partial w}{\partial \zeta}. \quad (2.41)$$

Other forms of Equation 2.41 using the Cauchy-Riemann Relationships are:

$$\begin{aligned} E_c(\zeta) &= -\frac{V_0}{\Delta u} \left[\frac{\partial u(\zeta)}{\partial \zeta} + j \frac{\partial v(\zeta)}{\partial \zeta} \right] = -\frac{V_0}{\Delta u} \left[\frac{\partial u(\zeta)}{\partial x} + j \frac{\partial v(\zeta)}{\partial x} \right] \\ &= -\frac{V_0}{\Delta u} \left[\frac{\partial u(\zeta)}{\partial x} - j \frac{\partial u(\zeta)}{\partial y} \right] = -\frac{V_0}{\Delta u} \left[\frac{\partial v(\zeta)}{\partial y} + j \frac{\partial v(\zeta)}{\partial x} \right]. \end{aligned} \quad (2.42)$$

3. Writing the Surface Integral as a Contour Integral

Now that the electric field can be written as the gradient of a complex potential, the surface integral in Equation 2.20 can be written as:

$$\iint_S \mathbf{E}_T(x, y) ds = \iint_S E_c(\zeta) dx dy = -\frac{V_0}{\Delta u} \iint_S \left[\frac{\partial u(\zeta)}{\partial x} - j \frac{\partial u(\zeta)}{\partial y} \right] dx dy. \quad (2.43)$$

Rewriting Equation 2.43 as follows:

$$-\frac{V_0}{\Delta u} \left[\iint_S \frac{\partial u(\zeta)}{\partial x} dx dy + \iint_S -j \frac{\partial u(\zeta)}{\partial y} dx dy \right] \quad (2.44)$$

and applying the following form of Green's Theorem to the integrals in Equation 2.44 [Brown and Churchill, 1996]:

$$\iint_S [Q_x - P_y] dx dy = \oint_C P dx + Q dy, \quad (2.45)$$

the following result is obtained:

$$\iint_S E_c(\zeta) ds = -\frac{V_0}{\Delta u} \left[\oint_C u dy + j \oint_C u dx \right]. \quad (2.46)$$

Substituting this result into Equation 2.20 the aperture height can be written as:

$$\mathbf{h}_a = -\frac{f_g}{V_0} \left[-\frac{V_0}{\Delta u} \left[\hat{\mathbf{x}} \oint_C u dy + \hat{\mathbf{y}} \oint_C u dx \right] \right]. \quad (2.47)$$

The geometric impedance f_g is equal to $\Delta u / \Delta v$ [Farr and Baum, 1995] so Equation 2.47 becomes:

$$\mathbf{h}_a = \frac{1}{\Delta v} \left[\hat{\mathbf{x}} \oint_C u dy + \hat{\mathbf{y}} \oint_C u dx \right]. \quad (2.48)$$

It has been shown that for the specific TEM feed geometry being studied, the x -component of the electric field on the aperture cancels out due to symmetry. [Baum, 1991] Because of this, the aperture height and resulting radiated electric field depends only on the y -component of the electric field. So Equation 2.20 reduces to:

$$h_a = -\frac{f_g}{V_0} \iint_S E_y(x, y; t) ds, \quad (2.49)$$

and Equation 2.48 reduces to:

$$h_a = \frac{1}{\Delta v} \oint_C u(x, y) dx \quad (2.50)$$

Equation 2.50 reduces the problem of determining the radiated electric field of an IRA to a simple contour integral. The contour integrated over is the boundary of the focusing aperture. In order to change the shape of the aperture all that needs to be done is change the contour that is integrated over. In order to optimize the radiated electric field,

this contour would only enclose portions of the aperture that has the y-component of the electric field orientated in the correct direction to contribute constructively to the radiated electric field.

THIS PAGE INTENTIONALLY LEFT BLANK

III. FINDING THE IDEAL APERTURE SHAPE

A. OVERVIEW

All of the electric field on an ideally shaped aperture will contribute constructively to the radiated electric field. In practice however, IRAs are typically made with circular cross section apertures with no consideration given to the orientation of the aperture electric field. To make the ideal aperture shape, the portions of the aperture that detract from the radiated field need to be found and removed.

Recall from Equation 2.15 that the radiated field along the bore sight of an IRA is proportional to the surface integral of the transverse electric field on the aperture of the antenna. For symmetrical TEM feeds, only portions of the aperture that have the y-component of the electric field less than zero will contribute constructively to the radiated electric field. [Baum, 1991] Therefore all that needs to be done is to remove the portions of the aperture that has a positive electric field y-component!

In order to accomplish this, the electric potential distribution on the aperture is found using the finite element method and a symmetry operator called reciprocation. Once the electric potential distribution is known, then the electric field can be found by taking a simple gradient of the electric potential distribution. Now that the electric field is known, a line is drawn where the y-component of the electric field is equal to zero. This boundary is called the ideal contour. The ideal aperture will contain the areas where the y-component of the electric field is negative and its boundary will be the ideal contour.

B. PROBLEM GEOMETRY

Figure 3.1a is a schematic diagram of the IRA being studied. The reflector is assumed to be paraboloidal with a focal length f and diameter D . The TEM feed consists of a pair crossed coplanar electrodes orientated clockwise at an angle of θ_o from the y-axis. The electrodes originate at the focal point of the paraboloidal and intersect the circle of symmetry. The circle of symmetry radius is denoted by a . The input impedance of the electrodes determines the values of b_1 and b_2 . Once f , D , θ_o , and input impedance are specified the values of β_0 , β_1 , β_2 , and a are as follows:

$$\beta_0 = \tan^{-1} \left[\frac{1}{2(f/D) - (D/8f)} \right], \quad (3.1)$$

$$\beta_1 = 2 \tan^{-1} \left[\sqrt{b_1/b_2} \tan(\beta_0/2) \right], \quad (3.2)$$

$$\beta_2 = 2 \tan^{-1} \left[b_2/b_1 \tan(\beta_1/2) \right]. \quad (3.3)$$

Recall from Chapter II that in order to calculate the aperture electric field, the TEM electrode geometry has to undergo a stereographic projection. Equations 3.4, 3.5, and 3.6 describe the antenna geometry after stereographic projection:

$$b_1 = \tan(\beta_1/2), \quad (3.4)$$

$$b_2 = \tan(\beta_2/2), \quad (3.5)$$

$$a = \sqrt{b_1 b_2}. \quad (3.6)$$

Figure 3.1b is a view of the IRA geometry after stereographic projection.

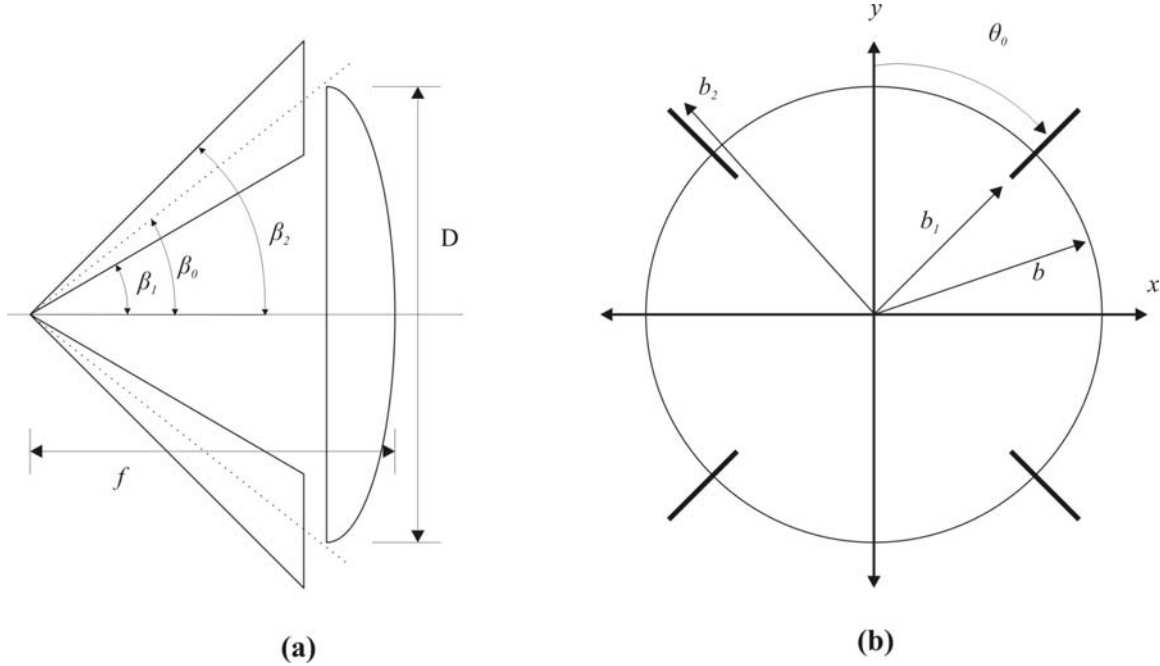


Figure 3.1. (a) Side view of the IRA being studied. (b) Front view of the IRA after stereographic projection.

1. Self-reciprocal Symmetry

To simplify calculations associated with many IRAs a two dimensional symmetry operator called reciprocation has been developed. [Farr and Baum, 1995] The reciprocation operator replaces a point in the original geometry with its reciprocal complex conjugate times a constant. For example a point described by the polar coordinates (r, θ) has the reciprocal point $(b^2/r, \theta)$. When using reciprocation, the original geometry is described as a complex number in Cartesian (x, y) or polar (Ψ, θ) coordinates:

$$\zeta = x + jy = \Psi e^{j\theta}. \quad (3.7)$$

After reciprocation all points ζ are mapped to new points ζ_2 . This is similar to reflecting an object through a circle centered at the origin of radius b , typically called the circle of symmetry. The new point is positioned at the same angle θ from the x-axis at a distance b^2 / Ψ from the origin. Equations 3.8 and 3.9 describe the reciprocation mapping. Points inside the circle of symmetry are mapped outside and points outside are mapped inside.

$$\begin{aligned} \zeta_2 &= x_2 + jy_2 = b^2 / \zeta^*, \\ \zeta_2 &= \Psi_2 e^{j\theta_2} \end{aligned} \quad (3.8)$$

$$\begin{aligned} x_2 &= b^2 / x, \\ y_2 &= b^2 / y, \\ \Psi_2 &= b^2 / \Psi, \\ \theta_2 &= \theta \end{aligned} \quad (3.9)$$

Figure 3.2 gives some examples of how various shapes are transformed by reciprocation. Straight lines are transformed into circles passing through the origin, circles passing through the origin transform to straight lines. Circles that do not pass through the origin transform to other circles, straight lines passing through the origin transform onto themselves.

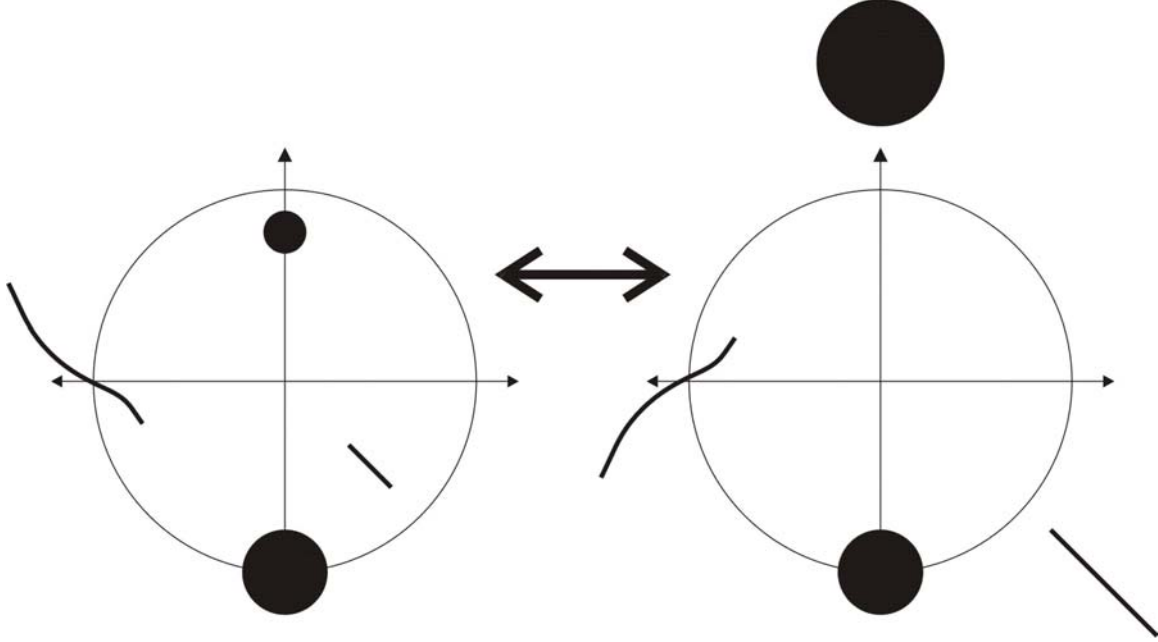


Figure 3.2. Some examples of two-dimensional structures and their reciprocals.

A structure that does not change after applying the reciprocation operator, such as the black circle at the bottom of Figure 3.2, is called a self-reciprocal structure. Some more examples of self-reciprocal structures are shown in Figure 3.3. Notice that the structure on right is the same as the feed structure of IRA being studied. Suppose that the shapes in Figure 3.3 are perfect electrical conductors with a potential difference between them. This is now a two-dimensional cross-section of a TEM feed and the static electric field between the conductors can be found by solving Laplace's equation as discussed in Chapter II.

To take advantage of self-reciprocal symmetry the potential is written in the complex plane as,

$$w(\zeta) = u(\zeta) + jv(\zeta), \quad (3.10)$$

where u is the electric potential and v is the magnetic potential. In a self-reciprocal IRA, the structure of the electrodes does not change after reciprocation, so the potential at a

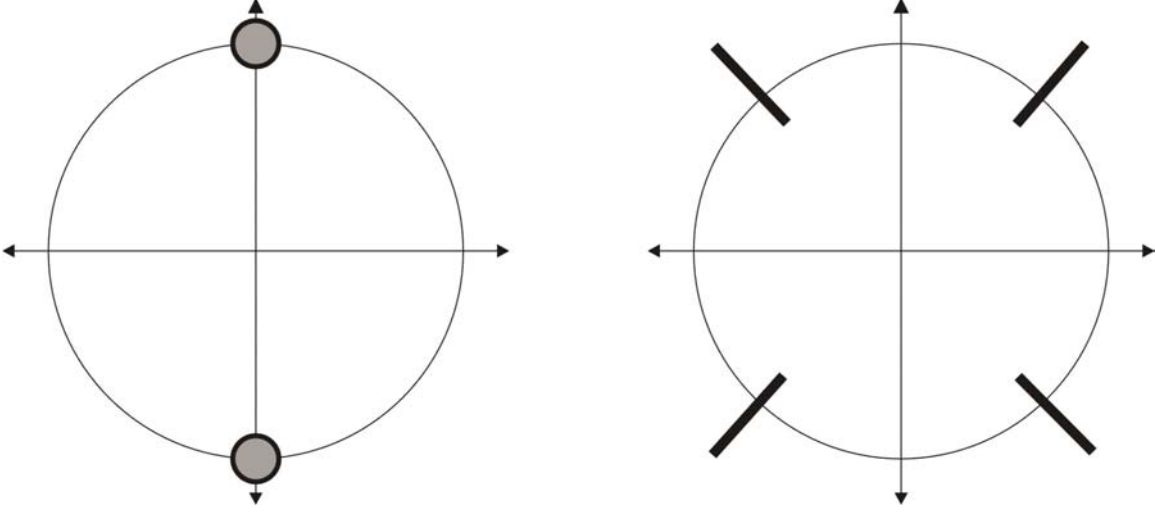


Figure 3.3. Some examples of self-reciprocal apertures. The structure on the right is the same as the IRA being studied in this paper.

point ζ is the same before and after the reciprocation. Written mathematically this is simply [Farr and Baum, 1995]:

$$w(\zeta) = w_2(\zeta). \quad (3.11)$$

This can also be expressed as the following, where v_0 is a real constant that is typically equal to zero [Farr and Baum, 1995]:

$$\begin{aligned} w(\zeta) &= w^*(\zeta_2) + jv_0, \\ u(\zeta) &= u(\zeta_2), \\ v(\zeta) &= -v(\zeta_2) + jv_0. \end{aligned} \quad (3.12)$$

The most significant result of Equation 3.12 is that the electric potential at any point ζ is equal to the electric potential at the reciprocal point ζ_2 . Recall from Equation 2.39 that the normalized electric field can be written as:

$$E(\zeta) = E_x(\zeta) - jE_y(\zeta) = -\frac{\partial u}{\partial x} + j\frac{\partial u}{\partial y}. \quad (3.13)$$

Applying the relationships in Equation 3.12 the electric field at ζ_2 is equal to [Farr and Baum, 1995]:

$$E(\zeta_2) = -E^*(\zeta) \frac{\zeta^{*2}}{b^2}. \quad (3.14)$$

2. Symmetry and Boundary Conditions

Due to symmetry considerations, only one quarter of the antenna is needed to find the radiated electric field. Since MATLAB PDE Toolbox Finite Element Method is used to compute the voltage distribution resulting from the TEM feed, this dramatically reduces the amount of computations that need to be accomplished. Figure 3.4 gives a qualitative view of how symmetry reduces the size of the finite element mesh needed.

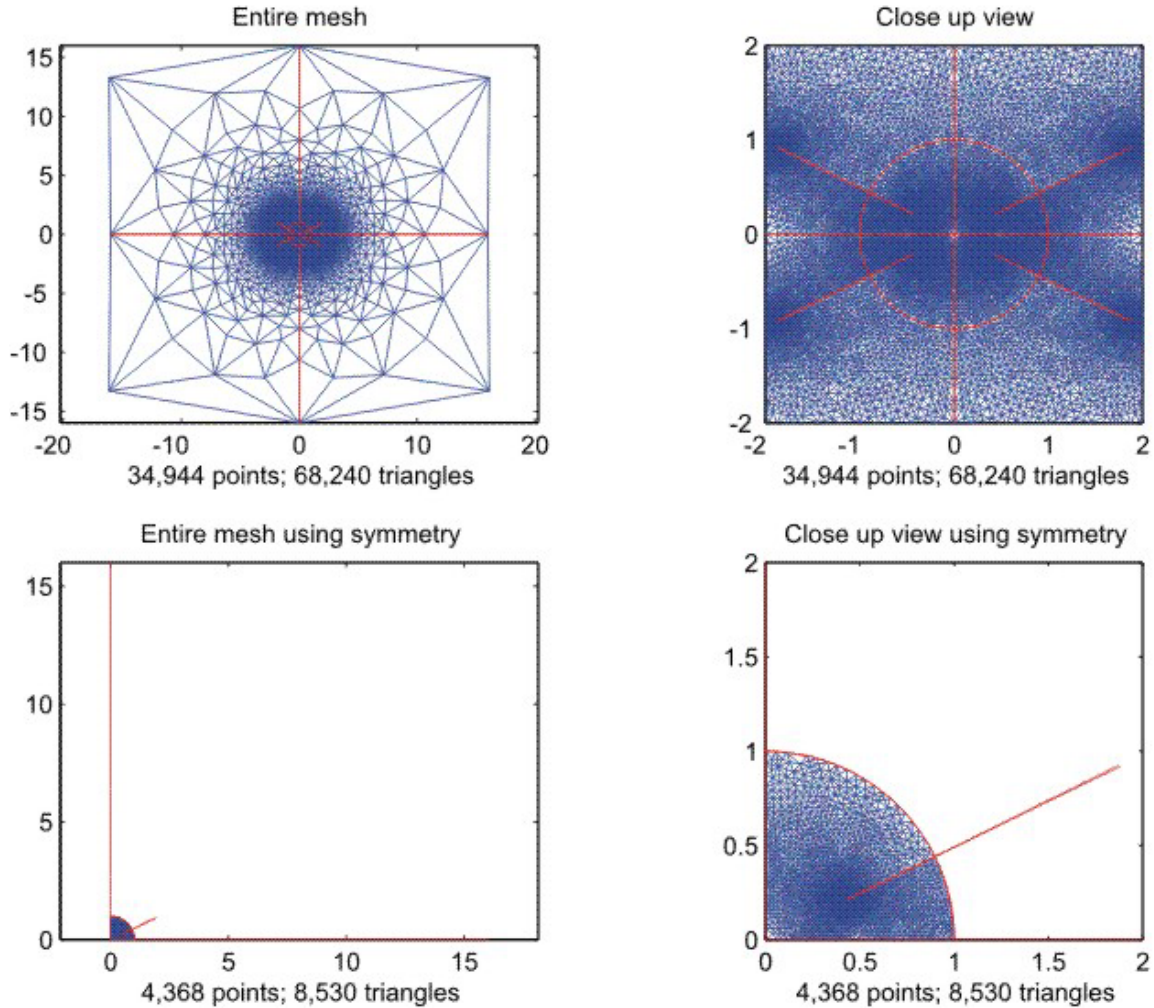


Figure 3.4. Taking symmetry into consideration reduces the amount of finite element triangles needed for reasonably accurate results from 68,240 to 8,530.

The electric potential on the TEM feed electrodes in the lower half of the IRA is equal to the negative of the electric potential of the electrodes in the upper half. This causes the IRA to be symmetric about the x-axis. Therefore, the x-axis can be treated as

a perfect electrical conductor where the tangential electric field and electric potential on the axis are both zero. The IRA is also symmetric about the y-axis because the electric potential on the TEM feed electrodes to the right of the y-axis is equal to the electric potential on the electrodes to the left. This allows the y-axis to be treated as a perfect magnetic conductor where the normal electric field is zero.

The circle of symmetry is a self-reciprocation boundary and is treated as a perfect magnetic conductor where the normal electric field is zero. This can be explained by

Equations 3.8 and 3.9 where a point ζ that is at an infinitesimally small distance inside the circle of symmetry will map to a point ζ_2 that is at an infinitesimally small distance outside the circle of symmetry at the same angle θ from the x-axis. Equation 3.12 shows that the electric potential at these two points is equal. Thus, the electric field between points ζ and ζ_2 , shown in Figure 3.5, can be written as:

$$\lim_{\Delta r \rightarrow 0} \frac{u(r + \Delta r/2) - u(r - \Delta r/2)}{\Delta r} = \frac{du}{dr} = E_{normal} = 0. \quad (3.15)$$

Because of this self-reciprocation boundary the electric potential and electric field need only be computed inside the circle of symmetry. The electric field and potential outside is easily found using Equations 3.12 and 3.14.

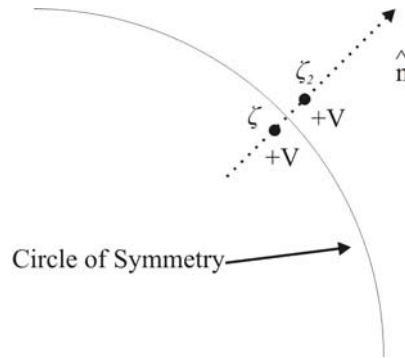


Figure 3.5. Illustration of why the electric field normal to the circle of symmetry is zero.

C. COMPUTING ELECTRIC POTENTIAL DISTRIBUTION

1. Aperture Voltage Distribution Using FEM

In the feed arm angle optimization study [Tyo, 1999] the electric potential distributions for 1,056 feed arm angle and size combinations were computed by the finite element method using MATLAB's PDE Toolbox. The electrode angles ranged from 3° to 87° measured clockwise from the y-axis. The electrode size is specified by the value for b_1 in Figure 3.1. The parameter b_2 is easily found using self-reciprocity symmetry. The values of b_1/b range from 0.2 to 0.97 units of length. The circle of symmetry radius and aperture boundary radius b are both equal to 1 unit of length. Figure 3.6 is the geometry and finite element mesh of one of these configurations. This is the 45-degree case with an electrode size b_1/b of 0.6424 units. The electrode is oriented straight up to simplify the MATLAB code used to create the boundaries.

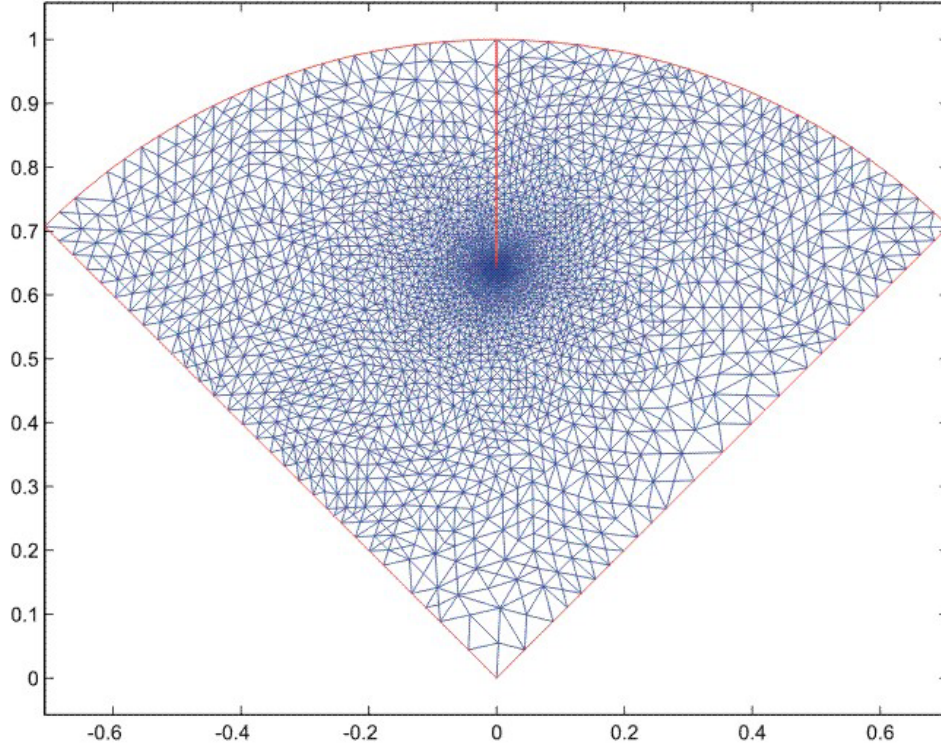


Figure 3.6. Finite Element mesh used to find the voltage distribution.

In order to make the problem more intuitive, the geometry is rotated so that the right boundary in Figure 3.6 lies on the x-axis and the left boundary lies on the y-axis.

This is accomplished by multiplying the PDE Toolbox point matrix by the simple linear algebra rotation matrix,

$$\begin{bmatrix} \cos(-\theta_0) & -\sin(-\theta_0) \\ \sin(-\theta_0) & \cos(-\theta_0) \end{bmatrix}, \quad (3.16)$$

and the resulting figure is shown in Figure 3.7. The solution computed by MATLAB's PDE toolbox is still valid because the finite element mesh and its associated boundary conditions remain unchanged, the only thing changed by the rotation matrix is its position relative to the x and y coordinate axes.

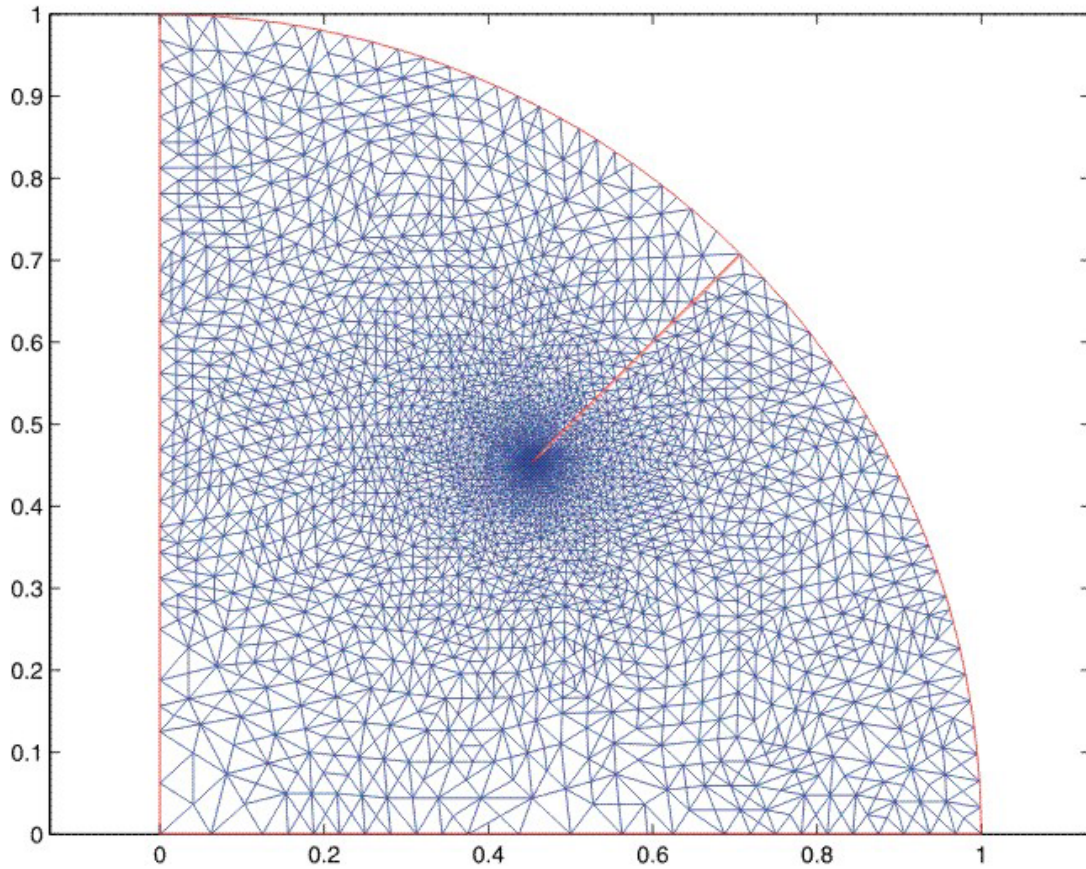


Figure 3.7. Finite element mesh after rotation.

The voltage distribution is computed at each point in the mesh by solving Laplace's equation $\nabla^2 V = 0$ with the boundary conditions contained in the symmetry discussion above.

Since the IRA TEM feed has self-reciprocal symmetry, the electric potential distribution outside the circle of symmetry can be found by performing a simple transformation similar to conformal mapping [Farr and Baum, 1995]. The mesh is mapped outside the geometry by applying the reciprocation operators in Equations 3.8 and 3.9 on the MATLAB finite element mesh. Figure 3.8 shows the newly mapped mesh. The electric potential is now known at every point in the mesh. Figure 3.9 is a contour plot of the IRA's voltage distribution.

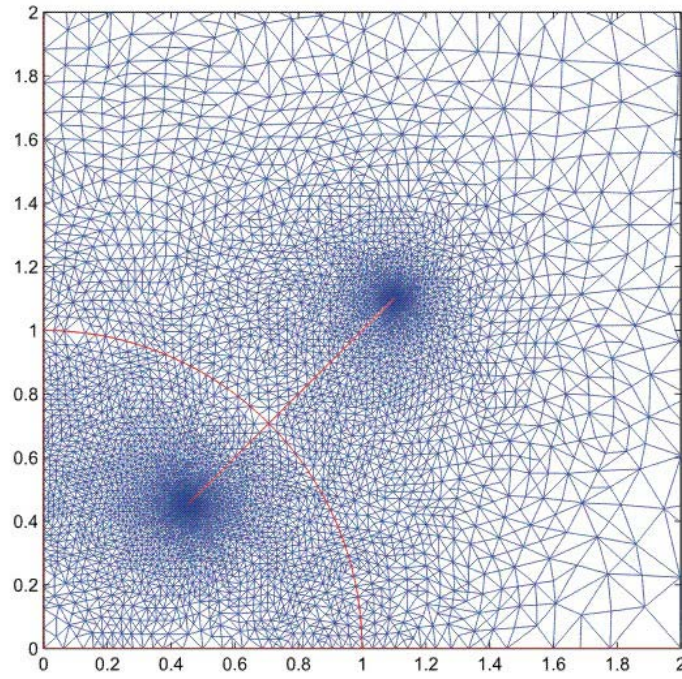


Figure 3.8. Finite element mesh outside the circle of symmetry created using self-reciprocity relationships

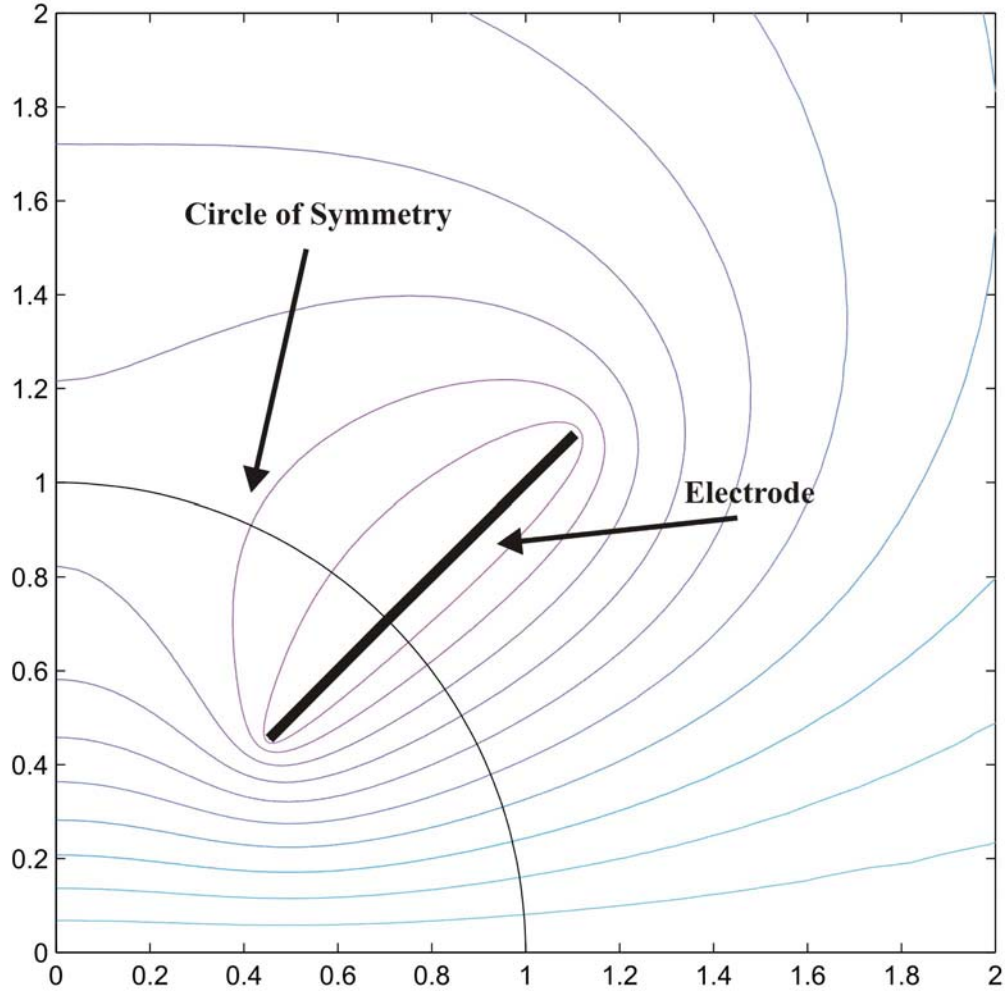


Figure 3.9. Contours of constant electric potential due to TEM feed electrode. The contours inside the circle of symmetry were calculated using finite element methods. The contours outside the circle of symmetry were found by self-reciprocation.

2. Contents of Data Files

Each of the data files contains the electric potential distribution stored in 10 different MATLAB variables. These variables contain the information in the following manner: (*xx* and *yy* identify the electrode angle/size combination)

- *bs* – the value in meters of b_l which is the distance from the origin to the inner tip of the electrode in the aperture plane.
- *e_xx_yy* – this is the PDE toolbox “edge matrix.” This variable identifies the points that lie on the boundary of the mesh used in the FEM analysis. Each column of this matrix represents one segment of the boundary edge. The first and second columns contain the point indices (columns of the point matrix) of the starting and ending point of that particular segment. The third and fourth

columns contain the voltage values at the starting and ending points. This fifth through seventh row contain information that identifies which boundary the line segment is on.

- $f_g_xx_yy$ – this is the geometric impedance of the electrode configuration. To find the impedance multiply f_g by 377.

$$Z = \sqrt{\mu_0 / \epsilon_0} f_g = 120\pi f_g \approx 377 f_g \quad (3.17)$$

- p_xx_yy – PDE toolbox “point matrix.” Each column in this matrix represents one point in the finite element mesh. The first row is the x-coordinate and the second row is the y-coordinate.
- t_xx_yy – PDE toolbox “triangle matrix.” The first three rows contain indices to the corner points (columns in the point matrix), given in counter clockwise order of each triangle in the mesh.
- $theta$ – angle of the electrode θ_o
- u_xx_yy – Solution to Laplace’s equation, it is the electric potential at every point in the mesh. Each column corresponds to the corresponding point index.

The electrode size and angle coefficients are shown in Table 3.1. The position of the start of the electrode can be found with the following equation:

$$start = b_l e^{\pi/2 - \theta}. \quad (3.18)$$

The angle θ is measured clockwise from the vertical, b_l is the value from Equation 3.4, and the electrode length is the length of the self-reciprocal electrode.

<i>xx, yy</i> Coeff	<i>b1</i>	Electrode Length	angle theta	<i>xx, yy</i> Coeff	<i>b1</i>	Electrode Length	angle theta
1	0.020	49.980	87.000	19	0.610	1.029	34.862
2	0.053	18.815	84.103	20	0.642	0.916	31.966
3	0.086	11.542	81.207	21	0.675	0.807	29.069
4	0.118	8.357	78.310	22	0.708	0.704	26.172
5	0.151	6.472	75.414	23	0.741	0.609	23.276
6	0.184	5.251	72.517	24	0.773	0.521	20.379
7	0.217	4.391	69.621	25	0.806	0.435	17.483
8	0.249	3.767	66.724	26	0.839	0.353	14.586
9	0.282	3.264	63.828	27	0.872	0.275	11.690
10	0.315	2.860	60.931	28	0.904	0.202	8.793
11	0.348	2.526	58.034	29	0.937	0.130	5.897
12	0.380	2.252	55.138	30	0.970	0.061	3.000
13	0.413	2.008	52.241	31			45.000
14	0.446	1.796	49.345	32			75.000
15	0.479	1.609	46.448	33			60.000
16	0.511	1.446	43.552	34			30.000
17	0.544	1.294	40.655	35			15.000
18	0.577	1.156	37.759				

Table 3.1. Parameter values for different IRA configurations

3. Two-dimensional Aperture Voltage Distribution Using Gauss's law

In the previous section the electric potential was found at every point in the mesh. However, to evaluate Equation 2.50 along the ideal contour it is necessary to know the electric potential at points not located on the matrix. This could be done by interpolation from the known points in the mesh. This is an extremely difficult task given the format of the MATLAB PDE toolbox output. However, it is relatively easy to find the electric charge on the electrodes using the PDE toolbox output. This allows the use of Gauss' Law to find the electric potential distribution. Gauss's Law states that the total outward flux of the electric field over any closed surface in free space is equal to the total charge enclosed by the surface divided by the electrical permittivity (ϵ_0) [Cheng, 1989]:

$$\oint_S \mathbf{E} \cdot d\mathbf{s} = \frac{Q_{enc}}{\epsilon_0}. \quad (3.19)$$

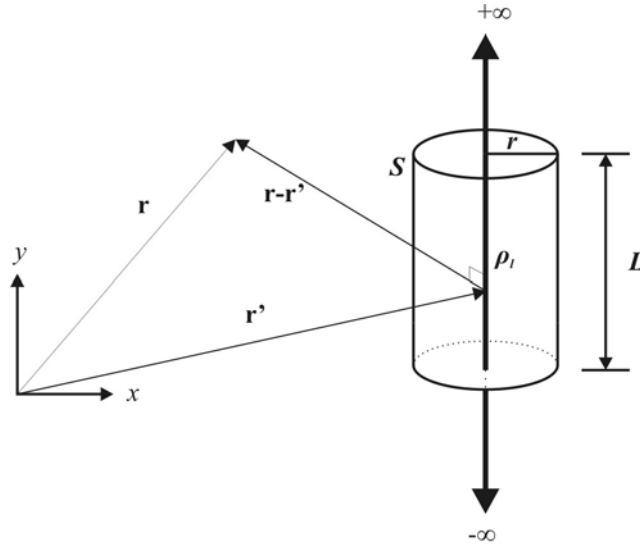


Figure 3.10. Infinite length line charge surrounded by surface S .

Suppose the electric field \mathbf{E} is due to a line of charge of length L with a charge density of ρ_l , as in Figure 3.10. Enclosing the line charge with surface S and using cylindrical coordinates the electric field magnitude, $E(r)$ at a radial distance r can be written as:

$$E(r)2\pi|\mathbf{r}-\mathbf{r}'|L = \frac{\rho_l L}{\epsilon_0}, \quad (3.20)$$

where the primed vectors refer to the source objects. Canceling out the length L , rearranging and writing in vector form, Equation 3.21 gives us the electric field due to a line charge of finite length:

$$\mathbf{E} = \frac{\rho_l}{2\pi\epsilon_0 r} \hat{\mathbf{R}}, \quad (3.21)$$

with $\hat{\mathbf{R}}$ defined as:

$$\begin{aligned} \mathbf{R} &= \mathbf{r} - \mathbf{r}', \\ \hat{\mathbf{R}} &= \frac{\mathbf{R}}{R} \\ R &= |\mathbf{R}| = |\mathbf{r} - \mathbf{r}'|. \end{aligned} \quad (3.22)$$

The electric potential V between points b and a is written as:

$$V(b) - V(a) = -\int_a^b \mathbf{E} \cdot d\mathbf{l} \quad (3.23)$$

Substituting Equation 3.21 for \mathbf{E} and the cylindrical coordinate representation $dr\hat{\mathbf{R}}$ for $d\mathbf{l}$ into Equation 3.23 results:

$$V(b) - V(a) = -\int_a^b \frac{\rho_l}{2\pi\epsilon_0 r} \hat{\mathbf{R}} \cdot dr\hat{\mathbf{R}} \quad (3.24)$$

Carrying out the dot product and solving the integral:

$$V(b) - V(a) = -\frac{\rho_l}{2\pi\epsilon_0} \int_a^b \frac{1}{r} dr = -\frac{\rho_l}{2\pi\epsilon_0} [\ln(b) - \ln(a)] \quad (3.25)$$

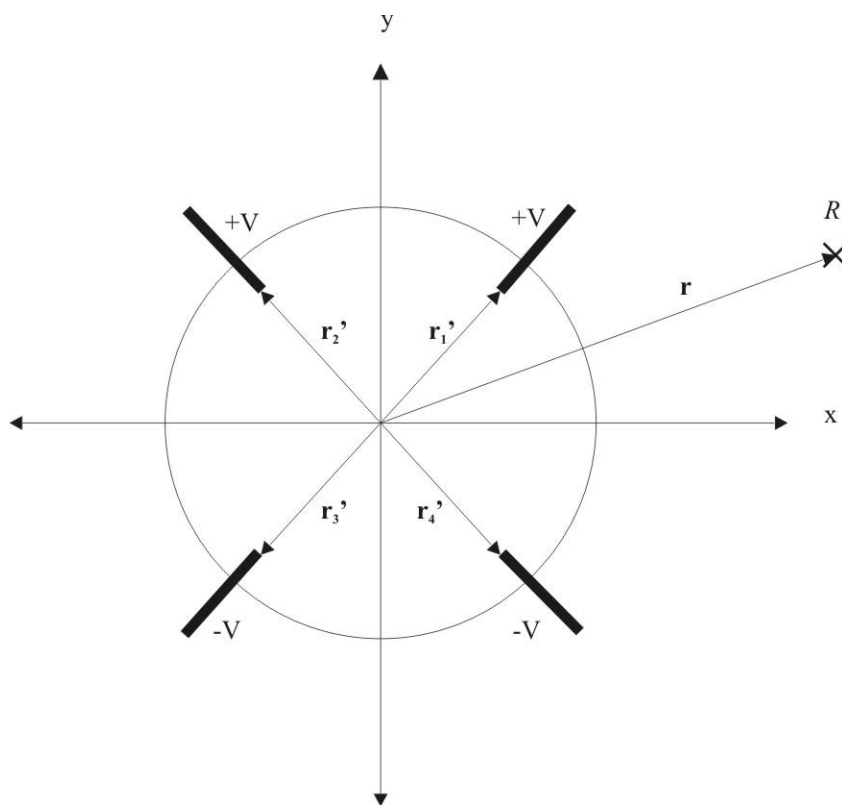


Figure 3.11. Gauss' Law is being used to find the electric potential at point R due to the four electrodes. Each electrode is treated as an infinite plate coming out and going into the page that is broken up into an infinite amount of line charges. The vector \mathbf{r}' points to one of the infinite length line charges.

In Figure 3.11 \mathbf{r} identifies the point R where the electric potential needs to be determined. The vector \mathbf{r}' identifies the location of the charge. The electric potential at

R with respect to ∞ is V_R . Using Equation 3.25 to find the electric potential results in the following:

$$V(R=|\mathbf{r}-\mathbf{r}'|)-V(\infty)=-\frac{\rho_l}{2\pi\epsilon_0}\int_{\infty}^{|\mathbf{r}-\mathbf{r}'|}\frac{1}{r}dr=-\frac{\rho_l}{2\pi\epsilon_0}\left[\ln(|\mathbf{r}-\mathbf{r}'|)-\ln(\infty)\right]. \quad (3.26)$$

This equation blows up because of the $\ln(\infty)$ term. To get around this, we write the electric potential at the origin (which we know is zero for the IRA because of symmetry) with respect to the electric potential at $R=\infty$ as:

$$V(|\mathbf{r}'|)-V(\infty)=\frac{-\rho_l}{2\pi\epsilon_0}\int_{\infty}^{|\mathbf{r}'|}\frac{1}{r}dr=\frac{-\rho_l}{2\pi\epsilon_0}\left[\ln(|\mathbf{r}'|)-\ln(\infty)\right]. \quad (3.27)$$

The electric potential at R referenced to the electric potential at the origin is:

$$\begin{aligned} V &= V_R - V_0 = \frac{-\rho_l}{2\pi\epsilon_0}\left[\ln(|\mathbf{r}-\mathbf{r}'|)-\ln(\infty)-\ln(|\mathbf{r}'|)+\ln(\infty)\right], \\ V &= \frac{-\rho_l}{2\pi\epsilon_0}\left[\ln(|\mathbf{r}-\mathbf{r}'|)-\ln(|\mathbf{r}'|)\right]. \end{aligned} \quad (3.28)$$

When taking all four electrodes in Figure 3.11 into account Equation 3.28 becomes for one ‘piece’ of the electrode (and its counterparts in the other three electrodes) is:

$$\begin{aligned} V &= \frac{-\rho_l}{2\pi\epsilon_0}\left[\ln(|\mathbf{r}-\mathbf{r}_1'|)+\ln(|\mathbf{r}-\mathbf{r}_2'|)-\ln(|\mathbf{r}-\mathbf{r}_3'|)-\ln(|\mathbf{r}-\mathbf{r}_4'|)\right], \\ V &= \frac{-\rho_l}{2\pi\epsilon_0}\left[\ln\left(\frac{|\mathbf{r}-\mathbf{r}_1'|\|\mathbf{r}-\mathbf{r}_2'\|}{|\mathbf{r}-\mathbf{r}_3'|\|\mathbf{r}-\mathbf{r}_4'\|}\right)\right]. \end{aligned} \quad (3.29)$$

Writing Equation 3.29 in terms of x and y coordinates:

$$\begin{aligned} V &= \frac{-\rho_l}{2\pi\epsilon_0}\left[\ln\left(\frac{\sqrt{(x-x_1')^2+(y-y_1')^2}\sqrt{(x-x_2')^2+(y-y_2')^2}}{\sqrt{(x-x_3')^2+(y-y_3')^2}\sqrt{(x-x_4')^2+(y-y_4')^2}}\right)\right], \\ V &= \frac{-\rho_l}{4\pi\epsilon_0}\left[\ln\left(\frac{\left((x-x_1')^2+(y-y_1')^2\right)\left((x-x_2')^2+(y-y_2')^2\right)}{\left((x-x_3')^2+(y-y_3')^2\right)\left((x-x_4')^2+(y-y_4')^2\right)}\right)\right]. \end{aligned} \quad (3.30)$$

The line charge density ρ_l in Equation 3.30 was found using the results of the MATLAB finite element method. Figure 3.12 is a portion of one of the electrodes showing the FEM triangles bordering it. The electric field \mathbf{E} is known via the finite

element solution at the centers of the triangles. By Gauss's law the surface charge density in each triangle is equal to:

$$\rho_s = |\mathbf{E}| \epsilon_0. \quad (3.31)$$

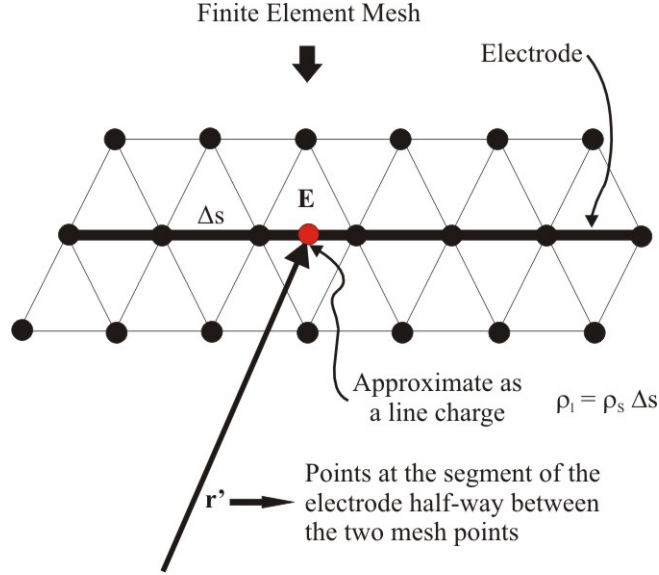


Figure 3.12. Close up view of the finite element mesh along on of the electrodes. Each segment of the electrode is being approximated by an infinite line charge coming out of the page, located at the center of the electrode.

Equation 3.30 can be solved numerically if it is written in the following form:

$$V \approx \sum_n \frac{-\rho_{s,n} \Delta s_n}{4\pi\epsilon_0} \left[\ln \left(\frac{\left((x-x_{1,n}')^2 + (y-y_{1,n}')^2 \right) \left((x-x_{2,n}')^2 + (y-y_{2,n}')^2 \right)}{\left((x-x_{3,n}')^2 + (y-y_{3,n}')^2 \right) \left((x-x_{4,n}')^2 + (y-y_{4,n}')^2 \right)} \right) \right], \quad (3.32)$$

where n is the number of electrode “segments” shown in Figure 3.12, q_n is the charge on each segment, Δs_n is the length of each segment and (x_n', y_n') is the position of the center of each electrode segment.

3. Comparing FEM Distribution to Gauss's Law

The FEM and Gauss's Law solutions discussed above are intimately related through the charge on the electrodes. It is useful to compare the two to help determine the amount of error that the two solutions may contribute. Notice in Figure 3.13 that the maximum difference between the two is about 1.3%.

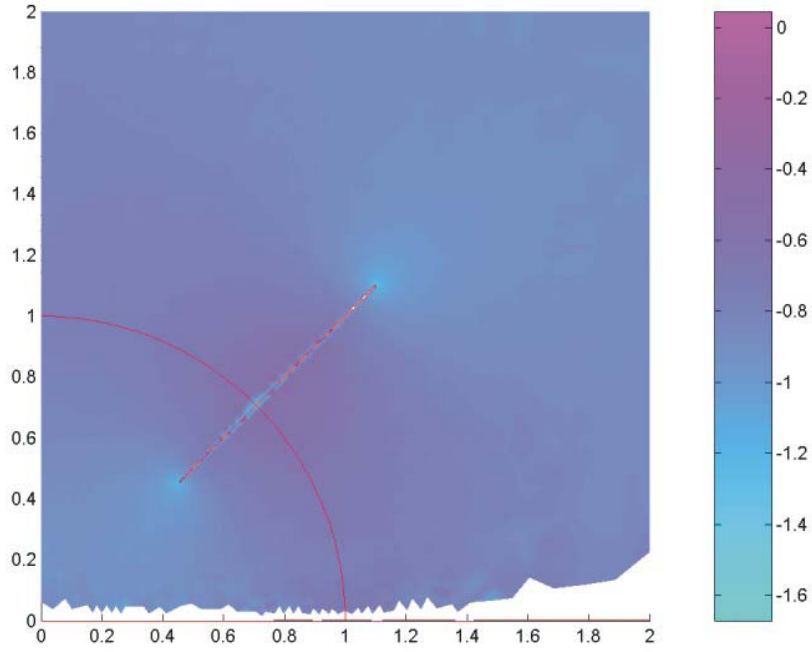


Figure 3.13. Plot of the percent difference between the electric potential distribution calculated by the finite element method and the by Gauss' Law. The white areas at the bottom are caused by divide by zero errors. The electric potential along the x-axis is zero, so the electric potential in the triangles bordering the x-axis is also zero.

D. FINDING THE IDEAL CONTOUR

Now that the electric potential distribution is known, the electric field can be easily computed by taking the gradient of the distribution:

$$\mathbf{E} = -\nabla V \quad (3.33)$$

MATLAB's PDE Toolbox has a built in function, *pdegrad*, which can compute the gradient of a finite element mesh. Figure 3.14 shows the electric field lines for one IRA electrode size and angle combination.

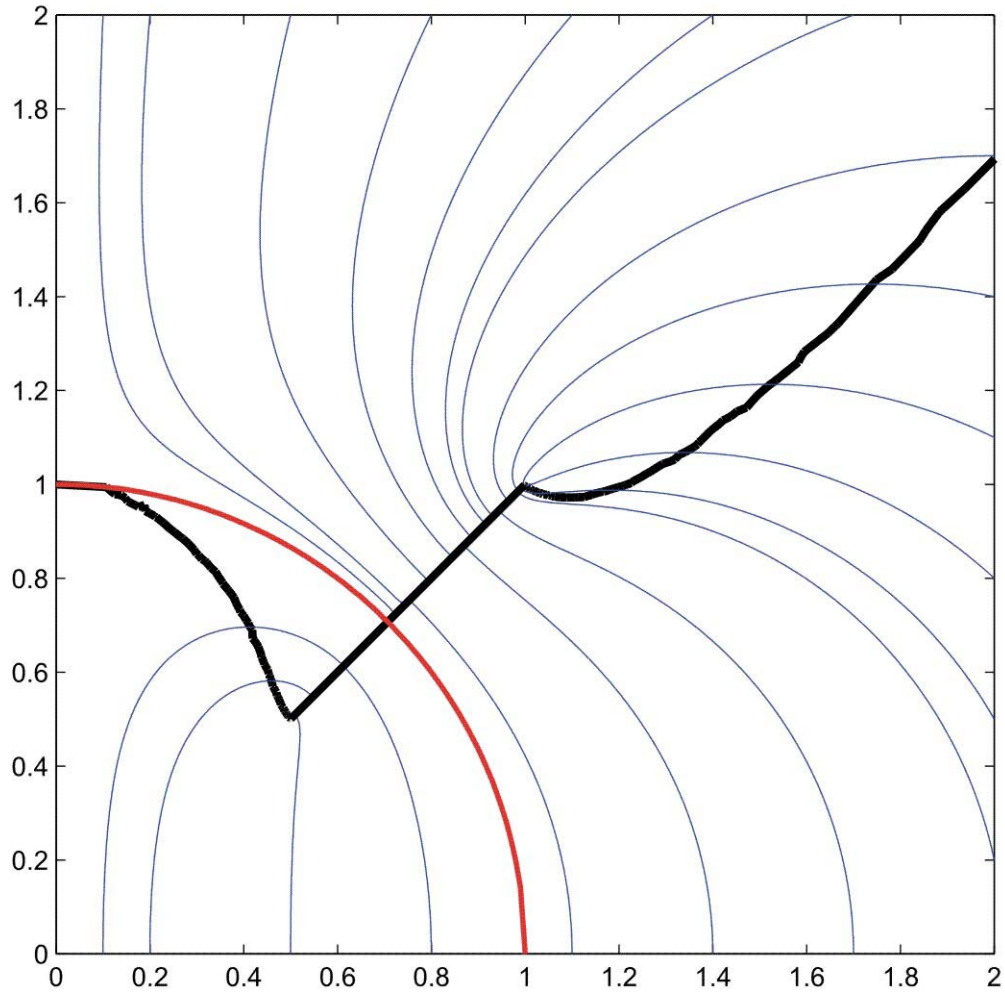


Figure 3.14. IRA showing electric field lines in blue and the ideal contour in black and the circle of symmetry in red.

Once the electric field is known, it is a trivial matter to find out the areas where E_y is orientated in the wrong direction. The bold line in Figure 3.14 is where $E_y = 0$ and is referred to as the ideal contour, as E_y is orientated in the wrong direction above the ideal contour and E_y in the correct direction below. This line was plotted using the MATLAB command *pdecont*. Each electrode size and angle combination will produce a slightly different ideal contour similar in shape to the one in Figure 3.14 as can be seen in Figure 3.15.

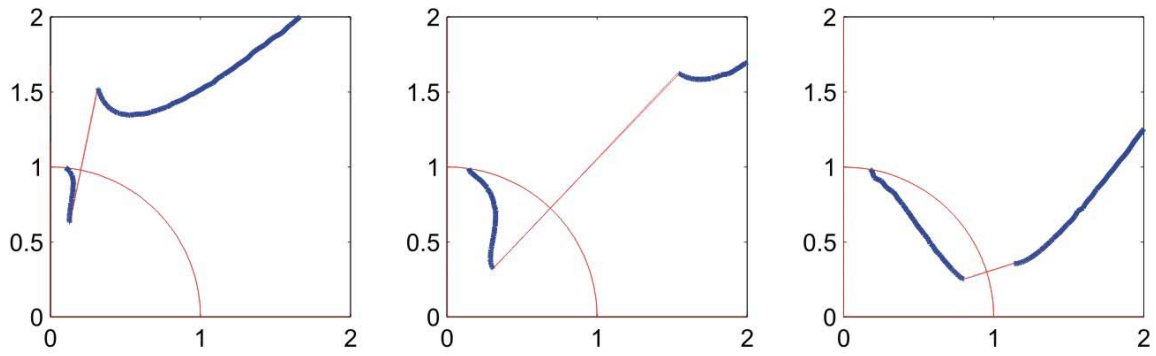


Figure 3.15. Some examples of Ideal Contours for different electrode size and angle combinations. The entire area below the ideal contour contains aperture electric field that will contribute constructively to the radiated electric field.

IV. DETERMINEING THE OPTIMUM CIRCULAR APERTURE

A. OVERVIEW

In Chapter III the ideal contour was found for a given TEM feed size and angle configuration. For most IRA applications, the aperture size is fixed and normally has the same outer dimensions as the circle of symmetry. The maximum possible radiated field from a given aperture and electrode configuration will result by projecting the ideal contour onto the aperture and eliminating the parts of the aperture outside the ideal contour. For a given aperture size, the response can be improved by optimizing the position of the circle of symmetry relative to the maximum aperture size while forcing the aperture boundary to follow the ideal contour. Figure 4.1 shows a number of different ideal aperture shapes relative to the circle of symmetry. [Baretela and Tyo, 2001]

The aperture height h_a is a useful tool to find the optimum position of the circle of symmetry relative to the aperture boundary. A high magnitude for h_a is desired since it is proportional to the prompt radiated electric field. In this chapter, the aperture height is numerically computed for a number of electrode size and angle configurations,

B. CALCULATE THE APERTURE HEIGHT

In Chapter II it was shown that the aperture height, h_a , is proportional to the radiated electric field. Recall from Equation 2.50 that h_a is equal to the contour integral along the boundary of the aperture C of the electric potential u :

$$h_a = \frac{1}{\Delta v} \oint_C u(x, y) dx,$$

where Δv is the magnetic potential discussed in Chapter II and is equal to the total charge on the positive electrodes.

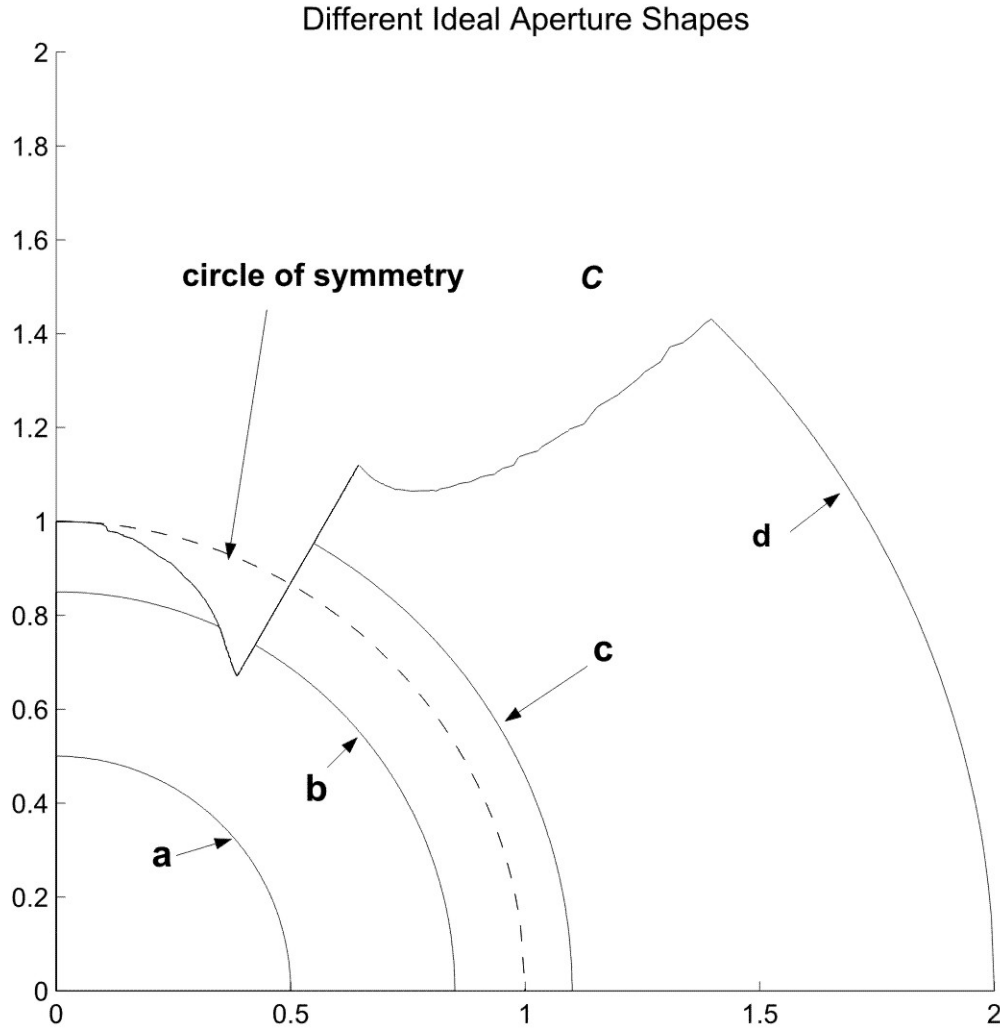


Figure 4.1. There are four possible relationships between the circle of symmetry C and the maximum radius R: a) R inside C and inside the inner edge of the electrode, b) R inside C and intersecting the electrode, c) R outside C and intersecting the electrode, d) R outside the electrode. [From: Baretela and Tyo, 2001]

1. Numerically Computing the Aperture Height h_a

As an example, h_a is calculated for the circular aperture in Figure 4.2. This is a good example because it shows how the integral is computed for all possible locations of the ideal boundary. There is (1) a portion along the circle of symmetry, (2) a portion along the ideal contour inside the circle of symmetry, (3) a portion along the electrode, (4) a portion along the ideal contour outside the circle of symmetry and (5) a portion outside the circle of symmetry that does not follow the ideal contour.

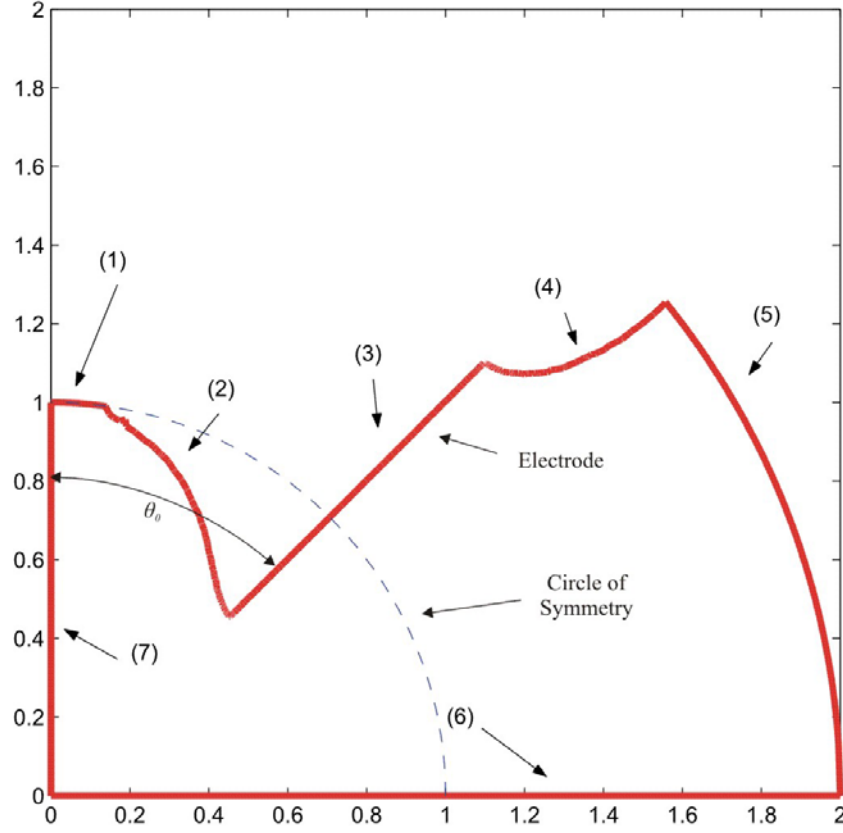


Figure 4.2. Circular shaped aperture that follows the ideal contour with and outer radius larger than the circle of symmetry.

Along the x-axis (6) the contribution to h_a is zero because the electric potential u is zero. On the y-axis (7), the contribution to h_a is zero because dx is zero on the y-axis. Along the electrode (3) the electric potential u is equal to one volt, therefore the contribution to h_a is equal to the length of the electrode $l_{electrode}$ projected onto the x-axis divided by Δv :

$$\begin{aligned}
 h_{a6} &= \frac{1}{\Delta v} \int_{C_6} (0) dx = 0 \\
 h_{a7} &= \frac{1}{\Delta v} \int_{C_7} u(x)(0) = 0 \\
 h_{a3} &= \frac{1}{\Delta v} \int_{C_5} (1) dx = \frac{(l_{electrode}) \sin(\theta_0)}{\Delta v},
 \end{aligned} \tag{4.1}$$

where θ_0 is measured as in Figure 3.1.

It is more complicated to calculate h_a for the other segments (1,2,4,5) on the ideal contour because the electric potential $u(x)$ is not easily found. These segments do not have simple boundary conditions as (6,7) or lie on points included in the finite element mesh that was used to compute the electric potential. Additionally, segments (1,5) are arcs of a circle, while segments (2,4) are complicated contours without a known analytic description.

Figure 4.3 describes how segment (2)'s contribution to h_a was calculated using the approximation in Equation 4.2:

$$h_{a2} \approx \frac{1}{\Delta V} \sum_{n=1}^m u(n) \Delta x_n. \quad (4.2)$$

Recall from Chapter III that the ideal contour was found using the MATLAB command *pdecont*. In addition to drawing a line where $E_y = 0$, *pdecont* divides this line into m pieces identified by starting and ending x and y coordinates. The electric potential at the start and end of each piece is found using Equation 3.30. The electric potential $u(n)$ for each piece is then approximated by averaging the start and end electric potential values. The length of each piece in the x-direction Δx_n is found by subtracting the x-coordinate of the starting point from the x-coordinate of the ending point. Note that Δx_n could take on a positive or negative value. This same method is used to solve for the contribution from segment (4).

The remaining two segments (1) and (5) in Figure 4.2 are arcs of circles centered at the origin. Segment (1) lies on the circle of symmetry starting at the y-axis and ending at the beginning of segment (2). Segment (5) begins at the end of segment (4) and ends

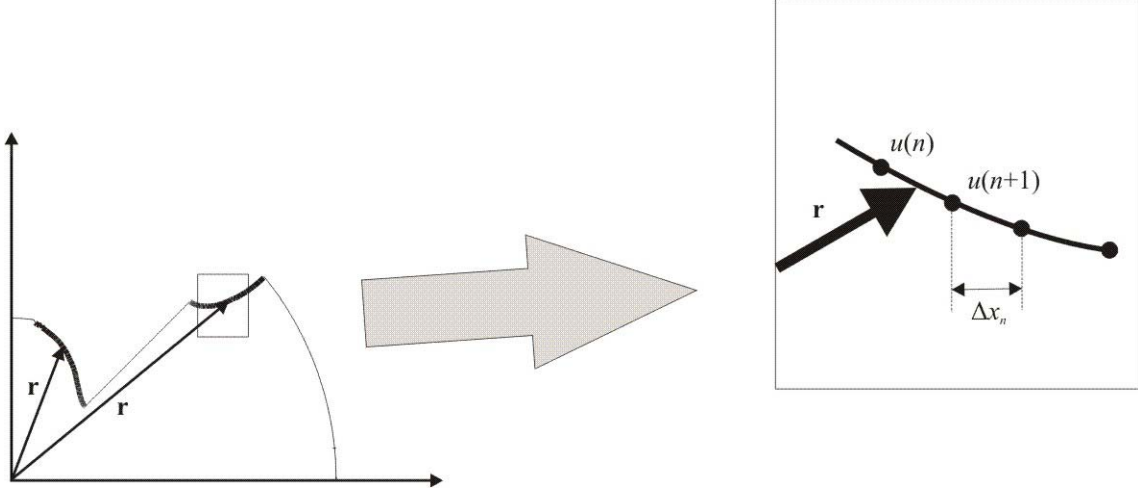


Figure 4.3. This is an enlarged view of the portions of the ideal contour calculated by the MATLAB *pdecont* command. The ideal contour is divided into m segments identified by starting and ending x-y coordinates. The contribution to h_a is found by summing the average electric potential of each piece multiplied by the length of each piece in the x-direction.

at the x-axis. The radius of the arc for segment (5) is a constant specified by the overall size desired for the IRA. Figure 4.4 describes how h_a is calculated for segment (1) using the approximation in Equation 4.3.

$$h_{a1} \approx \frac{1}{\Delta V} \sum_{n=1}^{100} u(n) \Delta x \quad (4.3)$$

The segment is divided into 100 equal sized pieces and Δx_n is length of each piece projected onto the x-axis. One hundred pieces was chosen so that there would be a small enough Δx_n to obtain accurate results, while keeping the number of computations needed low. The electric potential $u(n)$ for each piece is found in the same manner as was used for segments (2) and (4). Equation 4.3 is also used to find the contribution to the aperture height from segment (5).

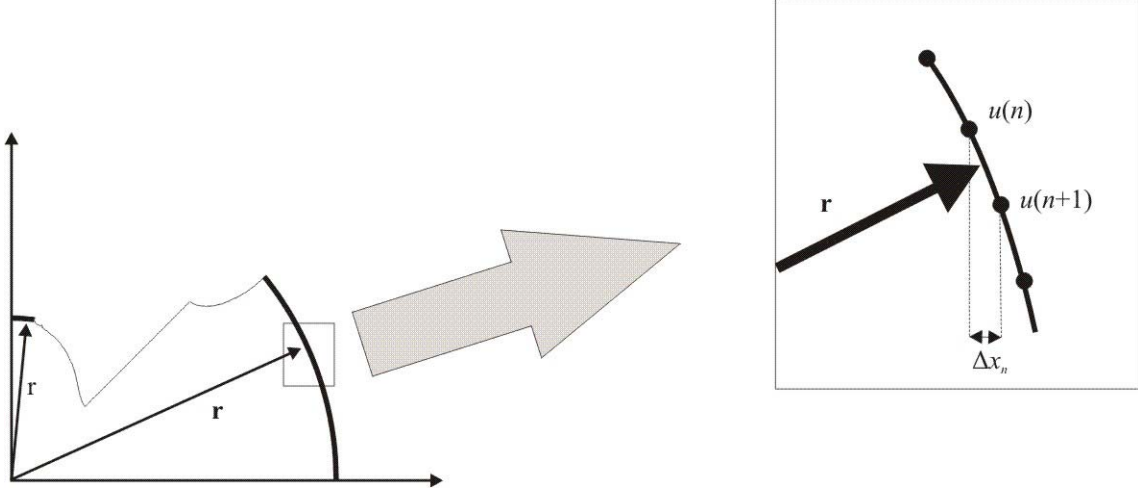


Figure 4.4. This is an enlarged view of the portions of the ideal contour where the geometry is easily identified. The ideal contour is divided into 100 equally sized pieces. The contribution to h_a is found by summing the average electric potential of each piece multiplied by the length of each piece in the x-direction.

The value of h_a for the contour in Figure 4.2 is found by adding the contributions to h_a for each segment:

$$h_a = 4(h_{a1} + h_{a2} + h_{a3} + h_{a4} + h_{a5} + h_{a6} + h_{a7}) \quad (4.4)$$

The sum is multiplied by 4 because the value of h_a was computed for only one quarter of the antenna due to symmetry considerations.

2. Comparing Numerical Value of h_a to an Analytic Form Solution

The Analytic solution to Equation 2.50 for a TEM feed arm angle $\theta_0 = 45^\circ$ is [Farr, 1993]:

$$h_a = \frac{\pi m^{-1/4}}{2\sqrt{2}K(1-m)} \left[1 - \frac{2}{\pi} \sin^{-1} \left(\frac{(1-m^{1/2})^2}{1-m} \right) \right]. \quad (4.5)$$

K is a complete elliptic integral of the first kind with parameter m is given as:

$$m = \left(\frac{b_1}{b_2} \right)^2, \quad (4.6)$$

where b_1 and b_2 define the electrode size and can be found in Equations 3.4 and 3.5. Analytic solutions for θ_0 other than 45° have not been found.

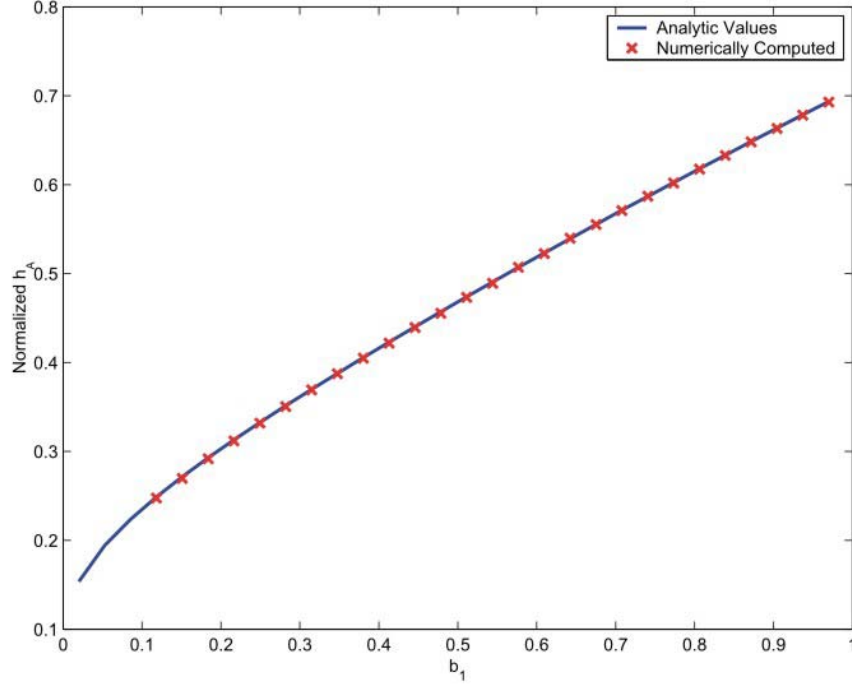


Figure 4.5. Comparison of analytic solution for h_a to the numerically computed one. The Analytic solution is for the $\theta_0 = 45^\circ$ case. The aperture height is normalized by the radius of the circle of symmetry.

As seen in Figure 4.5, the value of h_a computed using Equation 4.4 follows the analytical solution calculated with Equation 4.5 for the $\theta_0 = 45^\circ$ case. The mean deviation is 0.19% with a maximum deviation of 0.69%. This result provides a level of confidence to the numerical h_a calculations for other TEM feed arm angles.

C. CALCULATED RESULTS

The location of the ideal contour was computed for most of the cases in Table 3.1. The ideal contour was not found for all of the cases because for b_1 coefficients of less than 6 or 7, the resulting self-reciprocal electrode size is too wide to be practical for most applications. Also, the numerical computation method to find the ideal contour occasionally becomes unreliable at electrode angles less than 15° .

1. Aperture Height h_a

The aperture height was computed for circular aperture shapes that have been trimmed to conform to the shape of the ideal contour. For each electrode angle and size configuration, h_a was found for a range of aperture radii corresponding to the different aperture sizes relative to the circle of symmetry shown in Figure 4.1. The aperture height vs. aperture radius for a number of different electrode angles and sizes corresponding to a 200 Ω input impedance is shown in Figure 4.6. The 200 Ω case is used in this discussion because that is the input impedance most commonly used in high power applications.

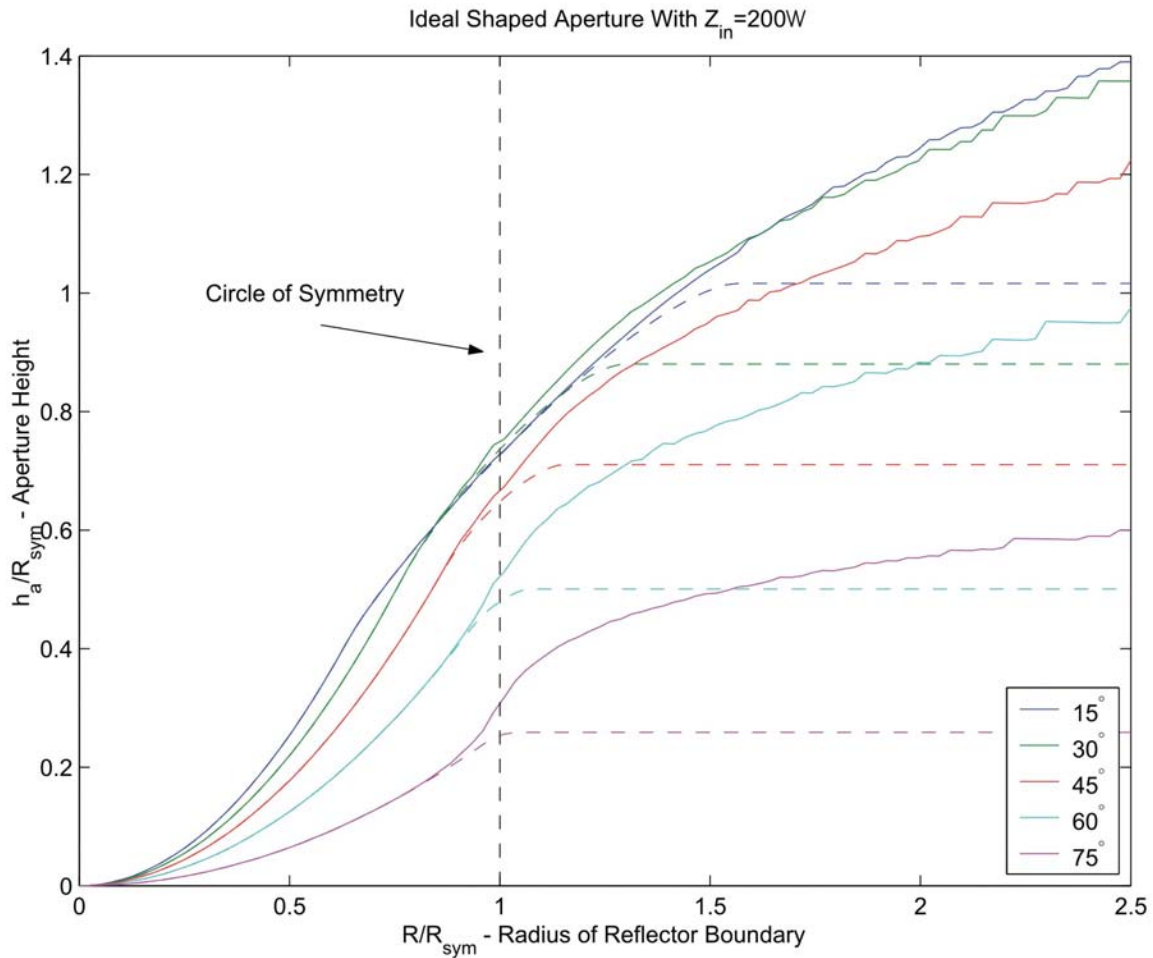


Figure 4.6. Plot of aperture height vs. the radius of the reflector boundary. Five different electrode angles with electrode sizes corresponding to a TEM input impedance of 200 Ω . The dashed lines represent a circular aperture that does not follow the ideal contour.

Notice in Figure 4.6 that h_a increases as the size of the ideal aperture increases. This is due to the fact that the larger aperture is focusing more constructively contributing input electric field, resulting in a larger magnitude radiated field. Also it can be seen that there is a maximum curve for h_a somewhere between 15° and 30° . The inflection point to the left of the circle of symmetry corresponds to the beginning of the electrode. The roughness of the curves at larger radii is due to the coarseness of the finite element mesh used to compute the ideal contour.

The dashed lines in Figure 4.6 are due to standard circular apertures that do not follow the ideal contour. The standard circular aperture encompasses both constructively and destructively contributing input electric fields. Notice that the standard aperture closely follows the ideal aperture and then at a point larger than the circle of symmetry, the standard aperture levels off while the ideal aperture continues to increase. This is reasonable at radii smaller than the circle of symmetry because the area of “bad” electric field being eliminated by the ideal aperture is relatively small. Refer to Figure 3.15 to help visualize this. As the size of the aperture is increased at radii greater than the circle of symmetry the amount of “bad” electric field being eliminated by the ideal aperture becomes more and more significant. The leveling off of the standard case occurs at the outer tip of the electrode and is also reasonable because at large radii, the ideal contour essentially splits the increased aperture area between “good” and “bad” electric field into two equal halves.

2. Normalized Values for Aperture Height

From Figure 4.6 it appears that h_a will increase with a larger ideal aperture, because a larger aperture will focus a larger portion of the input field. Typically the size of the aperture is specified by physical constraints, such as there may only be one square meter available for an antenna. The position of the circle of symmetry is determined by the size of the TEM electrodes. The larger the electrodes, the larger the radius of the circle of symmetry will be. Therefore by changing the size of the circle of symmetry compared to the size of the aperture will change how much of the total aperture area will contribute constructively to the radiated electric field. The question is whether for a given aperture size, and impedance, can the radiated electric field be made larger by making the input TEM electrodes smaller?

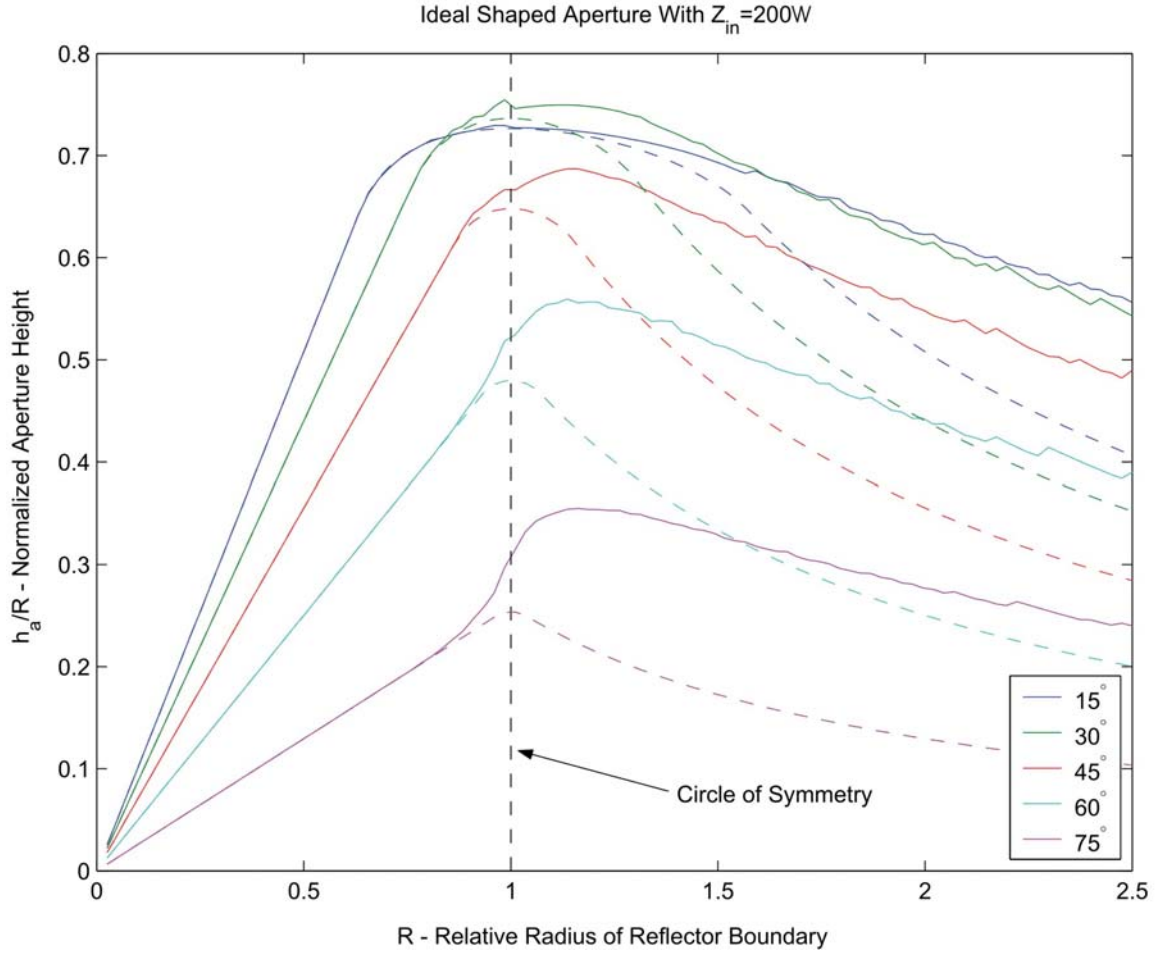


Figure 4.7. Aperture height normalized by the size of the focusing aperture. The dashed lines represent a standard circular aperture. This figure can be used in IRA design. Suppose a 200Ω antenna with 60° electrodes is being made, looking at the graph, the peak value for h_a occurs at a radius of 1.14 times the circle of symmetry boundary. So if the aperture radius is 1 meter then the circle of symmetry radius will be $1/1.14$ or 0.877 meters.

This question can be answered by looking at Figure 4.7 which is a normalized version of Figure 4.6. The y-axis is h_a normalized by the radius of the aperture, and the x-axis is the radius of the aperture normalized by the radius of the circle of symmetry. Therefore a relative radius value of one corresponds to an aperture with the same radius as the circle of symmetry. The main difference between the two figures, is that in Figure 4.6 the aperture is physically getting bigger along the x-axis. In Figure 4.7, the overall size of the aperture remains the same, but it becomes larger relative to the circle of

symmetry along the x-axis. In other words, the circle of symmetry is being made physically smaller.

The maximum h_a in Figure 4.7 is at an electrode angle of 30° at a radius of $R=1.125$ relative to the circle of symmetry. The knee in the curves to the left of the circle of symmetry occurs at the inner edge of the feed electrode. The knee is less obvious at lower angles because less of the aperture has fields oriented in the wrong direction. Since this is a normalized plot, it is important to note that increase in h_a is not caused by increasing the actual size of the aperture. Two factors cause this increase. First, the edge of the aperture is following the ideal contour instead of the circle of symmetry. Second, by making the electrodes smaller relative to the circle of symmetry, the circle of symmetry is being made smaller relative to the edge of the aperture.

Thus for a given aperture size with smaller electrodes, the aperture encompasses the portions of the input electric field that have the greatest positive effect on the prompt radiated electric far field.

3. Trends

Table 4.1 contains data for four different input impedances that are most likely to be used in high power applications: 100, 150, 200 and 250 Ω . The second column contains the electrode measured in the plane of the aperture. It is equal to $b_2 - b_1$ from Equations 3.4 and 3.5. The third column contains the angle of the electrode measured clockwise from the y-axis. The h_a for a circular aperture with a radius equal to the circle of symmetry that does not follow the ideal contour is given in the 4th column and is titled $h_a \text{ COS}$. The maximum normalized h_a for a circular aperture that follows the ideal contour is listed in the fifth column along with the relative radius that this occurs in the 7th. Finally the percent increase in aperture height obtained by following the ideal contour at the optimum relative radius verses a plain circular aperture at the circle of symmetry is given in the 6th column.

Input Z ohms	Electrode length	Angle theta	ha COS	ha ideal	% incr	Relative Radius
100	2.860	30	0.443	0.453	2.11%	0.97
100	1.796	45	0.439	0.457	3.99%	1.58
100	1.029	60	0.372	0.433	16.48%	1.62
100	0.435	75	0.226	0.326	44.03%	1.34
150	1.796	15	0.584	0.589	0.84%	0.89
150	1.156	30	0.616	0.623	1.19%	1.13
150	0.704	45	0.571	0.610	6.83%	1.31
150	0.435	60	0.437	0.521	19.21%	1.26
150	0.202	75	0.243	0.347	43.07%	1.24
200	0.916	15	0.726	0.730	0.42%	0.96
200	0.521	30	0.736	0.750	1.80%	1.11
200	0.275	45	0.648	0.687	6.00%	1.16
200	0.130	60	0.480	0.559	16.63%	1.14
200	0.061	75	0.254	0.355	39.94%	1.16
250	0.435	15	0.841	0.845	0.53%	0.96
250	0.202	30	0.812	0.828	1.89%	1.09
250	0.130	45	0.678	0.719	5.97%	1.09

Table 4.1. Increase in aperture height due to an ideal contour shaped aperture.

a. Electrode Size

The first noticeable trend is that the electrode size gets smaller as input impedance grows. Also for a given input impedance the electrode size decreases as the angle of the electrode increases.

b. Maximum Normalized h_a

The maximum normalized aperture height typically occurs at a relative radius greater than the circle of symmetry. As the electrode angle decreases, the relative radius that the maximum h_a occurs asymptotically approaches the circle of symmetry. This is evident in Figure 4.8. Notice at low electrode angles, there appears to be some numerical noise in the curves just to the right of the circle of symmetry. This is due to the relatively large size of the triangles in this region of the finite element mesh used to compute the location of the ideal contour. In Table 4.1, at low electrode angles, the relative radius where the maximum h_a occurs is less than the circle of symmetry, but when looking at the plots in Figure 4.8 it is evident that these values are within the error caused by the numerical noise and that the maximum h_a is at the circle of symmetry.

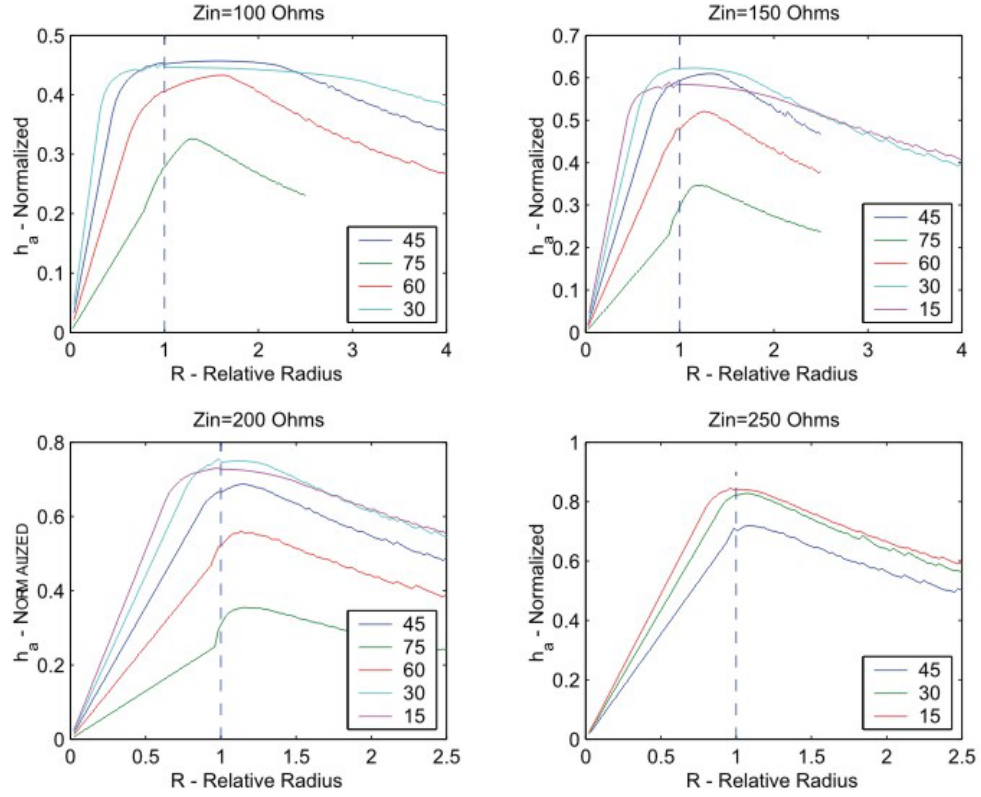


Figure 4.8. Normalized aperture height curves for different input impedances.

c. *Optimum Electrode Angle*

Initially as the electrode angle increases, the aperture height h_a also increases. The maximum normalized aperture height reaches a maximum value and then decreases as the electrode angle continues to increase. Figure 4.9 shows that the maximum occurs at an angle of approximately 23° for the 200Ω case. Typically the optimum electrode angle for a circular aperture is between 20 - 25° [Tyo, 1999].

d. *Increase in h_a Due to Following Ideal Contour*

For given input impedance, the percent increase in h_a is larger at higher electrode angles. This is because at higher electrode angles, a larger portion of the aperture that has E_y orientated in the wrong direction is removed. This is easily seen in Figure 4.10.

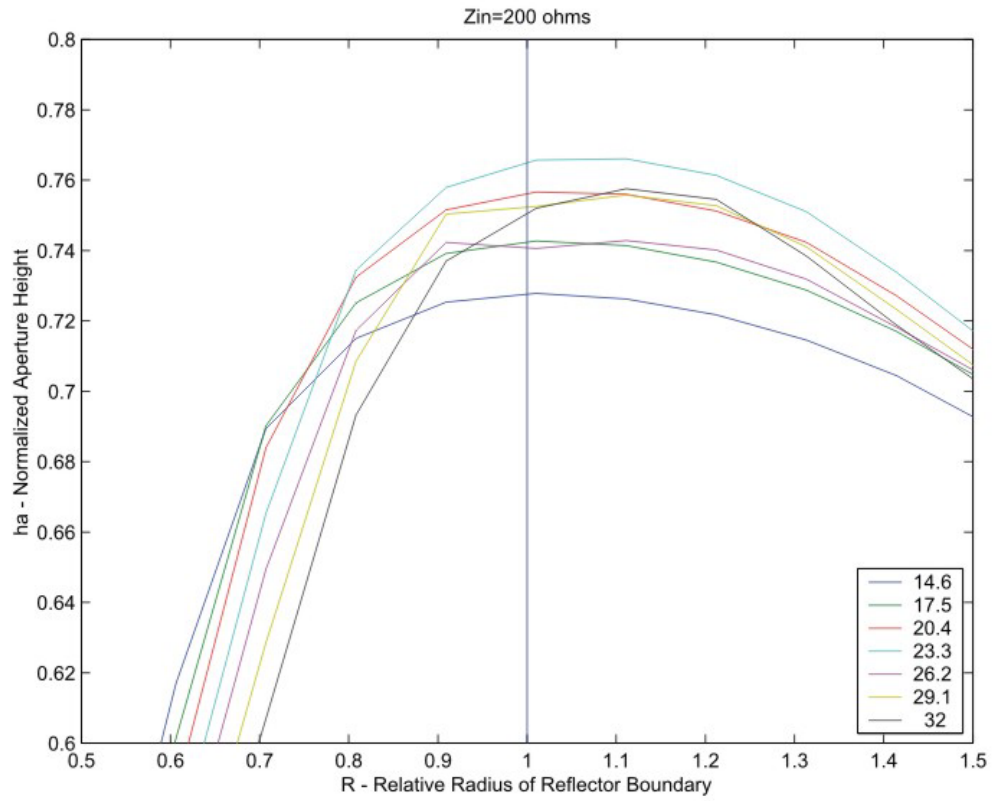


Figure 4.9. Maximum normalized h_a increases as the electrode angle increases and reaches a maximum at 23° . As the electrode angle continues to increase, the value for h_a begins to decrease.

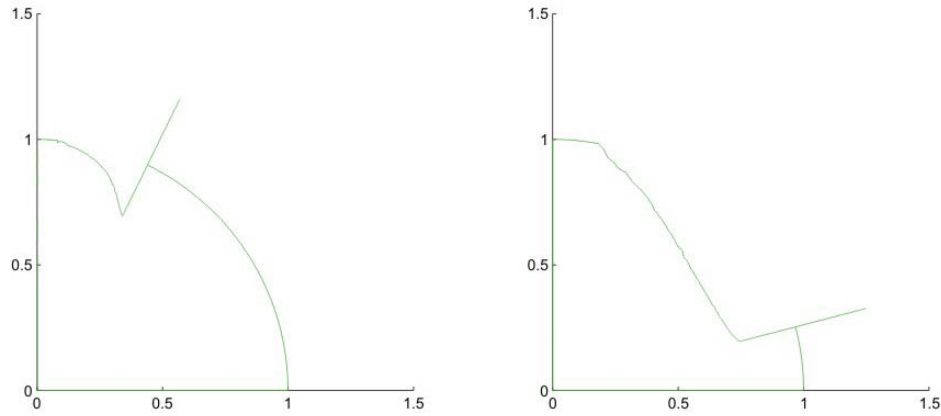


Figure 4.10. For large electrode angles, a larger portion of the aperture has the electric field orientated in the wrong direction. When this area is removed, there is a greater effect on the radiated electrode field than at small electrode angles.

D. APERTURE TRIMMING IN ANTENNA DESIGN EXAMPLE

As an example consider a parachute that will be delivered over a target via an artillery shell and once deployed transmit as much of electromagnetic energy as possible to the target. The canopy of the parachute will serve as a parabolic reflector and the electrodes will be suspended from the canopy. Figure 4.11 is a basic drawing of the parachute IRA. [Farr, 2001a]

Mechanical considerations require that the electrodes extend no farther than the edge of the parachute canopy. The proper portions of the canopy need to be metalized in order to maximize the radiated electric field. Figure 4.12 is a two dimensional view of the parachute IRA from an observer standing underneath it along the bore sight of the antenna.

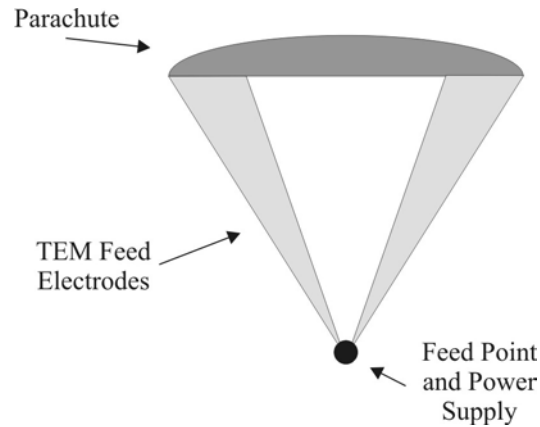


Figure 4.11. Side view of the parachute IRA after being deployed. The canopy of the parachute will be metalized to serve as the reflector of the IRA.

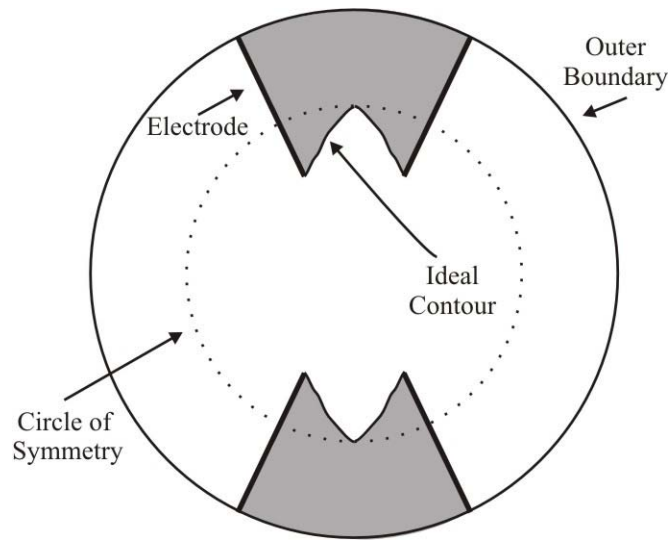


Figure 4.12. Two-dimensional view of the parachute IRA along its bore sight. The conical feed electrodes are shown at an angle of 30° after stereographic projection. The shaded portions identify the portions of the aperture that has the input electric field orientated in the wrong direction, thus these areas would not be metalized in order to maximize the radiated prompt electric field.

Since the size of the canopy and the electrodes are fixed this antenna will not be operating at the optimum point identified in Figure 4.7. This is due to the fact that the size of the circle of symmetry cannot be changed because of the fixed electrode size.

However, there will be an improvement if the portions of the canopy outside the ideal contour are not metalized. Table 4.2 summarizes the percent increase in radiated prompt electric field achieved due to ideal aperture shaping.

Input Z ohms	Angle theta	Canopy Radius	ha edge	ha ideal	% incr
100	30	3.175	1.1826	1.3300	12.46
100	45	2.242	0.8241	1.0071	22.21
150	30	1.733	0.9339	1.0481	12.23
150	45	1.412	0.7282	0.8518	16.98
200	30	1.293	0.8806	0.9590	8.90
200	45	1.147	0.7104	0.7901	11.22

Table 4.2. Increase in radiated field for the parachute IRA due to an ideal shaped aperture boundary.

THIS PAGE INTENTIONALLY LEFT BLANK

V. EXPERIMENT

A. OVERVIEW

An experiment was conducted at the Air Force Research Lab ultra wideband antenna range, shown in Figure 5.1, located at Kirtland Air Force Base. The goal of the experiment was to see if the results of chapter IV could be reproduced in the laboratory. Over a three-day period, eight different TEM feed electrode configurations were built and tested. For each configuration, measurements were made with various sized circular and ideally shaped apertures. The experimental setup, procedure and results are discussed in the following pages.



Figure 5.1. AFRL ultra-wideband antenna range.

B. EXPERIMENT SETUP

A schematic diagram of the experimental setup is shown in Figure 5.2. In order to use available equipment and simplify data collection, a half-lens IRA operating in the receive mode was used. Some discussion on this choice is needed since typically in electronic warfare applications IRAs are reflector antennas operating in the transmit mode.

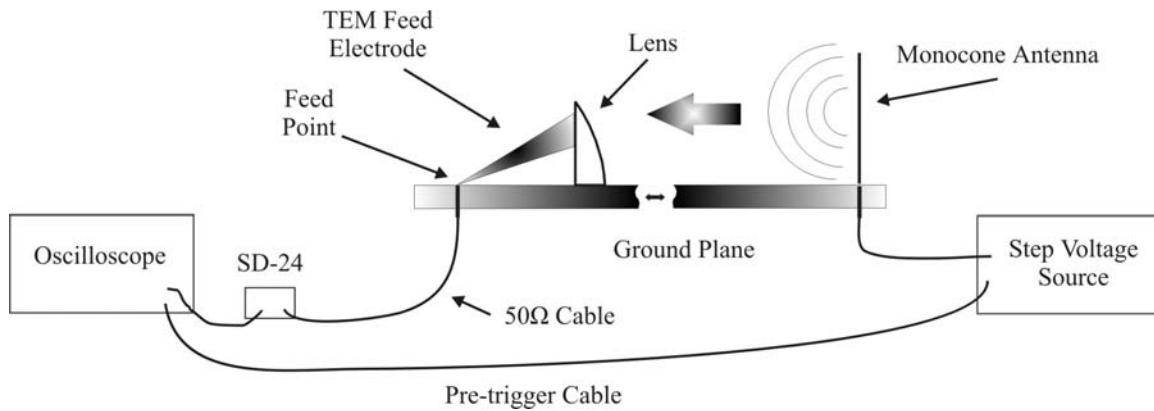


Figure 5.2. Schematic diagram of the experimental setup.

1. The IRA

The received response of an IRA is related to the transmitted response by a property called reciprocity. Reciprocity relates the transmitted and received signals of an IRA by a simple derivative. In short, the transmitted field from an IRA is the derivative of the received field under the same excitation. [Farr and Baum, 1992b]

Second, using a lens instead of a reflector sounds like a big change, but remember that the surface area integrated over to find the radiated electric field in Equation 2.17 is a post stereographic projection two-dimensional surface. As seen in Figure 5.3, the aperture has the same boundaries whether a reflector or a lens is used. Also, from Equation 2.50 the aperture height, which determines the radiated electric field, is actually computed using a contour integral along the outer edge of the focusing optic.

The method in which aperture portions are blocked to remove the input electric field orientated in the wrong direction depends on whether a lens or reflector is being used. For a reflector, the aperture would be built using an electromagnetically transparent material and only the areas that contribute constructively to the radiated electric field would be metalized. Thus the antenna would only “reflect” or transmit the electric field that is orientated in the correct direction.

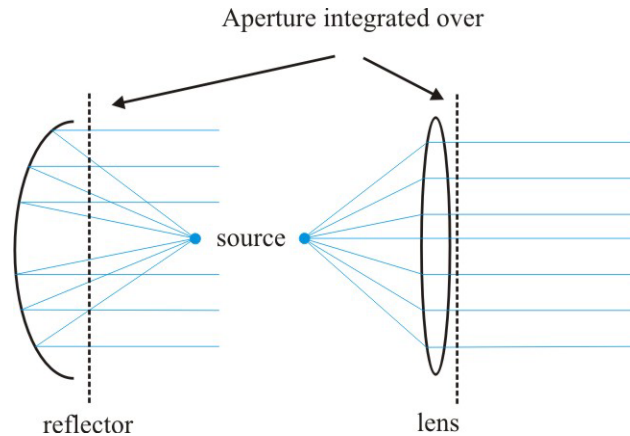


Figure 5.3. Aperture integrated over is the same for both a lens and reflector.

For a lens, the portions with the input electric field orientated in the wrong direction are covered with metal foil. Note that the “bad” portions of the lens have to be blocked and not trimmed away. Referring to Figure 5.3, notice that if a portion of the lens were trimmed away, the “bad” electromagnetic field would reach the aperture, thus interfering with the prompt response. Metal foil will effectively block the prompt response of the input signal. The foil does have an effect in the late time but for electronic warfare applications we are primarily interested in the prompt response.

The polyethylene lens, shown in Figure 5.4 is plano-convex with a 12-inch radius and a 28-inch focal length. A number of different sized feed electrodes can also be seen in Figure 5.4. In order to minimize feed blockage the electrodes were made with 1/16-inch aluminum, anything thinner would not allow the electrodes to maintain their shape. To allow the electrodes to be soldered together, copper tape was applied to the tips.

2. The range

The range consists of a 40x20 foot rectangular ground plane with a 4 ns clear time. As seen in Figure 5.5, clear time refers to the difference in time to traverse the range between a wave traveling along the center and the shortest reflected wave. The ground plane was made using $\frac{1}{8}$ -inch thick aluminum sheets resting on top of a number



(a)

(b)

(c)

Figure 5.4. (a) IRA used for measurements (b) Lens (c) Various sized electrodes.

of tables for support. A 4 ns monocone antenna, excited by a Picosecond Pulse Labs 4050B step generator, shown in Figure 5.6 transmitted spherical TEM waves across the range to the IRA operating in the receive mode. The step generator was set to transmit 47-ps rise time, 10 volt, 10-ns duration voltage steps.

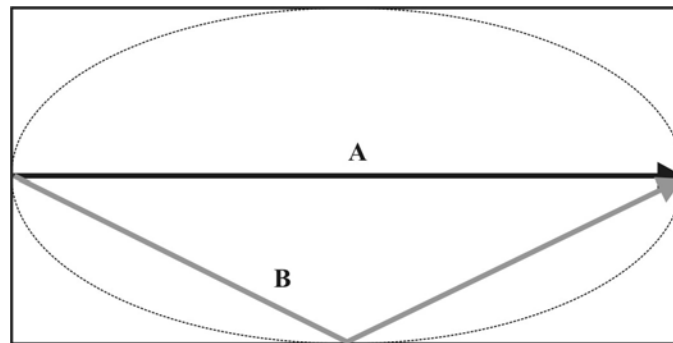
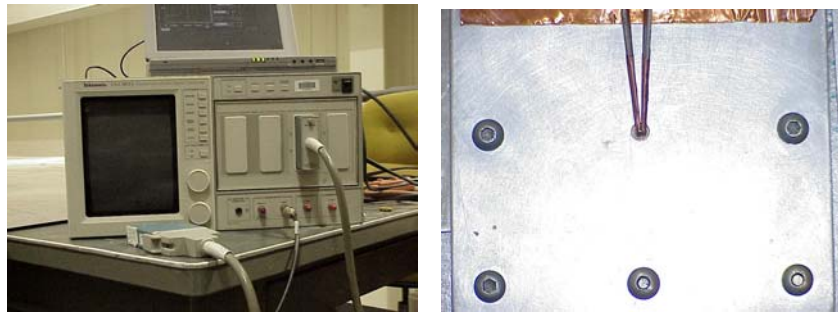


Figure 5.5. A 4ns clear time means that a wave traveling along **A** will reach the end of the range 4ns before the shortest reflected wave **B**.



Figure 5.6. Picosecond Pulse Labs 4050B step generator and the 4 ns monocone antenna



(a)

(b)

Figure 5.7. (a) Tektronix Digital Sampling Oscilloscope (b) Top view of the focal point of IRA showing the TEM electrodes connected to the co-axial cable protruding through the ground plane.

3. Data collection

Measurements were taken at the focal point of the IRA with a Tektronix CSA803A digital sampling oscilloscope shown in Figure 5.7. The copper tape tipped TEM electrodes were soldered together and connected to the center wire of a copper co-axial connector protruding through the ground plane. The signal was then fed to the SD-24 sampling head of the oscilloscope by a 50 Ω co-axial cable. In order to prepare for an incoming signal, the oscilloscope was given a sixty-five-nanosecond warning by the step generator via the pre-trigger cable, shown in Figure 5.2, between the generator and oscilloscope.

C. MEASUREMENTS

Eight different TEM feed electrode size and angle combinations were tested. For each configuration, a template of the ideal contour with a circle of symmetry radius of 8-inches was made. An 8-inch circle of symmetry was chosen so that apertures larger than the circle of symmetry could be measured with the 12-inch lens. Aluminum foil masks in the shape of the ideal contour were made with the templates. Covering the lens above the ideal contour blocked the undesired portions of the prompt response. The foil mask attached to the flat surface of the lens can be seen in Figure 5.8. To simulate different sized apertures relative to the circle of symmetry, one-inch thick metal semicircles shown in Figure 5.9 were attached to the lens.

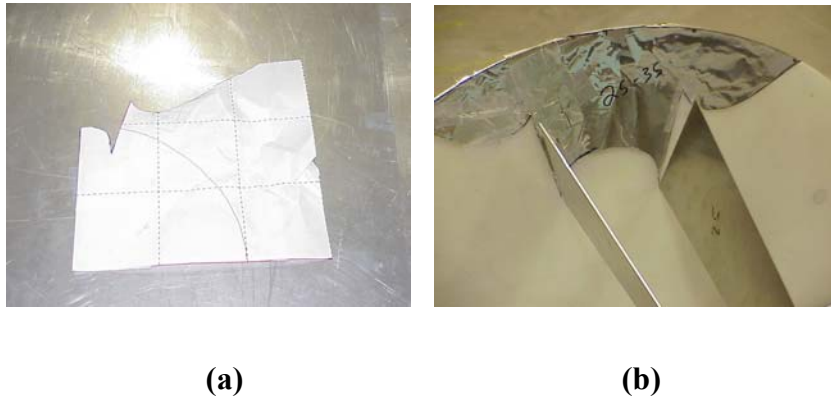


Figure 5.8. (a) Template that was used to cut the metal foil used to block the areas of the aperture above the ideal contour. (b) Metal foil template attached to the flat surface of the lens.

1. Measuring Input Impedance

The first measurement taken for each electrode configuration was the input impedance. A result close to the theoretical value gives an indication of how well the electrodes were built.

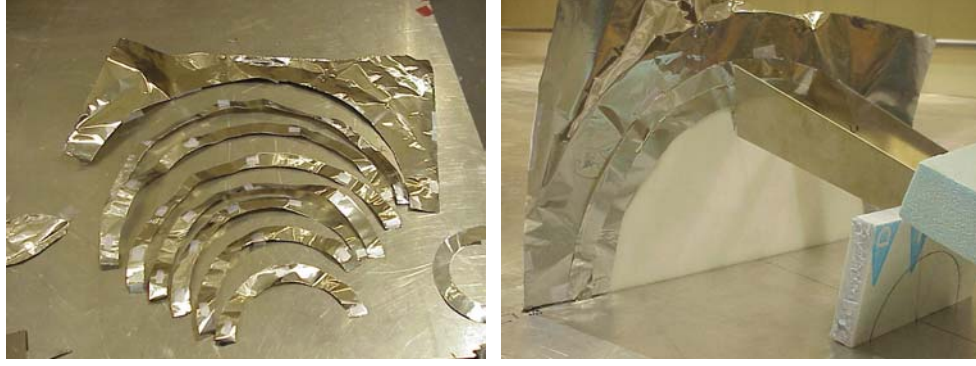


Figure 5.9. One-inch metal foil strips were used to simulate different sized apertures by blocking the prompt response of the IRA.

The input impedance was measured by setting the oscilloscope SD-24 probe in the time domain response (TDR) mode. In the TDR mode, the oscilloscope sends a voltage step to the feed of the antenna and the plot in Figure 5.10 is produced. The y-axis is the unitless reflection coefficient ρ and time is on the x-axis. Each jump in the curve represents an impedance mismatch boundary. The first flat region is the cable connecting the SD-24 to the feed point. This cable has a known impedance of 50Ω . The line corresponding to the cable should be at a value of $\rho = \text{zero}$; however the SD-24 had an offset error that could not be calibrated out. Because of this offset, measuring the difference in ρ between the electrodes and cable and inputting this value into the following equations was used to find the impedance of the TEM electrodes:

$$\begin{aligned}\rho &= \frac{Z_{\text{electrode}} - Z_{\text{cable}}}{Z_{\text{electrode}} + Z_{\text{cable}}}, \\ Z_{\text{electrode}} (\rho - 1) &= Z_{\text{cable}} (1 + \rho), \\ Z_{\text{electrode}} &= Z_{\text{cable}} \frac{1 + \rho}{1 - \rho}.\end{aligned}\tag{5.1}$$

The theoretical input impedance is twice the value for $Z_{\text{electrode}}$ because the theoretical antenna has a full circle aperture and 2 TEM feeds, while the experimental IRA is only a $\frac{1}{2}$ circle aperture resting on a ground plane.

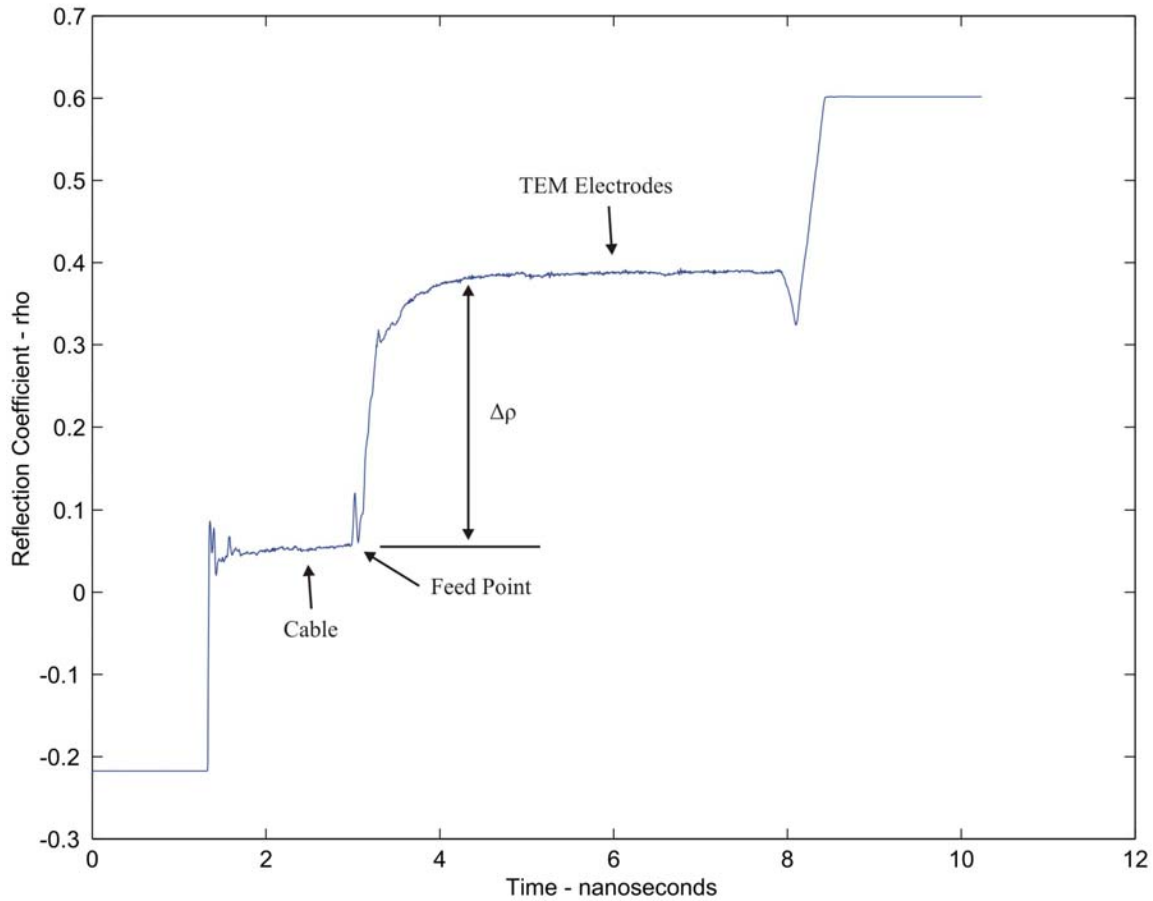


Figure 5.10. Plot of TDR response used to find impedance

2. Measuring the Aperture Height

Once the input impedance was found, the received step response of the IRA was measured. Recall that the step generator driving the monocone antenna transmitted 47ps rise time, 10 volt, 10 ns duration voltage steps. The Tektronix oscilloscope was given a 65-ns pre-trigger signal from the step generator to get ready for an incoming signal. The oscilloscope averaged 64 records for each received waveform. The samples were taken 0.25-ps apart and each record contained 2048 points. Figure 5.11 shows an entire received waveform for the 200Ω, 40° electrode case.

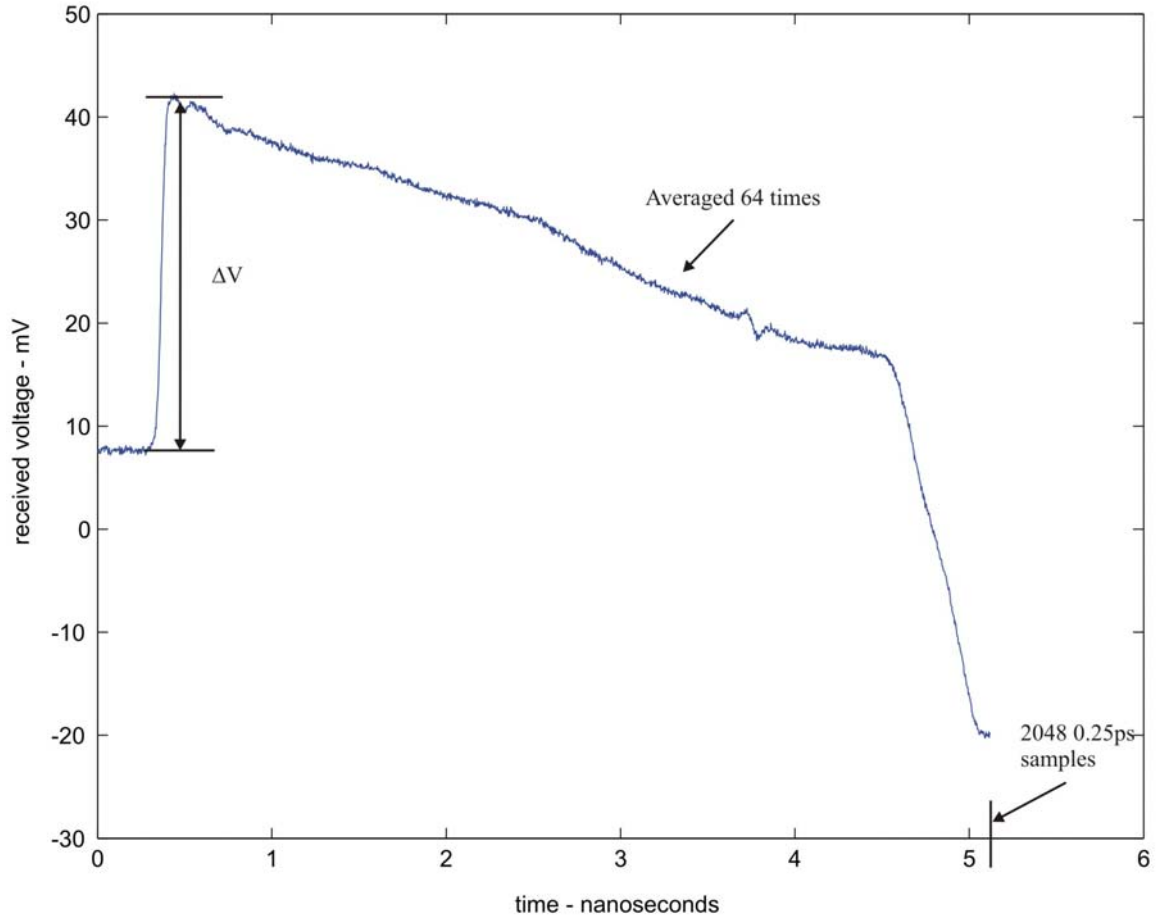


Figure 5.11. Received step response for a 200Ω, 40° electrode IRA

In order to measure the aperture height the incident electric field has to be measured. Unfortunately the equipment to measure this was not available. However as evident in Equation 2.20, the voltage of the received signal is directly proportional to h_a and can easily be measured.

The step response voltage Δv in Figure 5.10 is the difference between the peak of the step response and the flat portion of the waveform before the step response. Voltage measurements were taken for ideal shaped apertures of radii of 3, 4, 5, 6, 7, 8, 9, 10, and 12-inches. Standard circular apertures not following the ideal contour were measured at radii of 8 and 12 inches. The waveforms for the 8 and 12-inch ideal and circular cases were saved in Excel spreadsheet formats for later analysis. The measured data for each of the eight IRA configurations tested are contained in Appendix A.

D. RESULTS

1. Plotting the Results.

There is some high frequency noise apparent in Figure 5.12. To remove this noise, the data was run through an eight picosecond Gaussian filter. Also there is the voltage offset caused by a problem with the SD-24 sampling head. Figure 5.12 shows one waveform in its unfiltered, filtered and offset removed forms. The waveform “walking in and out” of the Gaussian filter causes the “tails” at the beginning and end of the filtered waveform.

Figure 5.13 shows the received voltage prompt response for the 200 Ω , 30° feed electrode angle case. Notice that the received signal is a fast rising step with a risetime of ~50-picoseconds which is consistent with the signal transmitted by the monocone antenna. As predicted, the ideal apertures have a higher magnitude step response than the circular apertures. Also, the 12-in aperture has a larger percent increase than the smaller 8-in aperture. The bottom portion of the figure shows the corresponding signal that would be transmitted due to reciprocity. The plots for all eight tested electrode configurations are contained in Appendix A.

2. Comparing Calculated and Measured Results

Figures 5.14, 5.15 and 5.16 compare the measured results with the calculated results. The solid lines represent the calculated results using the methods in Chapters III and IV. The x-marks are actual measured data. Figure 5.14 is the aperture height vs. the radius of the aperture that follows the ideal contour for the 200 Ω cases. Figure 5.15 is the normalized aperture height vs. the radius of the aperture relative to the circle of symmetry for the 200 Ω cases. Figure 5.16 contains both the normalized and un-normalized data for the 250 Ω cases. The data in these figures is discussed below.

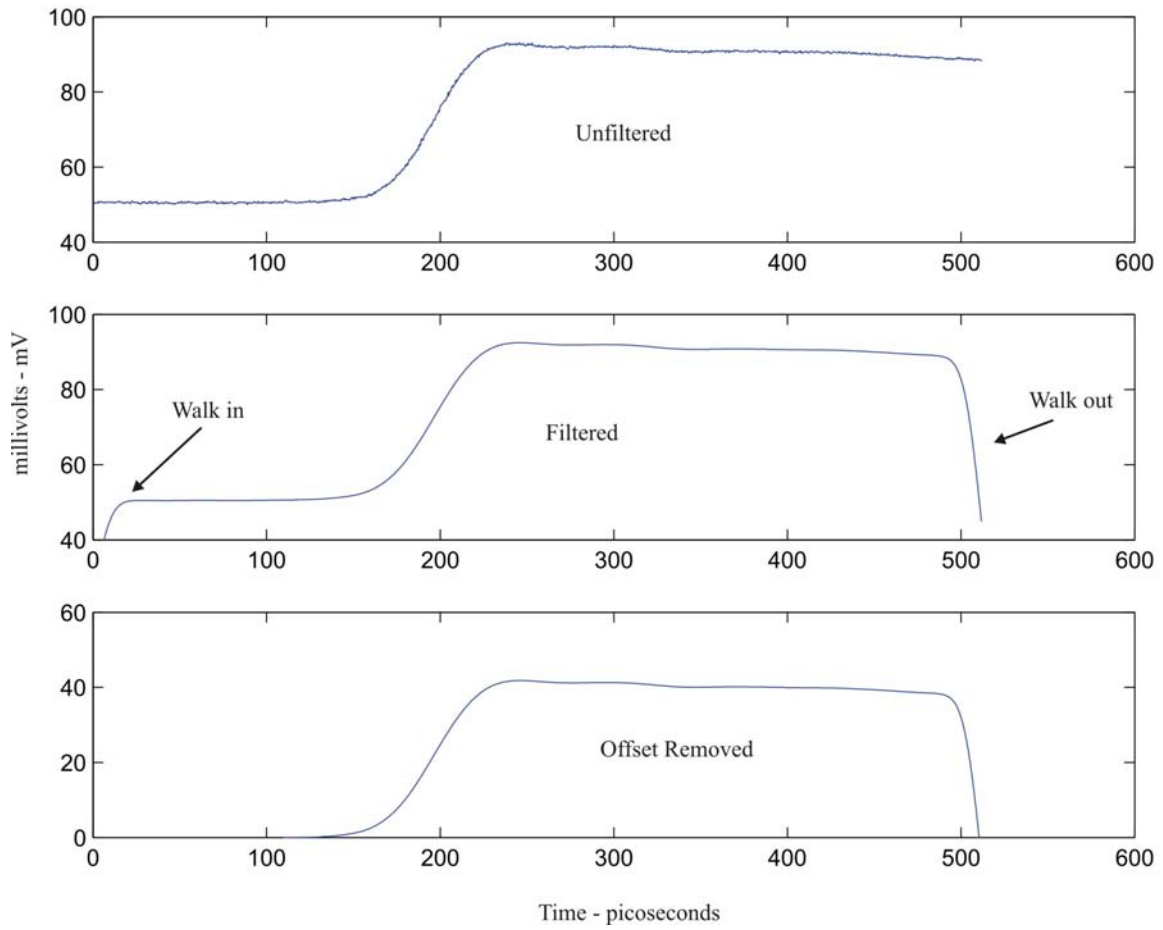


Figure 5.12. An 8ps Gaussian filter was used to remove high frequency noise from the step response

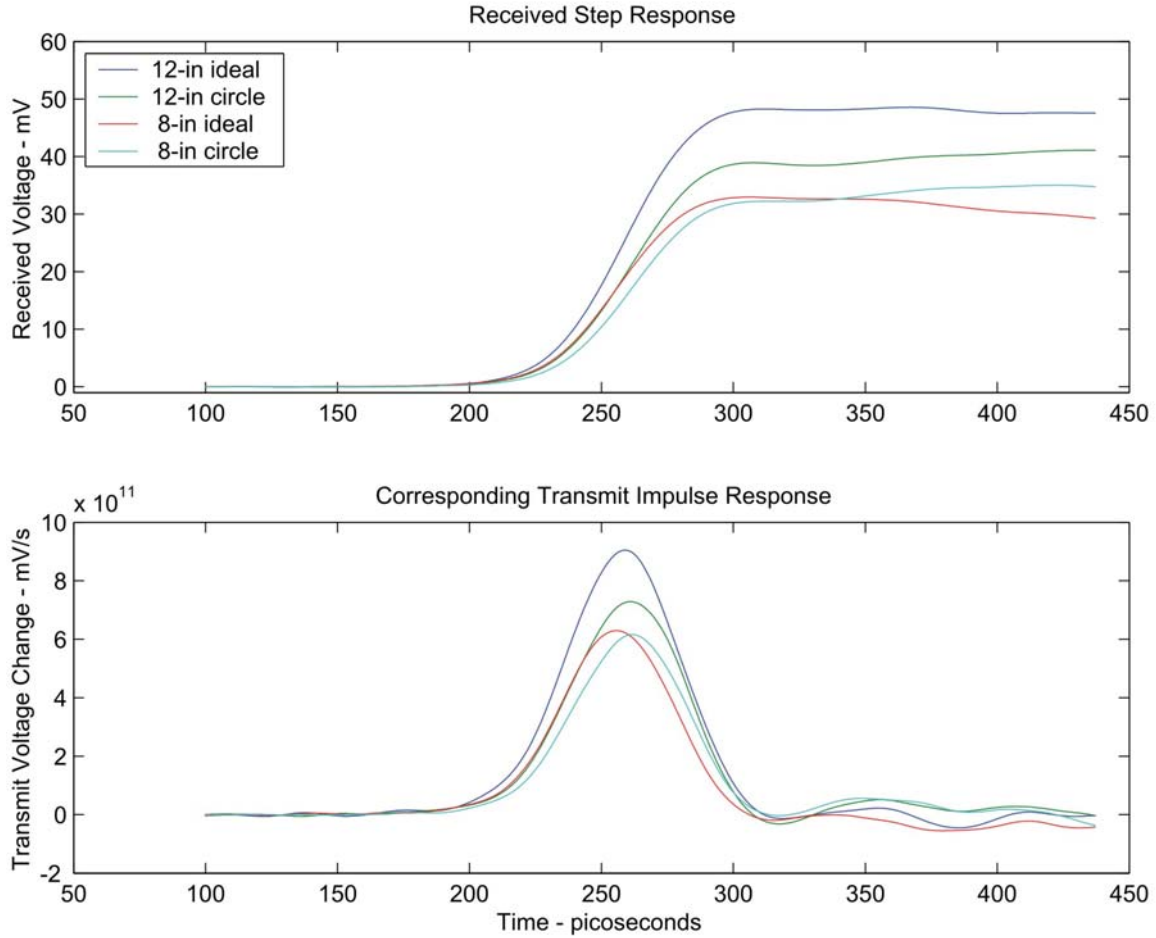


Figure 5.13. Received step response and corresponding transmit impulse response for a 200Ω , 30° electrode. Notice that the late time response becomes apparent around 320 picoseconds.

a. Comparing Aperture Height h_a to Measured Δv

In order to compare the calculated h_a to the measured Δv on the same plot, all of the data is referenced to the values obtained at the circle of symmetry. To accomplish this the calculated values for h_a were plotted vs. the radius of the aperture. Then the h_a value for an aperture with radius equal to that of the circle of symmetry is obtained from this plot. The measured Δv is then multiplied by the ratio of the calculated h_a at the circle of symmetry to the measured Δv at the circle of symmetry.

b. Match Between Experiment and Numerical Results

The un-normalized data in Figures 5.14 and 5.16 show that the experimental results closely follow the calculated in overall trend, slope and magnitude

with the possible exception of the 60° 200Ω case. However, this was the last case tested and the SD-24 sampling head for the Tektronix oscilloscope malfunctioned so an SD-26 sampling head was used in its place.

At smaller radii the measured values stray from the calculated. This is more apparent in the normalized curves of Figures 5.15 and 5.16. This was most likely caused by measurement error. Notice in Figure 5.9 that the size of the unblocked aperture relative to the size of the TEM electrodes is small, therefore the received signal is much smaller thus making the data taking more difficult. Also, the late time response caused by all of the metal foil seen in Figure 5.9, begins to obscure the prompt response. Instead of having a nice step similar to Figure 5.11 response to measure the Δv value, the response looks similar to Figure 1.3 case F.

3. Possible Sources for Experimental Error

The trends of the aperture height data do follow the calculated results, however it appears that there is some experimental error present. The lens used in the IRA setup was the only precision-machined part. The electrodes were made by hand and cut with metal cutting shears. The angles in the triangular electrodes were at best one to two degrees off of specification. The paper templates were within one tenth of an inch, however the metal masks that were made using the templates were hand made with an exacto-knife. the circular strips used to simulate different aperture sizes were also hand made. It was also difficult to cut the foam supports used to hold the electrodes at the proper angle.

During the conduct of the experiment, the metal foil semi-circular strips were attached and removed from the lens numerous times. Near the end of the three days, these strips were not as “flush-fitting” as they were in the beginning. Future experiments should use masks made of a more rigid material and also measure increments smaller than one inch.

There was one possible source of error due to equipment malfunction. The SD-24 probe had an offset from the beginning that could not be calibrated out. And on the third day, the probe stopped working entirely.

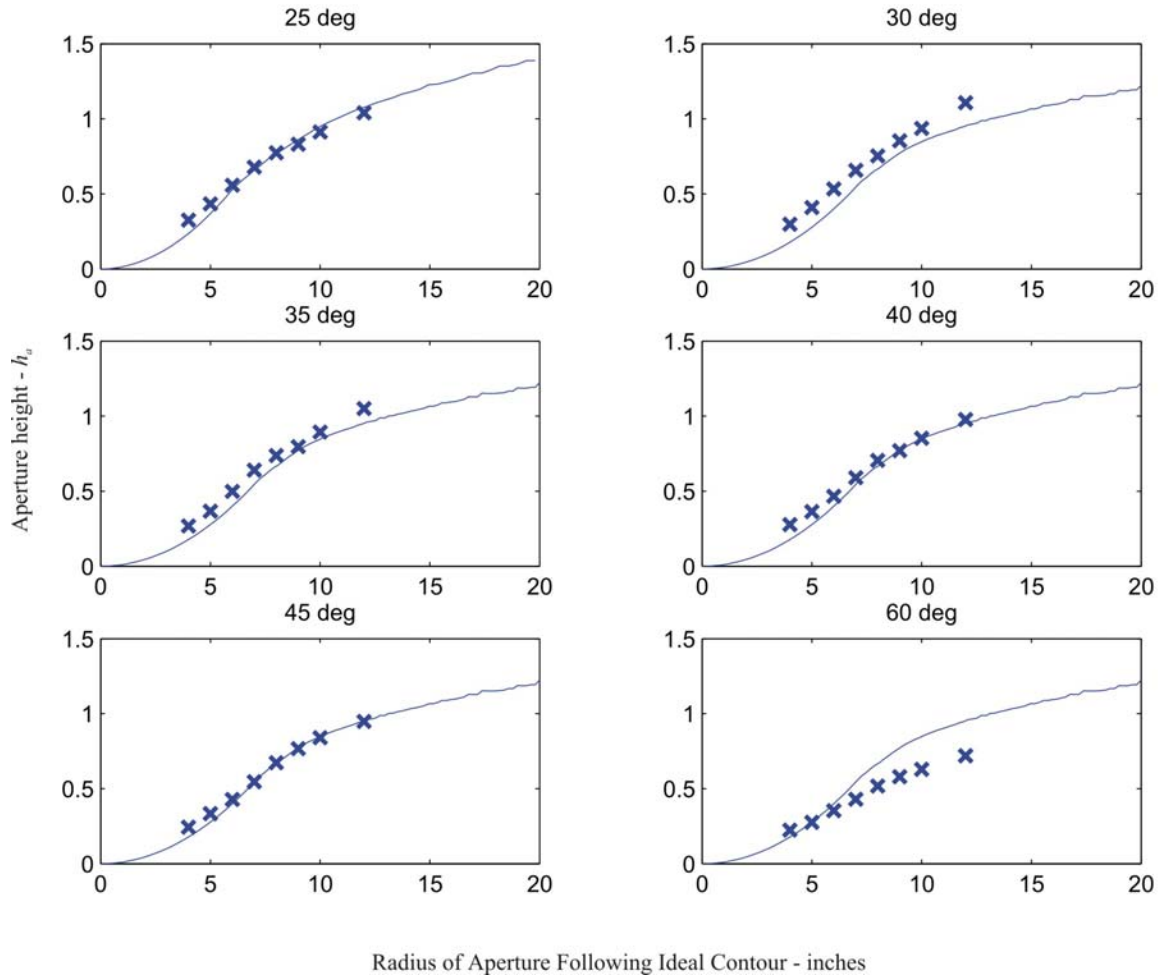


Figure 5.14. Experimental values for h_a denoted by the x's compared to calculated data for 200 Ω IRAs

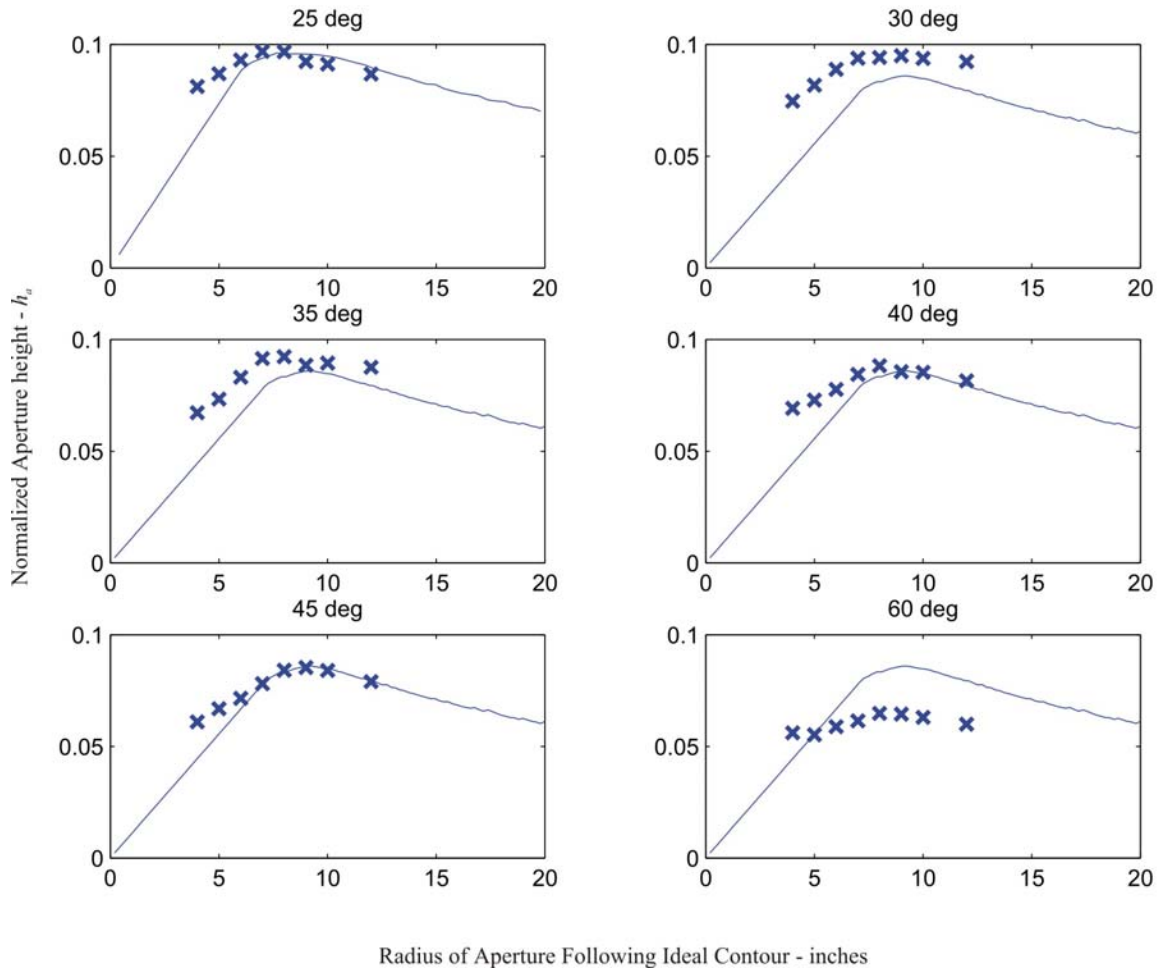


Figure 5.15. Experimental values for Normalized h_a denoted by the x's compared to calculated data for 200 Ω IRAs

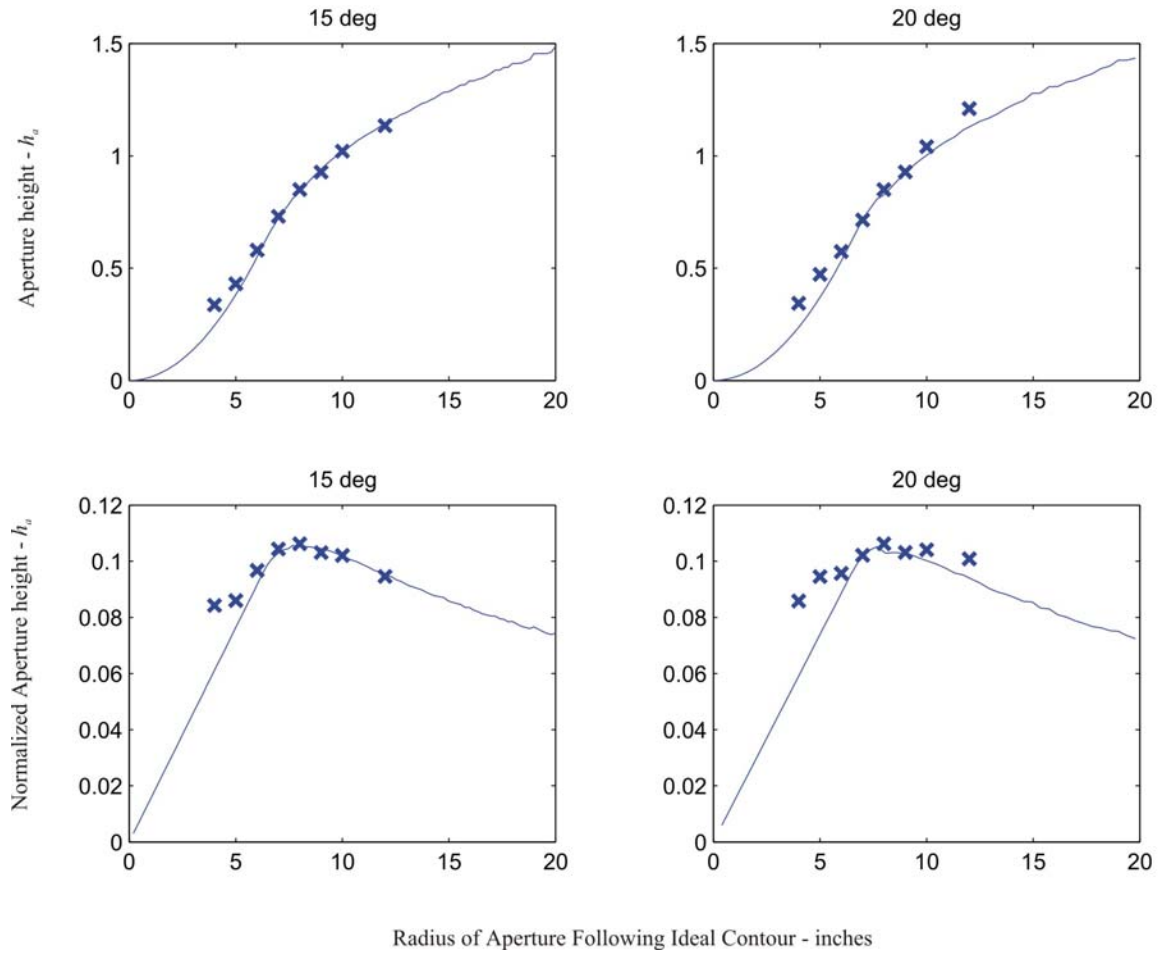


Figure 5.16. Experimental values for h_a and Normalized h_a denoted by the x's compared to calculated data for 200Ω IRAs

VI. CONCLUSION AND RECOMMENDATIONS

A. CONCLUSION

The prompt radiated electric field from an IRA can be improved by changing the shape of the aperture to eliminate the portions of the aperture that contribute negatively to the far field. In chapter II it was shown using the Field Equivalence Principle that the prompt radiated electric field in the far field is proportional to the integral of the transverse electric field on the surface of the focusing aperture. The portions of the aperture electric field that contribute negatively to the radiated electric field were then found in chapter III. The aperture boundary that encloses only positively contributing electric field is termed the ideal contour.

The ideal contour was then found for a number of different IRA configurations and the resulting change in aperture height are presented in chapter IV. The radiated electric field is proportional to the aperture height, h_a , which in turn is proportional to the integral of the transverse electric field on the surface of the aperture. Therefore, by maximizing h_a , the radiated electric field will also be maximized. It was found that apertures whose boundaries follow the ideal contour always show an improvement in the radiated electric field. As a general rule antennas with large electrode angles tended to show a more dramatic increase in radiated electric field than those with smaller angles.

The experiment conducted at the AFRL ultra wideband antenna range confirmed the calculated trends discussed in chapter IV. Normalized values of aperture height were measured since the actual magnitude was not measured due to lack of proper equipment.

Future IRA design can take advantage of the methods discussed in this thesis to optimize their prompt radiation characteristics. For an IRA with a fixed aperture size, moving the circle of symmetry relative to the maximum aperture size can optimize the radiated fields. In the parachute example discussed, the aperture size and the electrode size were both fixed thus fixing the position of the circle of symmetry. The radiated field was optimized for this case by removing the portions of the aperture with the electric field orientated in the wrong direction.

B. RECOMMENDATIONS

In this work the “aperture windows” studied were circular in shape. Some applications may have a square or rectangular aperture window. An extensive database of ideal contour data for many different TEM feed electrode configurations has been created. It should be a relatively simple task to apply different shaped aperture windows to these ideal contours.

For applications other than electronic warfare, the late time response of the far field characteristics are desired. As seen in some of the experimental results, aperture shaping does have an effect in the late time. Aperture shaping to increase the prompt response may have detrimental effects on the late time response.

The experiment conducted did show that effects of aperture trimming follow the same trends as the calculated results however only normalized data was available. Future experiments should attempt to minimize the possible sources of error mentioned in chapter V and also measure the electric field on the surface of the aperture so the actual magnitude of the aperture height can be determined.

APPENDIX A

A. FIRST TEM FEED ELECTRODE CONFIGURATION

Feed Identifier: 25_35
Electrode Angle: 15° (measured clockwise from y-axis)
 $\Delta\rho$: $0.424 \rightarrow 123.61\Omega \rightarrow 247.22\Omega$
Theoretical input impedance: 250.66Ω
Scope settings: 10 mv/div, 50 ps/div

Aperture	Δv (mV)	Averages	# points	Filename
12-in ideal	43.8	64	2048	feb28_01.xls
10-in ideal	39.4	64	2048	
9-in ideal	35.8	64	2048	
8-in ideal	32.8	64	2048	feb28_02.xls
7-in ideal	28.2	64	2048	
6-in ideal	22.4	64	2048	
5-in ideal	16.6	64	2048	
4-in ideal	13	64	2048	
3-in ideal	10	64	2048	
12-in clear	38.4	64	2048	feb28_03.xls

Comments:

- The input impedance was found using Equation 5.1
- The circle of symmetry for these antenna configurations has a radius of 8 inches.
- The 8-inch circular non-ideal aperture was not measured for this case
- The ideal contour template was attached to the lens and then measurements were taken for 12 to 3 inch radii. The circular non-ideal or “clear” 12 inch measurement was taken last.
- The magnitude of the received step response is largest for the 12 inch ideal case as expected.
- This was the only IRA configuration tested on February 28th.

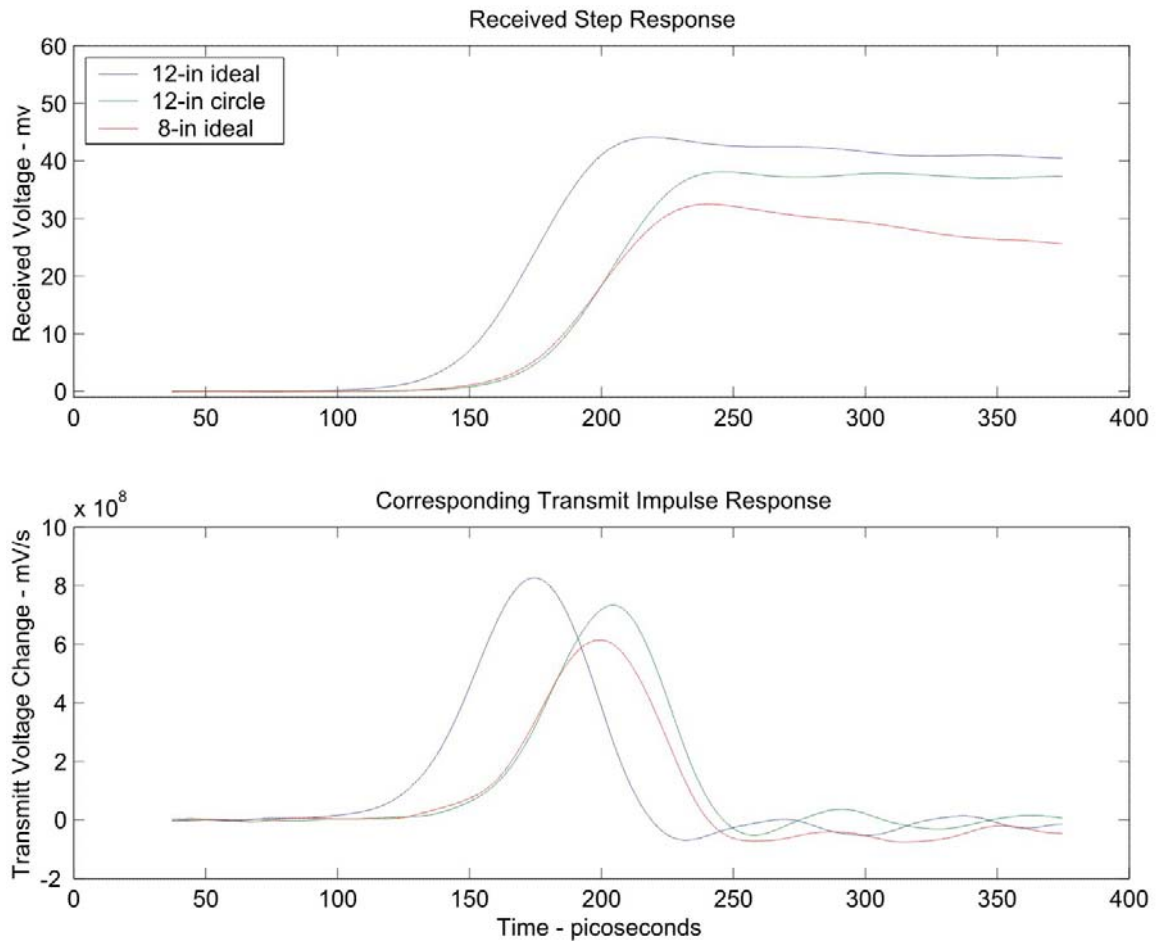


Figure A.1. Step and impulse response.

B. SECOND TEM FEED ELECTRODE CONFIGURATION

Feed Identifier: 27_31
Electrode Angle: 45° (measured clockwise from y-axis)
 $\Delta\rho$: $0.336 \rightarrow 100.62\Omega \rightarrow 200.20\Omega$
Theoretical input impedance: 203.10Ω
Scope settings: 10 mv/div, 50 ps/div

Aperture	Δv (mV)	Averages	# points	Filename
12-in ideal	42.0	64	2048	mar01_01.xls
10-in ideal	37.2	64	2048	mar01_02.xls
9-in ideal	34.0	64	2048	
8-in ideal	29.8	64	2048	mar01_03.xls
7-in ideal	24.2	64	2048	
6-in ideal	19.0	64	2048	
5-in ideal	14.8	64	2048	
4-in ideal	10.8	64	2048	
3-in ideal	9.4	64	2048	
12-in clear	31.6	64	2048	mar01_04.xls
8-in clear	29.8	64	2048	mar01_05.xls

Comments:

- mar01_01.xls is the time domain response used to find the input impedance of the antenna. This is the data used to make Figure 5.10.
- This was the first antenna configuration measured on March 1st.
- The measurements were taken in the same order as the first case with the addition of an eight inch clear aperture.
- The late time effect of the metal foil is easily visible on the eight inch clear case at about 250 ps. The waviness of the impulse response after the initial pulse is also due to the late time effects.
- The data follows the expected trends of ideal is better than clear and larger size produces larger magnitudes.

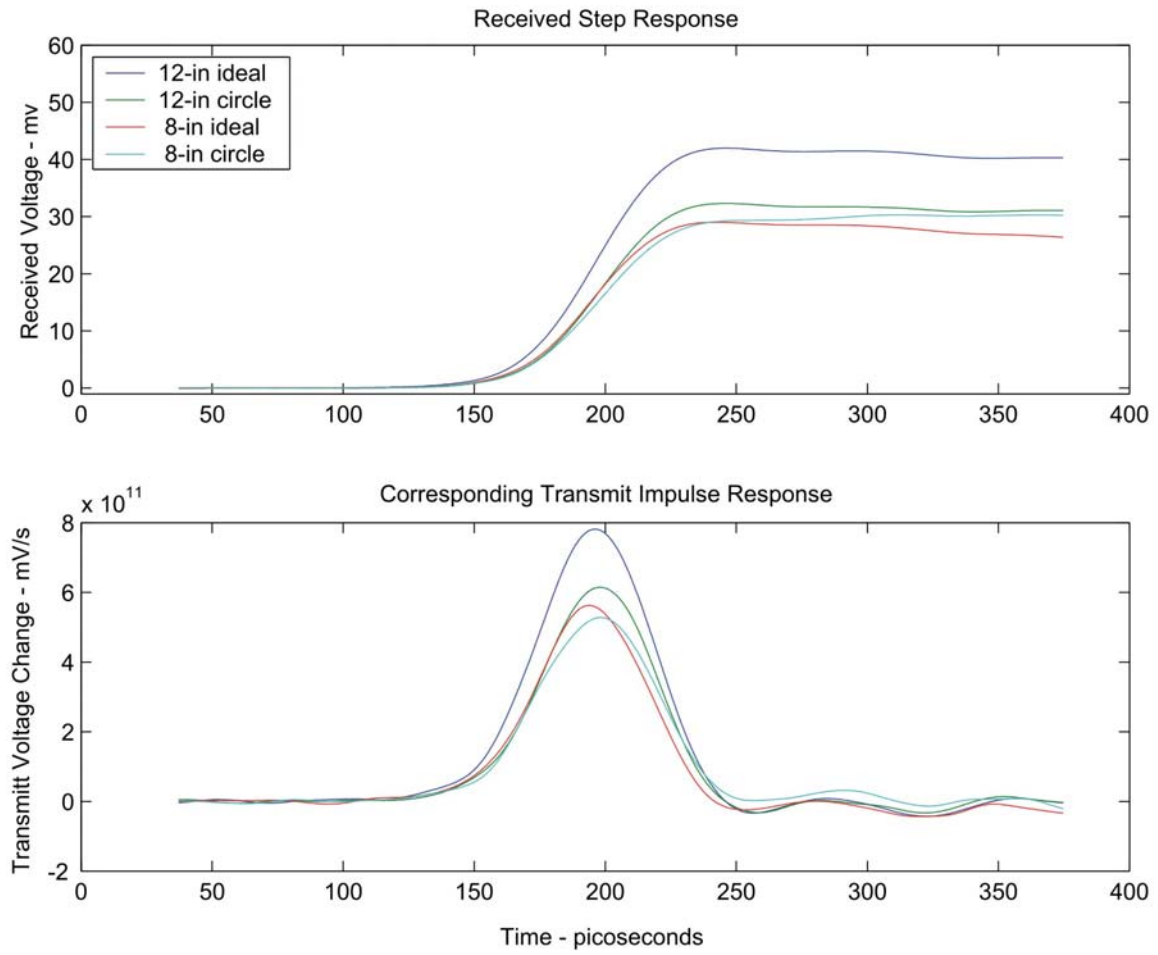


Figure A.2. Step and impulse response.

C. THIRD TEM FEED ELECTRODE CONFIGURATION

Feed Identifier: 24_34

Electrode Angle: 30° (measured clockwise from y-axis)

$\Delta\rho$: 0.320 \rightarrow 97.06 Ω \rightarrow 194.12 Ω

Theoretical input impedance: 197.44 Ω

Scope settings: 10 mv/div, 50 ps/div

Aperture	Δv (mV)	Averages	# points	Filename
12-in ideal	48.2	64	2048	mar01_06.xls
10-in ideal	40.8	64	2048	
9-in ideal	37.2	64	2048	
8-in ideal	32.8	64	2048	mar01_07.xls
7-in ideal	28.6	64	2048	
6-in ideal	23.2	64	2048	
5-in ideal	17.8	64	2048	
4-in ideal	13.0	64	2048	
3-in ideal	9.2	64	2048	
8-in clear	32.0	64	2048	mar01_08.xls
12-in clear	39.0	64	2048	mar01_09.xls

Comments:

- The 8 inch clear was measured prior to the twelve inch clear in this case.

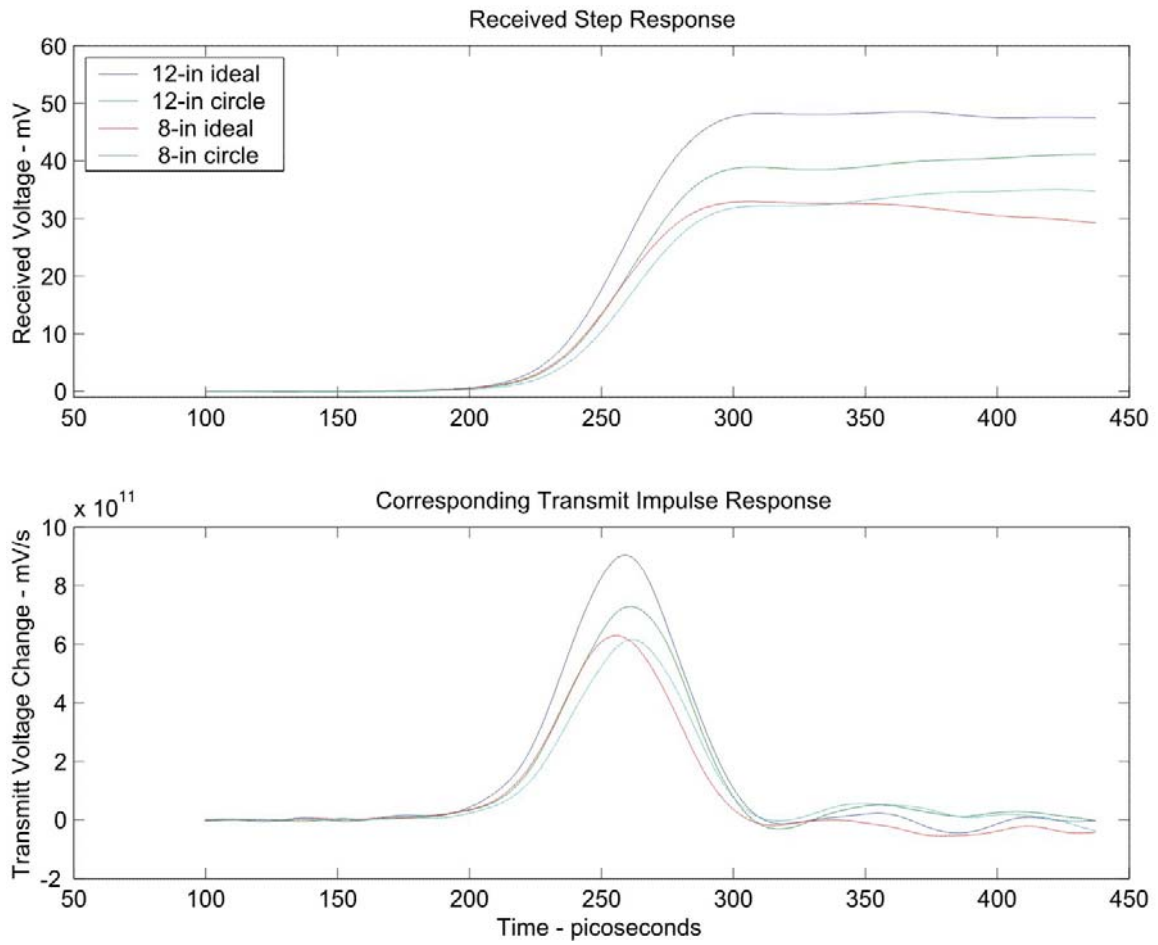


Figure A.3. Step and impulse response.

D. FOURTH TEM FEED ELECTRODE CONFIGURATION

Feed Identifier: 26_24

Electrode Angle: 20° (measured clockwise from y-axis)

$\Delta\rho$: $0.416 \rightarrow 121.23\Omega \rightarrow 242.46\Omega$

Theoretical input impedance: 246.85Ω

Scope settings: 10 mv/div, 50 ps/div

Aperture	Δv (mV)	Averages	# points	Filename
12-in ideal	43.0	64	2048	mar01_10.xls
10-in ideal	37.0	64	2048	
9-in ideal	33.0	64	2048	
8-in ideal	30.2	64	2048	mar01_11.xls
7-in ideal	25.4	64	2048	
6-in ideal	20.4	64	2048	
5-in ideal	16.8	64	2048	
4-in ideal	12.2	64	2048	
3-in ideal	9.0	64	2048	
8-in clear	31.6	64	2048	mar01_12.xls
8-in ideal	31.6	64	2048	mar01_13.xls
12-in clear	35.8	64	2048	

Comments:

- Due to the shallow angle, the ideal aperture removed only a small portion of the aperture inside the circle of symmetry. This explains the close values of the 8 inch clear and ideal cases.
- The file for the 12 inch clear step response was inadvertently erased.

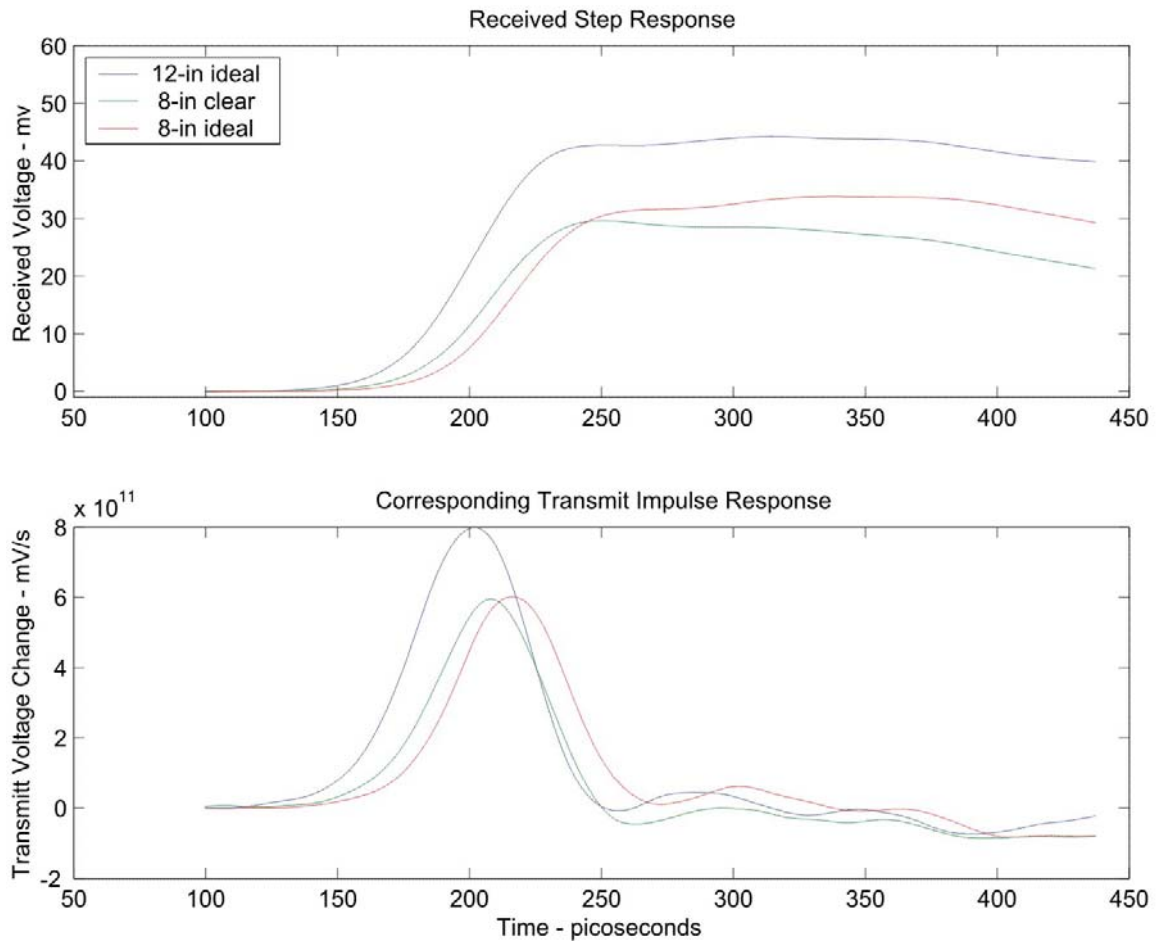


Figure A.4. Step and impulse response.

E. FIFTH TEM FEED ELECTRODE CONFIGURATION

Feed Identifier: 23_23
Electrode Angle: 25° (measured clockwise from y-axis)
 $\Delta\rho$: $0.331 \rightarrow 99.47\Omega \rightarrow 198.15\Omega$
Theoretical input impedance: 204.96Ω
Scope settings: 10 mv/div, 50 ps/div

Aperture	Δv (mV)	Averages	# points	Filename
12-in clear	40.4	64	2048	mar01_14.xls
12-in ideal	43.6	64	2048	mar01_15.xls
8-in ideal	32.4	64	2048	mar01_16.xls
7-in ideal	28.4	64	2048	
6-in ideal	23.4	64	2048	
5-in ideal	18.2	64	2048	
4-in ideal	13.6	64	2048	
3-in ideal	11.2	64	2048	
10-in ideal	38.2	64	2048	
9-in ideal	34.8	64	2048	
8-in clear	33.2	64	2048	mar01_17.xls
8-in ideal	33.0	64	2048	mar01_18.xls

Comments:

- The 12 inch clear case was measured first.
- The eight inch clear ideal case was measured twice. Again, there is not much difference between the 8 inch ideal and clear case due to the shallow electrode angle. Only one 8 inch wave form was plotted.

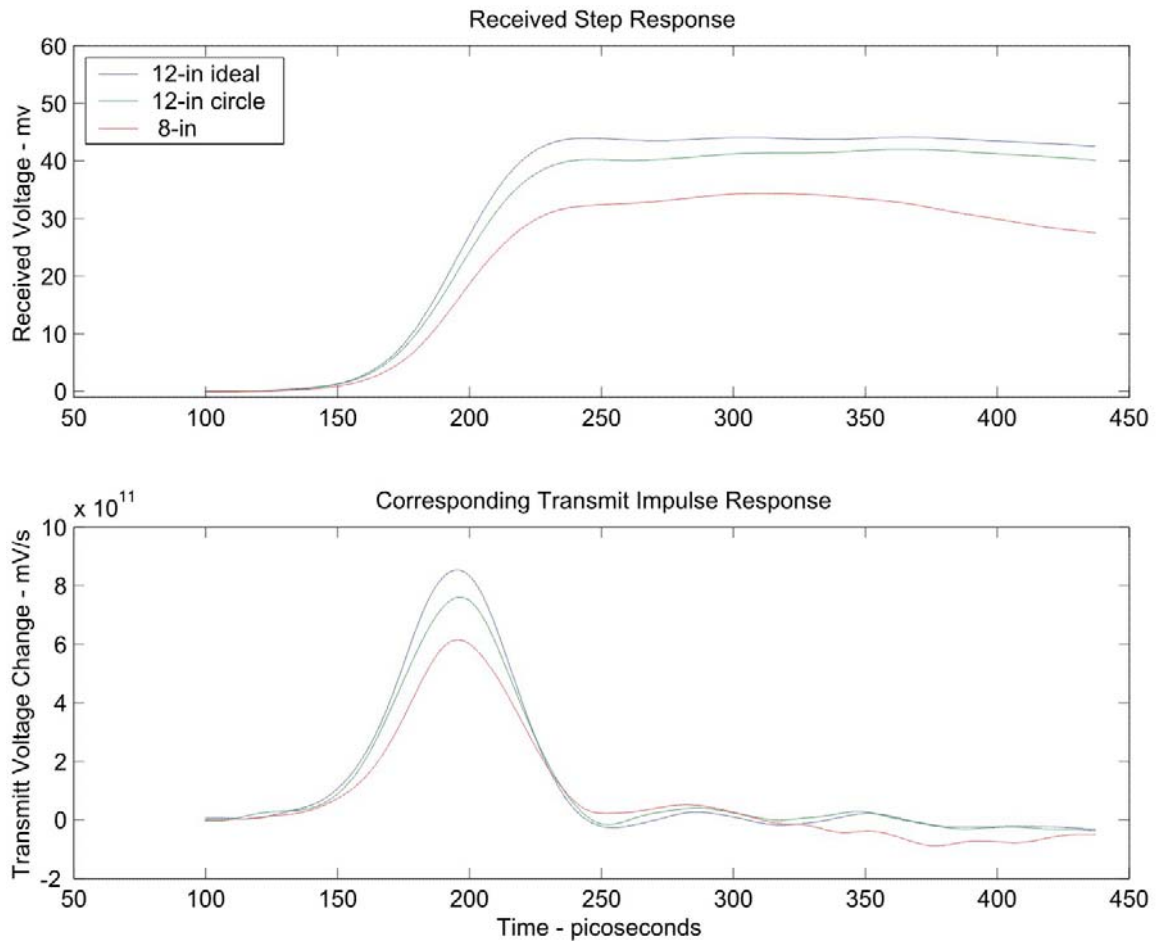


Figure A.5. Step and impulse response.

F. SIXTH TEM FEED ELECTRODE CONFIGURATION

Feed Identifier: 25_19

Electrode Angle: 35° (measured clockwise from y-axis)

$\Delta\rho$: $0.320 \rightarrow 97.06\Omega \rightarrow 194.12\Omega$

Theoretical input impedance: 192.81Ω

Scope settings: 10 mv/div, 50 ps/div

Aperture	Δv (mV)	Averages	# points	Filename
12-in clear	34.2	64	2048	mar01_19.xls
8-in clear	29.8	64	2048	mar01_20.xls
8-in ideal	30.2	64	2048	mar01_21.xls
7-in ideal	26.2	64	2048	
6-in ideal	20.4	64	2048	
5-in ideal	15.0	64	2048	
4-in ideal	11.0	64	2048	
3-in ideal	10.4	64	2048	
12-in ideal	43.0	64	2048	mar01_22.xls
10-in ideal	36.6	64	2048	
9-in ideal	32.6	64	2048	

Comments:

- The order in which the measurements were made was changed. First the clear 12 and 8 inch cases were measured. Then the ideal 8 through 3 inch cases were measured, then the 12 through 9 inch ideal cases were measured.

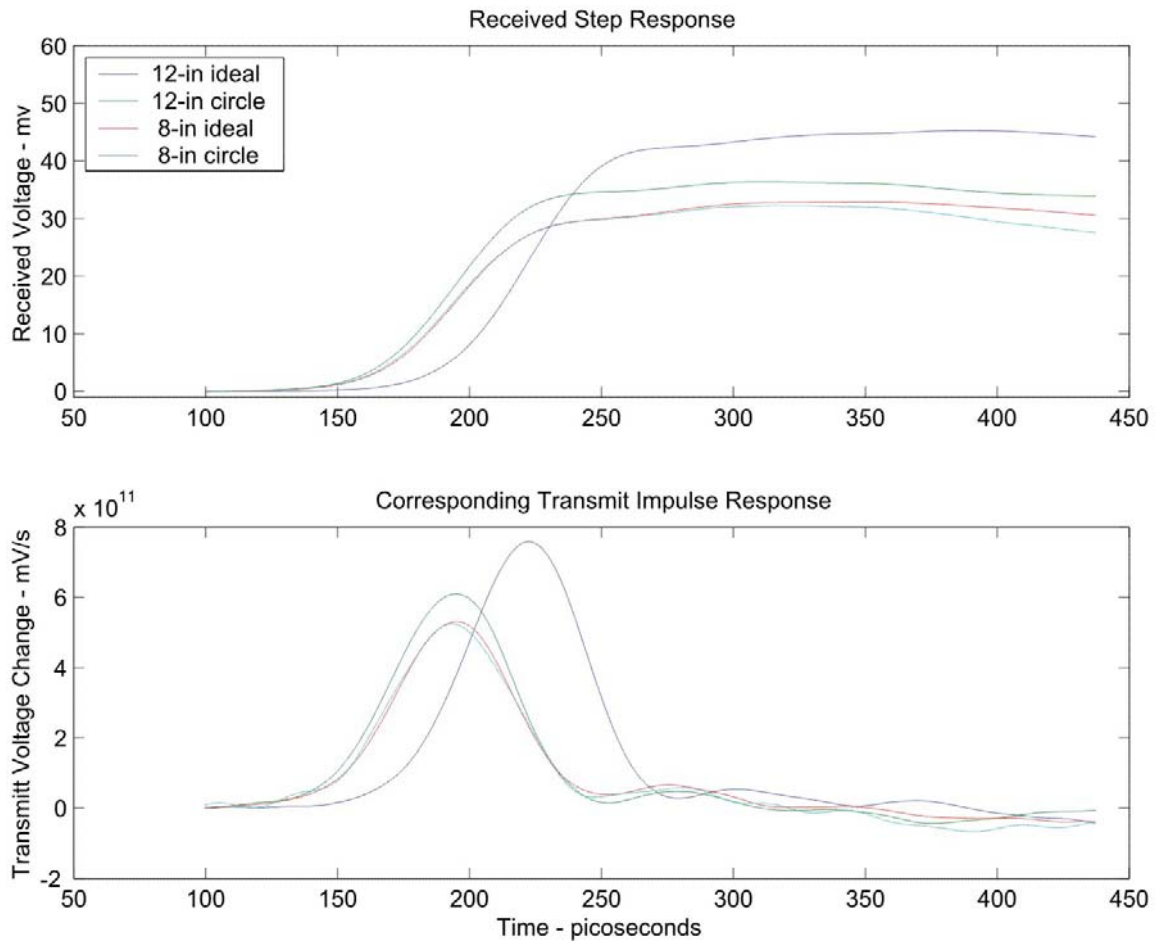


Figure A.6. Step and impulse response.

G. SEVENTH TEM FEED ELECTRODE CONFIGURIATION

Feed Identifier: 26_17
Electrode Angle: 40° (measured clockwise from y-axis)
 $\Delta\rho$: $0.326 \rightarrow 98.37\Omega \rightarrow 196.74\Omega$
Theoretical input impedance: 211.69Ω
Scope settings: 10 mv/div, 50 ps/div

Aperture	Δv (mV)	Averages	# points	Filename
12-in clear	34.0	64	2048	mar01_23.xls
8-in clear	28.6	64	2048	mar01_24.xls
8-in ideal	30.6	64	2048	mar01_25.xls
7-in ideal	25.6	64	2048	mar01_26.xls
6-in ideal	20.2	64	2048	
5-in ideal	15.8	64	2048	
4-in ideal	12.0	64	2048	
3-in ideal	9.2	64	2048	
12-in ideal	42.4	64	2048	mar01_27.xls
10-in ideal	37.0	64	2048	
9-in ideal	33.4	64	2048	

Comments:

- mar01_23.xls is the entire 10ns received step response. This data was used to make Figure 5.11.
- This was the last configuration tested on March 1st.

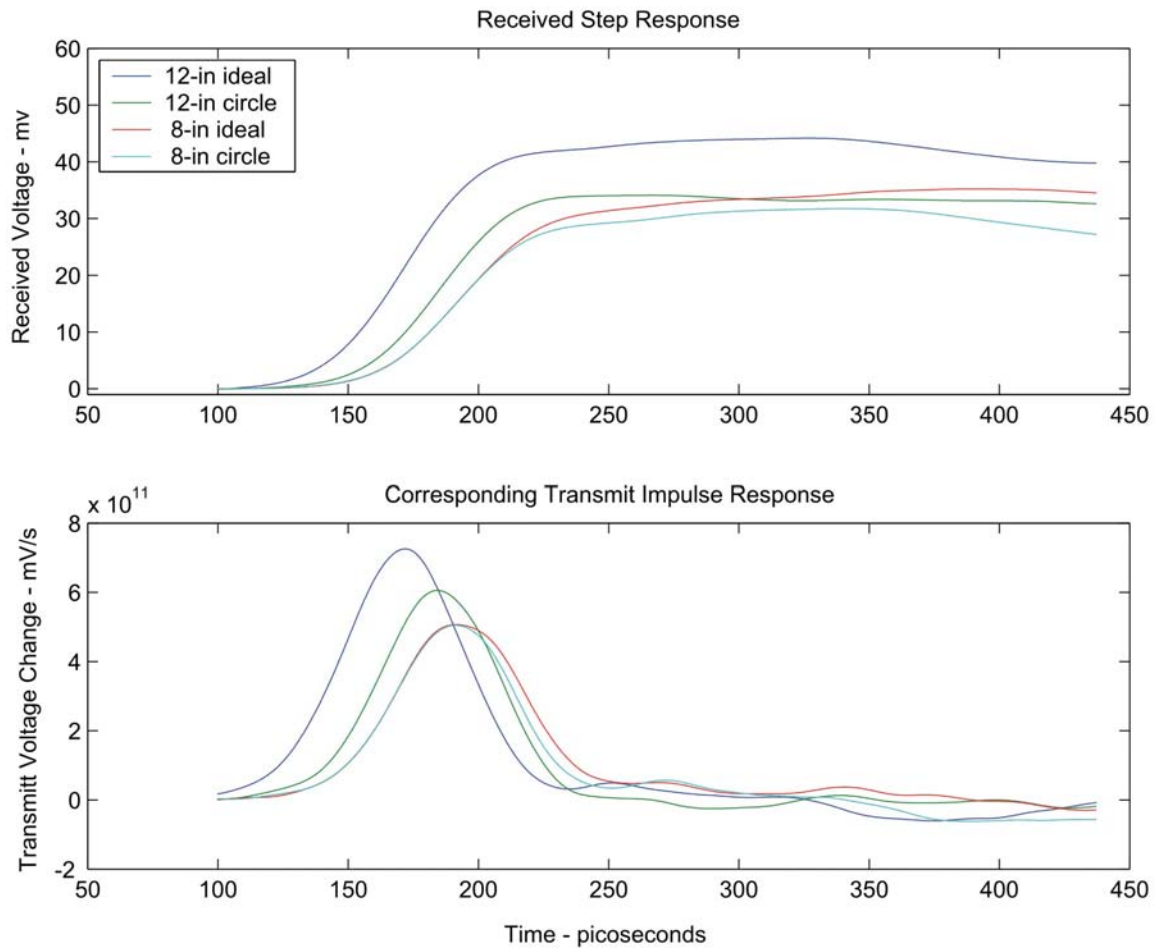


Figure A.7. Step and impulse response.

H. EIGHTH TEM FEED ELECTRODE CONFIGURATION

Feed Identifier: 28_33
Electrode Angle: 60° (measured clockwise from y-axis)
 $\Delta\rho$: Did not have SD-24 TDR
Theoretical input impedance: 190.00Ω
Scope settings: 5 mv/div, 50 ps/div

Aperture	Δv (mV)	Averages	# points	Filename
12-in clear	22.2	64	2048	mar02_01.xls
8-in clear	20.9	64	2048	mar02_02.xls
8-in ideal	22.9	64	2048	mar02_03.xls
7-in ideal	19.0	64	2048	mar02_04.xls
6-in ideal	15.6	64	2048	
5-in ideal	12.2	64	2048	
4-in ideal	9.9	64	2048	
3-in ideal	7.8	64	2048	
12-in ideal	31.8	64	2048	mar02_05.xls
10-in ideal	27.8	64	2048	
9-in ideal	25.6	64	2048	

Comments:

- The SD-24 probe malfunctioned so a SD-26 probe that does not have the time domain response mode was used as a replacement. Therefore the input impedance was not measured.
- mar02_01.xls is the entire 10 ns received step response.
- This was the only electrode configuration tested on March 2nd.

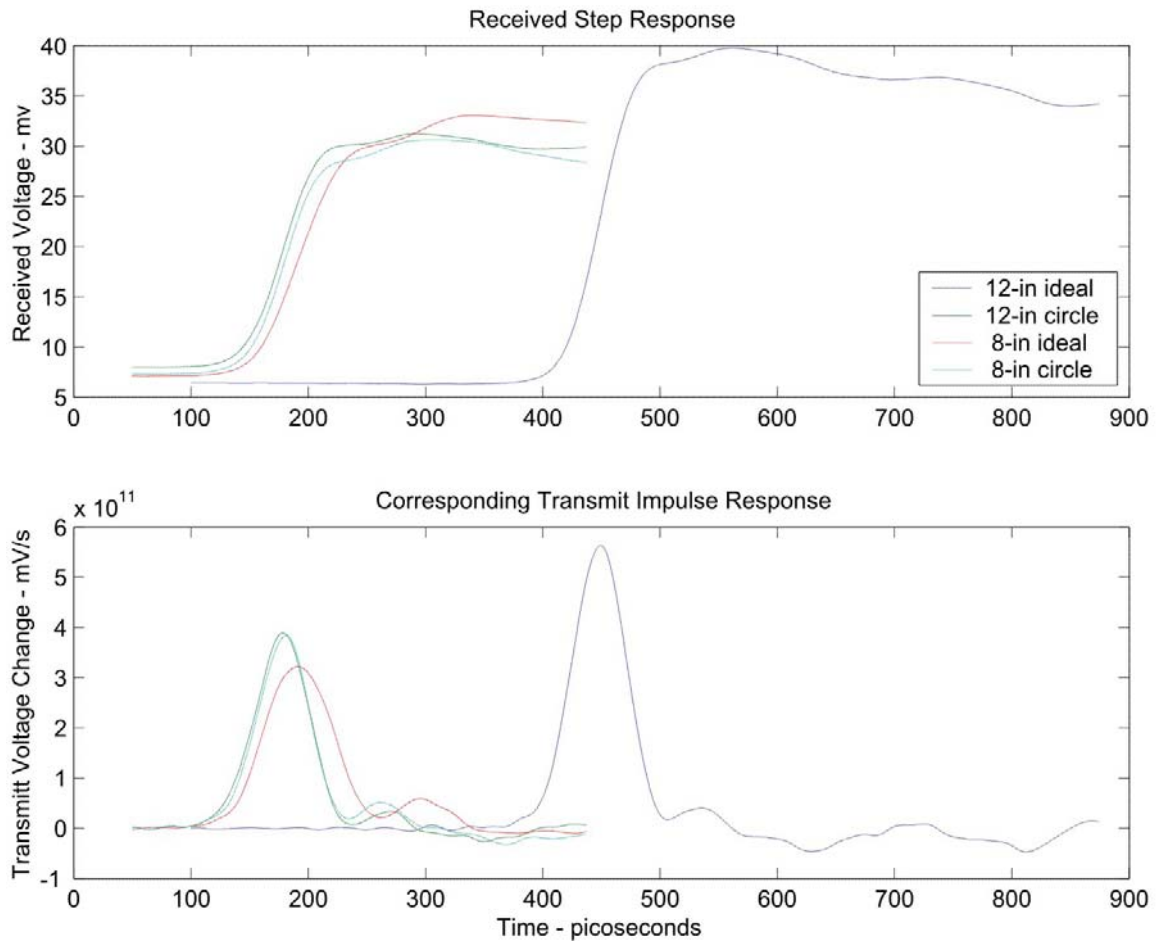


Figure A.8. Step and impulse response.

LIST OF REFERENCES

Balanis, Constantine A., *Antenna Theory Analysis and Design*, pp. 446-454, Haprer & Row, Publishers, Inc., 1982.

Baretela, Michael J. and Tyo, J. S., "Increasing Prompt Response from IRA Using Aperture Shaping," *2001 URSI Interational Symposium on Electromagnetic Theory, Proceedings*, Eds., Stuchly, M. A., and Shannon, D. G., Victoria, Canada, May 2001, pp218-217.

Baum, C. E., "Focused Aperture Antennas," Air Force Research Lab Sensor and Simulation Notes, no. 306, 1987.

Baum, C. E., "Radiation of Impulse-Like Transient Fields," Air Force Research Lab Sensor and Simulation Notes, no. 321, 1989.

Baum, C. E., "Aperture Efficiencies for IRAs," Air Force Research Lab Sensor and Simulation Notes, no. 328, 1991.

Baum, Carl E., and Farr, Everett G., "Impulse Radiating Antennas," *Ultra-Wideband. Short-Pulse Electromagnetics*, edited by H. Bertoni et al., pp. 139-146, Plenum Press, 1993.

Baum, C. E., "Selection of Angles between Planes of TEM Feed Arms of an IRA," Air Force Research Lab Sensor and Simulation Notes, no. 425, 1998.

Baum, C. E., Farr, E. G., and Giri, D.V., "Review of Impulse Radiating Antennas," in *Review of Radio Science* W. R. Stone, Ed., Oxford University Press, 1999, pp. 403-439.

Brown, James, Ward and Churchill, Ruel V., *Complex Variables and Applications*, McGraw-Hill, Inc., 1996.

Buchenauer, C. Jerald, Tyo, J. S., and Schoenberg, J. S. H., "Aperture Efficiencies of Impulse Radiating Antennas," Air Force Research Lab Sensor and Simulation Notes, no. 421, 1997.

Cheng, David K., *Field and Wave Electromagnetics, Second Edition*, Addison-Wesley Publishing Company, 1989.

Farr, E. G. and Baum, C. E., "Prepulse Associated with the TEM Feed of an Impulse Radiating Antenna," Air Force Research Lab Sensor and Simulation Notes, no. 337, 1992.

Farr, E. G. and Baum, C. E., "Extending the Definitions of Antenna Gain and Radiation Pattern Into the Time Domain," Air Force Research Lab Sensor and Simulation Notes, no. 350, 1992.

Farr, E. G., "Optimizing the Feed Impedance of Impulse Radiating Antennas. Part I: Reflector IRAs," Air Force Research Lab Sensor and Simulation Notes, no. 354, 1993.

Farr, E. G. and Baum, C. E., "Radiation From Self Reciprocal Apertures," in *Electromagnetic Symmetry* C. E. Baum and H. N. Kritikos, Eds., Taylor & Francis, New York, 1995, pp.281-308.

Farr, E. G. and Baum, C. E., "Experimental Results of Optimizing the Location of Feed Arms in a Collapsible IRA and a solid IRA," Air Force Research Lab Sensor and Simulation Notes, no. 450, 2000.

Farr, E. G. and Bowen, L. H., "Experimental Results of Optimizing the Location of Feed Arms in a Collapsible IRA and a solid IRA," Air Force Research Lab Sensor and Simulation Notes, no. 450, 2000.

Farr, E. G., Farr Research Inc. [<http://www.farr-research.com/cat/ira2.htm>], 2001.

Farr, E. G., Telephone conversation, April 2001.

Giri, D. V., and Baum, C. E., "Reflector IRA Design Boresight Temporal Waveforms," Air Force Research Lab Sensor and Simulation Notes, no. 365, 1994.

Rhebergen, J. B., Zwamborn, A. P. M., and Giri, D.V., "Design of an Ultra-Wideband Ground-Penetrating Radar System Using Impulse Radiating Antennas," *Detection of Abandoned Land Mines, 1998. Second International Conference on the (Conf. Publ. No. 458)*, pp. 45-49, October 1998.

Tyo, J. S., "Optimization of the Feed Impedance for an Arbitrary Crossed-Feed-Arm Impulse Radiating Antenna," Air Force Research Lab Sensor and Simulation Notes, no. 438, Nov. 1999.

Tyo, J. S., and Buchenauer, C. Jerald, "Measurement of Prompt IRA Responses Under Different Focused Aperture Configurations," Air Force Research Lab Sensor and Simulation Notes, no. 454, 2001.

Yang, F. C., "Field Distributions on a Two-Conical-Plate and a Curved Cylindrical-Plate Transmission Line," Air Force Research Lab Sensor and Simulation Notes, no. 229, Nov. 1977.

INITIAL DISTRIBUTION LIST

1. Defense Technical Information Center
Ft. Belvoir, VA
2. Dudley Knox Library
Naval Postgraduate School
Monterey, CA
3. J. Scott Tyo
Assistant Professor of Electrical Engineering
EECE Department
University of New Mexico
Albuquerque, NM
4. John Gaudet
AFRL/DEHP
Kirtland AFB, NM
5. Eric Mokole
Naval Research Lab
Target Characteristics Branch, Radar Division
Washington, DC
6. Carl E. Baum
AFRL/DHEP
Kirtland AFB, NM
7. Evertt G. Farr
Farr Research Inc.
Albuquerque, NM